ADVANCED STRUCTURAL AND SPATIAL ANALYSIS OF LIPIDS

USING ION MOBILITY – MASS SPECTROMETRY

By

Michal Kliman

Dissertation

Submitted to the Faculty of the

Graduate School of Vanderbilt University

in partial fulfillment of the requirements

for the degree of

DOCTOR OF PHILOSOPHY

in

Chemistry

August, 2011

Nashville, Tennessee

Approved:

Professor John A. McLean

Professor Terry P. Lybrand

Professor H. Alex Brown

Professor Christopher J. Janetopoulos

Dedicated

to

Viera, my loving wife, my companion and best friend,

our loves Peter, Agatha and Esther,

Dad Cyril,

Mom Marianna,

Sister Mariana,

and

the Brothers and Sisters in Faith.

ACKNOWLEDGEMENTS

especially pastor Jim Thomas and the Tuesday band of brothers for shepherding us well.

I thank my nuclear family, dad Cyril Kliman, the progenitor of the family chemistry genes, mom Marianna Klimanova, who birthed and fanned my interest in English, my sister Mariana, my parents in law Michal and Viera Olejcek, brother in law Martin for their steady support and their many talents and drive to do every task well.

I lavish my thanks and affection on Viera my courageous, strong and loving companion and best friend for her overflowing heart and soul approach to the wellbeing of dad, and our loves Peter, Agatha, and Esther.

TABLE OF CONTENTS

Page

Chapter

Appendix

LIST OF TABLES

LIST OF FIGURES

LIST OF ABBREVIATIONS

ATD   arrival time distribution

CE   collision energy

CB   cerebroside

CCS   collision cross-section

Da   Dalton

DFT   density functional theory

DHA   2,5-dihydroxyacetophenone

DHB   2,5-dihydroxybenzoic acid

DLP   digital light patterning

DMA   digital micro-mirror array

DT   drift tube

DTIM   drift tube ion mobility

E   electrostatic field

EK   ethanolamine kinase

ESI   electrospray ionization

FAIMS   high-field asymmetric waveform ion mobility spectrometry

FWHH   full width at half height

HPLC   high-performance liquid chromatography

IM   ion mobility

IM-MS   ion mobility – mass spectrometry

ITO	indium tin oxide
K	mobility
LDI	laser desorption ionization
m/z	mass to charge ratio
MALDI	matrix-assisted laser desorption/ionization
MD	molecular dynamics
MS	mass spectrometry
MS/MS	tandem mass spectrometry
MS^n	tandem mass spectrometry
NMR	nuclear magnetic resonance
PC	phosphatidylcholine
PE	phosphatidylethanolamine
PG	phosphatidylglycerol
PS	phosphatidylserine
PtdCho	phosphatidylcholine
PtdEtn	phosphatidyethanolamine
PtdSer	phosphatidylserine
QM	quantum mechanics/mechanical
SIMS	secondary ionization mass spectrometry
SM	sphingomyelin
t_{ATD}	arrival time distribution
TLC	thin layer chromatography
TOF	time-of-flight mass analyzer

T-Wave	traveling wave
TWIM	traveling wave ion mobility
v/v	volume to volume ratio
wt	wild-type
Ω	collision cross-section

CHAPTER I

INTRODUCTION

1.1 Challenges of Contemporary Lipidomics

Advances in mass spectrometry (MS) instrumentation have facilitated the study of lipids on a comprehensive bioanalytical level previously occupied by genomics and proteomics initiatives.[1] In particular, the capability to ionize and detect intact lipid molecules afforded by electrospray ionization (ESI)[2,3] and matrix assisted laser desorption ionization (MALDI)[4,5] has over the last decade assisted in the discovery of a wide diversity of lipid structures and their myriad spatial distributions in tissues and cells.[6,7] There are now over 100,000 distinct lipid structures known, of which membrane lipids, such as glycerophospholipids and sphingolipids, number over 9,000 and counting in mammalian cells.[8] This observation is significant from a biochemical point of view as dedicated or sufficiently adaptable biosynthetic machinery must be in place to produce each unique lipid structure.[9,10]

Lipids are biosynthesized from a pool of relatively simple building blocks (*e.g.*, glycerol, fatty acids, sterol core, sphingosine, amino acids), yet occur in a vast number of molecular compositions primarily due to differences in the conformational arrangement of various chemical groups and moieties (*e.g.*, derivatization degree of sterol core, phospholipid headgroup type, position and

number of fatty acid carbons and double bonds, type of fatty acid linkage).[11] It is now well understood that in eukaryotic membranes these diverse molecular compositions of lipids are necessary to support the structure and function of a diverse population of membrane proteins as well as participate in complex signaling mechanisms.[12,13,14] Indeed, the undisputable contribution of MS to the biological knowledgebase of lipids is not only the characterization of the multitude of lipid structures but also its contribution to the elucidation of their specific cellular roles. Such findings have extensive application potential (*e.g.*, elucidation of lipid biosynthetic pathways,[8] cell membrane lipid distribution and function in membrane protein crystallography,[15,16] gas phase studies of lipid stabilized membrane proteins[17,18]) and in this respect any relevant MS advances carry a large value added benefit.

The impact of ESI and MALDI based MS analysis in lipidomics was realized by two technological advances, namely the coupling of MS to condensed phase separation techniques (*e.g.*, gas and liquid chromatography), and the more recent development of precision MS instrumentation with high mass accuracy, resolution, and controlled analyte ion fragmentation tools. ESI/MS and LC/ESI/MS analysis platforms with tandem MS/MS and MS[n] fragmentation capabilities have led the gradual elucidation of the vast compositional complexity of lipid species.[19] Structural diversity of lipids creates unique challenges to current efforts in quantitative characterization of the lipidome: (i) lack of availability of pure lipid standards, (ii) subtle structural and chemical features (*i.e.*, fatty acid length, position and number of double bonds, ion adducts)

2

significantly affect lipid ionization efficiencies, (iii) competitive ionization suppression effects are common. [20,21] In addition to these challenges, the majority of lipid signals occur and subsequently overlap in relatively narrow mass ranges (*e.g.,* between *ca.* 650 and 950 Da for membrane lipids), and their identification in complex biological samples can be hindered by the presence of endogenous and exogenous chemical noise.

In this work I present the proof of principle capability of MALDI-Ion Mobility-MS to provide a unique enhancement to MS only analysis of lipid species. I summarize here the potential advantages of IM and IM-MS in mobility separation of lipids from endogenous and exogenous chemical noise and mobility separation of classes of lipids. While ion mobility (IM) cannot achieve the high peak capacity (*i.e.,* theoretical number or resolved peaks per unit of separation time) of condensed phase separation techniques, typical IM separations occur on the order of μs to ms, and yield high IM-MS peak capacity production rates (*ca.* 10^6 to 10^8 sec^{-1}).[22] Since IM disperses analyte signals based on a unique gas phase size dimension of separation, it has the potential to provide a concentration dynamic range enhancement to both condensed phase and MS lipid separations.[23,24] Clemmer and coworkers have utilized a combined LC-IM-MS approach toward increased peak capacity profiling of peptides in human plasma proteome.[25,26] These methods have the potential to greatly inform and advance the current proof of principle IM-MS analyses of lipids.

As detailed in section 1.2 and chapter 2, IM-MS can be expected to provide an increase in dynamic range in lipid analysis based on relative

differences in gas phase folding efficiencies of different biomolecular classes. Additionally, IM-MS can be used to obtain collision cross section (*i.e.* apparent surface area) measurements of lipid ions for subsequent computational interrogation of their gas phase structural separation. Such methods are extensively described in sections 1.2.3 and 1.2.4 and applied in chapter 3 in the interpretation of observed mobility separation trends of membrane lipid standards. In addition to the promise of endogenous biomolecular IM separations, exogenous chemical noise can be efficiently removed in MALDI-IM-MS analysis. In chapter 4, I summarized this capability in the analysis and relative quantitation of brain lipids of the *Drosophila eas* mutant.

1.1.2 Challenge of high spatial resolution in lipid analysis

Advanced mass spectrometry approaches to obtaining better lipid structural and functional information have now been at the forefront of lipid research for a decade. An emerging technological challenge in lipid analysis is the determination of where lipid structures occur in cells and tissues, in a spatially and temporally resolved manner. While both ESI[3,27] and MALDI[28,29] lipid studies have greatly advanced the understanding of lipid fine structure, abundance and biomolecular function, relatively little is known about the spatial distribution and abundance of lipids and their spatially correlated fine structure detail.[30] Chemical imaging methods (*i.e.*, staining,[31,32,33] antibody[34]) have been very useful in efforts to understand total lipid content and the distribution of various classes of lipids at the cellular and sub-cellular levels; however, chemical

4

imaging can only provide limited fine structure lipid information (*e.g.*, headgroup).[35] To build a picture about where and in what concentration lipids reside in cells and the sub-cellular compartments, new technological approaches are necessary.[36] Indeed, to better appreciate the structural diversity and complexity of lipids, and the myriad roles of lipids in biology, high resolution spatial analysis of lipids at fine structure level is essential.

Mass spectrometry detection coupled to post ionization by ion beams, *i.e.*, secondary ionization mass spectrometry (SIMS), and assisted laser desorption ionization (LDI), have emerged as strong techniques for lipid imaging in cells and tissues. In chapter 5, I detail a promising novel approach to laser beam manipulation based on the digital micro mirror array (DMA) device. Current 15:1 demagnification ratio of the DMA optical train is sufficient to generate a <1 μm image size from a laser beam reflected from a single 12x12 μm mirror of the DMA device, which is approximately two times larger than the limit imposed by diffraction (λ=355nm). In chapter 5, profiling experiments of peptide standards are demonstrated at 5 μm spatial resolution, and lipid imaging experiments at 8 μm spatial resolution from mouse brain tissue sections. Since the optical train detailed in chapter 5 does not require optical components mounted in the vacuum of the imaging instrument, it can transfer seamlessly between MS instrumental platforms, including IM-MS.[37]

1.2 Biomolecular ion mobility-mass spectrometry overview

The coupling of IM to a mass spectrometer (MS) occurred to achieve faster analyte identification and to utilize the two dimensional advantage of this technique in complex mixture analysis.[38,39] Pioneering work in structural analysis of larger molecular species using ion mobility mass spectrometry (IM-MS) was performed by the laboratories of Bowers, Jarrold, and Clemmer. They successfully combined highly accurate experimental measurements with atomic detail of quantum mechanical and molecular dynamics calculations and reliable computational collision cross-section (CCS) calculations in analyses of metal[40] and carbon clusters,[41] polymers,[42] peptides,[43] proteins,[44,45] oligosaccharides,[46] and oligonucleotides.[47,48]

Further biomolecular IM-MS structural studies uncovered an important result. Various types of biomolecules were found to separate in IM measurements based on their differences in intramolecular gas phase packing densities.[39] For several years peptides,[49,50] proteins,[22,51] nucleotides,[52] and carbohydrates[53] remained the focus of IM-MS studies. In 2007 Jackson, et al.[54,55] demonstrated the utility of using an IM-MS (*i.e.*, MALDI-IM-TOF-MS) instrument in imaging of rat brain lipids. Further data collected by Jackson, et al.[56] and Fenn, et al.[57,58] showed lipids to have the least gas phase packing efficiency of all previously studied biomolecules, allowing reliable separation of their signals from peptides and other biomolecular ions as shown in Figure 1.1.
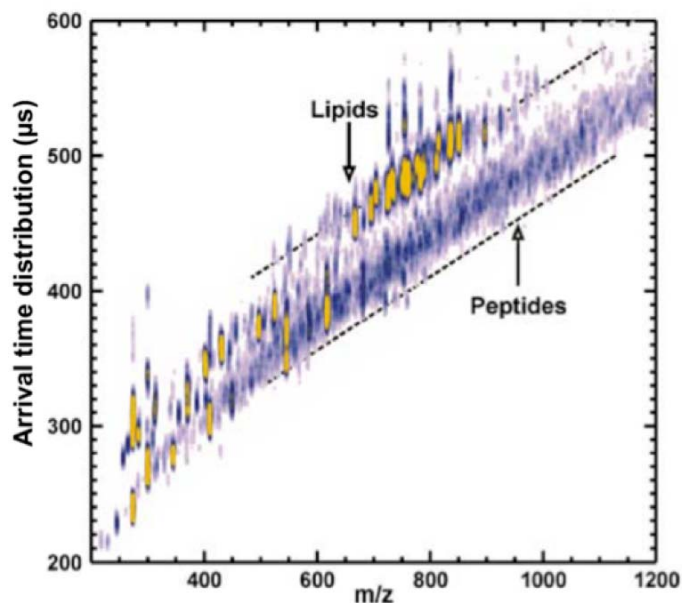
Figure 1.1 2-D plot of MALDI-IM-MS conformation space for the simultaneous analysis of lipids and peptides directly from a thin animal tissue section (12 μm). Note the arrival times of lipid signals differ markedly from the arrival times of same mass peptide signals. False coloring represents signal intensity, such that the more intense signals are shown in brighter colors. Adapted from Figure 2 in *Journal of Mass Spectrometry,* "Profiling and imaging of tissues by imaging ion mobility-mass spectrometry," 42, 2007, 1099-1105, J.A. McLean, W.B. Ridenour and R.M. Caprioli, with permission. Copyright© 2007 Wiley-Liss, Inc.

1.2.1 Types of ion mobility

Ion mobility separations utilize low energy gas-phase collisions to separate ions predominantly on the basis of molecular surface area, also known as the ion-neutral collision cross-section (Ω) with units of $Å^2$. Generally speaking, ions are injected into a separation cell filled with a neutral drift gas and migrate under the influence of a weak electric field. The applied electric field is electrostatic for drift tube ion mobility (DTIM) and electrodynamic for both traveling wave ion mobility (TWIM) (Figure 1.2) and field asymmetric waveform ion mobility spectrometry (FAIMS) separations. In the presence of the neutral drift gas larger ions have a lower mobility than smaller ions, resulting in longer

drift times versus shorter drift times, respectively. Following the elution profile of

the ions from the IM-dimension, mass spectra are constantly being acquired and

the drift time information from the ion mobility measurement is combined with the

m/z measurement from the mass spectrometer. The result is a three dimensional

data set displaying mass-to-charge typically on the x-axis, drift time on the y-axis,

and signal intensity on the z-axis (Figure 1.3).
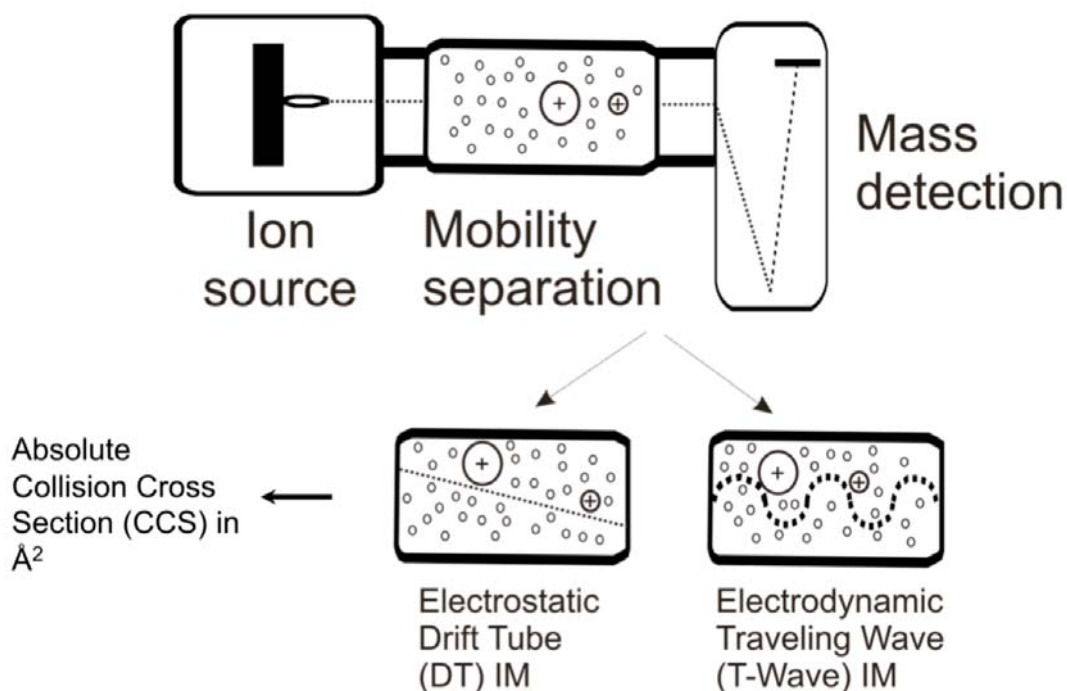
Figure 1.2 General schematic of the IM-MS instrument and two predominant types of ion mobility separation, drift tube (DT) and traveling wave (T-Wave). In DTIM mobility separation occurs along a linearly decreasing electrostatic potential gradient, while in T-Wave IM ions encounter collisions and separate being propagated on electrodynamic potential waves.
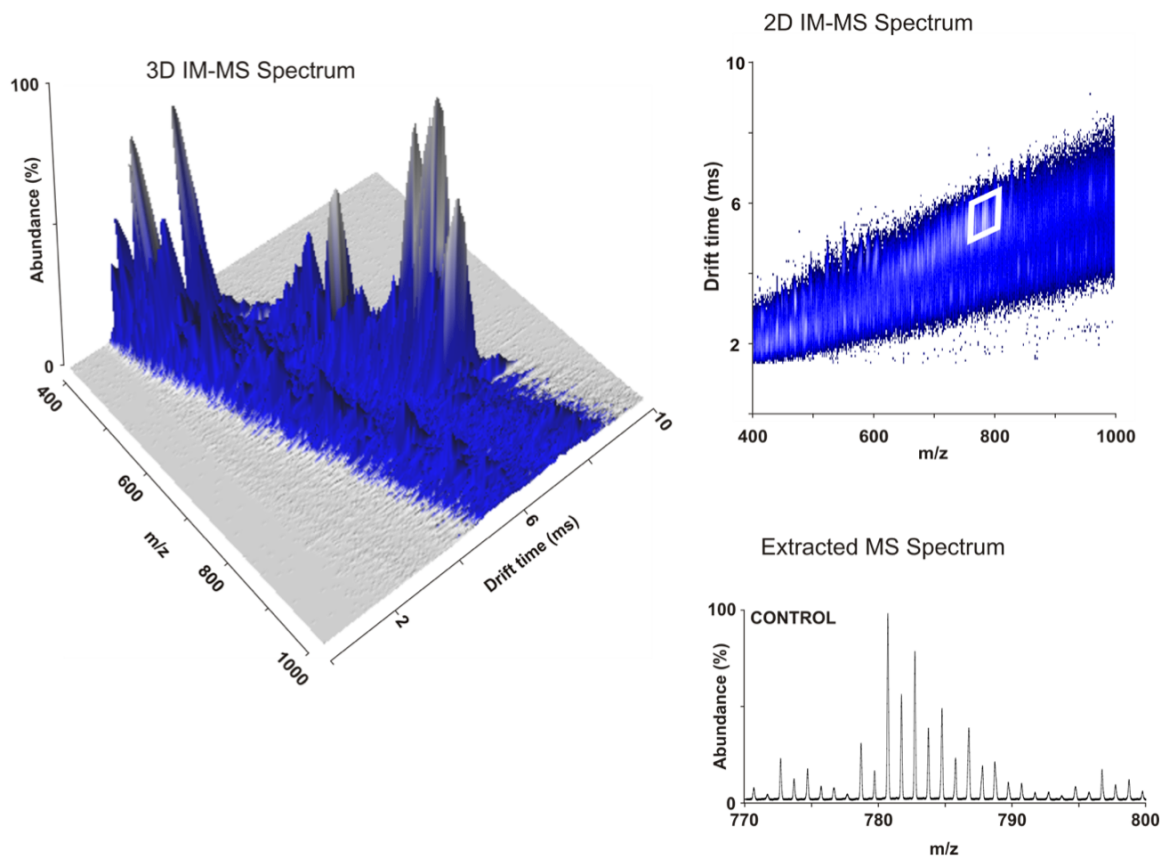
Figure 1.3 Data dimensionality of the IM-MS separation. In the 3D plot % abundance (*i.e.*, intensity) is projected along the z-axis, in the 2D IM-MS plot the intensity is represented by false coloring (*i.e.*, here more intense signals are brighter), m/z typically projected on the x-axis and mobility drift time on the y-axis. The MS spectrum shown on the bottom right is an extracted % abundance *vs.* m/z plot of lipid signals extracted from the highlighted region of the 2D IM-MS plot.

1.2.1.1 Drift tube ion mobility (DTIM)

The original ion mobility design was developed by using a drift tube composed of a series of concentric ring electrodes connected by resistors to create a uniform electrostatic field. Under the influence of this electrostatic field and in the presence of a low molecular weight drift gas (*e.g.*, helium, nitrogen, argon) the ions separate along the axis of motion based on their mobility (*i.e.*, the number of low energy collisions between the ions and the drift gas molecules).

9

The relative inherent simplicity of the drift tube design enables the transformation of measured drift time data into absolute collision cross-section by using the kinetic theory of gases as detailed in Section 1.2.3. Thus, structural information can be inferred from the measurement of cross-section when combined with computational approaches (section 1.2.4). The mobility resolution afforded in typical DTIM arrangements ranges from 30-50 ($r = t/\Delta t$ at FWHH), although longer, cryogenically cooled, or higher pressure drift tubes can be used to achieve mobility resolutions exceeding 100.[59,60]

1.2.1.2 Traveling wave ion mobility (TWIM)

The commercial availability of traveling wave ion mobility instrumentation continues to make IM-MS technology accessible to a large number of users. Similar to drift tube instruments, TWIM separates ions by time dispersion through collisions with a background drift gas, but by using electrodynamic fields rather than electrostatic fields.[61] This is accomplished by transmitting voltage pulses sequentially across a stack of ring electrodes; the voltage pulses create a travelling wave.[62] Conceptually, TWIM separations are performed based on the susceptibility of different ions to the influence of the specific wave characteristics and may be described as the ability of ions to "surf" on these waves. Adjustable wave parameters include: travelling wave pulse height, wave velocity, and ramping either of these variables. Generally IM resolution in the TWIM is similar to that of typical DTIM cells, *ca.* 30-50. Although there are protocols to obtain relative collision cross-section values by using TWIM experimental data, the

calculations still rely on absolute values obtained by using drift tube instruments.[63,64]

1.2.1.3 Asymmetric field ion mobility spectrometry (FAIMS)

Ion separations utilizing FAIMS were first documented in the early 1990s by Buryakov and coworkers[65] and since have seen commercial success primarily as sensitivity improvement front-end devices. Separation selectivity in FAIMS occurs on the basis of the nonlinear dependence of the mobility coefficient in varying electric fields. Unlike time-dispersive DTIM and TWIM separations, FAIMS performs space-dispersive separations. In FAIMS devices, ions are subjected to positive and negative electric fields that oscillate perpendicular to the direction of ion propagation. By injecting ions between two parallel plates in a separation cell and directing this waveform perpendicularly across them, only selected ions will traverse the cell, and all other ions will strike either the lower or upper plate. The use of a compensation voltage roughly achieves in FAIMS a mobility-based selection similar to a radio frequency mass selection in a quadrupole.

While ion mobility data obtained from DTIM enables absolute collision cross-section calculations (section 1.2.3) the TWIM and FAIMS can currently only provide estimated collision cross-sections based on previously measured DTIM values. Although efforts to understand the fundamental physical processes in TWIM and FAIMS separations are under way, gas-phase kinetics theory to describe these processes is still an ongoing research endeavor.[66,67]

11

1.2.2 Motion of ions within neutral gases

The theory of ion movement through a neutral gas medium is rooted in the classical electrodynamics of directed diffusion and theoretical gas dynamics studies by Mason and McDaniel, and others. The size-dependent movement of ions in an ion mobility cell is an intuitive process. After an ion is created in the source, it travels "downhill" through the mobility cell along a linearly decreasing electrostatic voltage gradient. As the ion traverses the mobility cell, it experiences numerous low-energy collisions (*ca.* 10^5-10^7) at moderate pressures and drift cell lengths. At sufficiently low electrostatic field strengths, where ion-neutral collisions are considered elastic, the ion is free to rotate and tumble through the drift cell. Owing to the combination of the large number of collisions and low field strength, the drift velocity (v_d) of the ion as it moves through the neutral gas is size dependent. Ions experiencing different numbers of collisions will have different drift velocities and, therefore, will spatially separate along the direction of movement.[66-69]

1.2.3 Foundational principles of ion mobility structural separations

Several excellent works describe the mathematical foundation of ion mobility and the derivation of CCS from IM measurements, using the kinetic theory of gases.[68,70,72] At sufficiently low field strength, the drift velocity (v_d) is linearly dependent on the strength of the applied electrostatic field (E), and the linearity constant in this relationship is referred to as mobility (K).

12

$$v_d = KE \qquad \text{Eq. (1)}$$

Generally, mobility can be determined by measuring the drift time (t_d) of an ion across a drift cell of fixed length (L).

$$K = \frac{v_d}{E} = \frac{L}{t_d E} \qquad \text{Eq. (2)}$$

In practice, however, the time parameter obtained in an IM experiment is the arrival time distribution (t_{ATD}) of a packet of identical ions at the detector. The arrival time of an ion is the sum of the time the ion spends in the drift cell (t_d) and that it spends in the other parts of the instrument (*i.e.*, the ion source, ion optics, and detector region). The time spent outside the drift cell can be determined by performing IM at multiple electrostatic-field strengths by varying the potential (V) across the length of the drift cell. Through constructing a plot of t_{ATD} versus the inverse of the applied drift cell potential ($1/V$), a linear regression fit to these data yields two important results. Firstly, if the fit is linear, it indicates that low-field conditions predominate. Secondly, the y-intercept corresponds to the time the ions spend outside the drift cell region, which is the limit where the applied potential across the drift cell is infinite and $t_d = 0$.

Ion-drift velocity changes with the number of collisions and, therefore, depends on gas number density (N), pressure (p) and gas velocity (v_{mean}); all these also depend on temperature (T). To derive CCS from K, the dependence of K on temperature and gas density must be further evaluated. By convention, K is

reported as the standard or reduced mobility (K_0), which normalizes K to standard temperature and pressure (*i.e.*, 0 ^{o}C / 273 K and 760 Torr):

$$K_0 = K \frac{p}{760} \frac{273}{T} = \frac{L}{t_d E} \frac{p}{760} \frac{273}{T}$$

Eq. (3)

The mean thermal velocity of gas and ion molecules under zero electrostatic field conditions, assuming a Maxwellian distribution function of molecular and ion velocities at thermal equilibrium, can be expressed as v_{mean}, where T is temperature (Kelvin), k is the Boltzman constant, and M_r is reduced mass.

$$v_{mean} = \left(\frac{8kT}{\pi M_r} \right)^{\frac{1}{2}}$$

Eq. (4)

When a sufficiently weak electrostatic field is applied to a mixture of gas and charged molecules, the direction of movement (and velocity) of ions in the gas consists of two components, the random motion of ions at the temperature of the gas, on which a second small component in the direction of the electrostatic field is imposed. If the mean ion energy (and, therefore, velocity) as the ion traverses the mobility cell does not increase, the mobility separation is said to be performed under "low field" conditions, and interaction of the ion with the gas molecules via elastic collisions can be assumed. At higher electrostatic field strengths, the ion velocity depends less strongly on the gas temperature, and the mean ion energy increases as it traverses the drift region. Under these "high field" conditions, tumbling and elastic collisions can no longer be assumed, and K is no longer constant, but depends on the ratio of electrostatic field to the gas-

number density (E/N). Provided the field strength is sufficiently weak to afford mobility separation at low field conditions (*i.e.*, constant K), a closed equation for the dependence of K_0 on the ion-neutral CCS (Ω) of the ion-neutral pair can be expressed as follows:

$$K_0 = \frac{(18\pi)^{\frac{1}{2}}}{16} \frac{ze}{(k_BT)^{\frac{1}{2}}} \left[\frac{1}{m_i} + \frac{1}{m_n}\right]^{\frac{1}{2}} \frac{1}{N_0} \frac{1}{\Omega}$$
$\qquad$ Eq. (5)

where, ze is the elementary charge of the ion, N_0 is the number density of the drift gas at STP (0 °C / 273 K and 760 Torr), the middle term is the reduced mass of the ion-neutral collision pair (ion and neutral masses of m_i and m_n, respectively), and k_B is the Boltzmann's constant. Substituting for K_0 and rearranging to solve for Ω yields:

$$\Omega = \frac{(18\pi)^{\frac{1}{2}}}{16} \frac{ze}{(k_BT)^{\frac{1}{2}}} \left[\frac{1}{m_i} + \frac{1}{m_n}\right]^{\frac{1}{2}} \frac{t_dE}{L} \frac{760}{p} \frac{T}{273} \frac{1}{N_0}$$
$\qquad$ Eq. (6)

This is the functional form of the equation used to derive collision cross-section from mobility data. This equation holds when the collisions of ions with neutral gas molecules can be assumed to be elastic. The collision cross-section thus derived is termed "hard sphere" (*i.e.*, only momentum is transferred at the point of ion neutral collision). Comparisons of experimentally measured and theoretically derived CCSs show that the hard-sphere, elastic-collision assumption holds for analytes larger than *ca.* 500 Da, which is a mass range well suited for lipid analysis.[73]

1.2.4 Computational approaches for interpretation of structure

Empirically determined collision cross-section values can be used to probe structural motifs of various biomolecular ions including lipids,[58] peptides/proteins[44,49,74] and protein complexes.[63,46,75] This is accomplished by augmenting IM CCS measurements with computational modeling strategies. For structural interpretation, the CCS is used as a size constraint that can be used to discriminate and interpret a subset of structures from a large pool of computationally generated conformers. Structural populations can be expected to consist of structurally similar ions that either undergo thermally accessible structural/conformational isomerization/interconversion or, depending on intramolecular forces and atomic arrangement, may even remain in relatively fixed conformations on the time scale of the IM-MS experiment.[76] Therefore, each IM-MS unique signal, ideally corresponding to identical ions with different conformations, has its own unique structural signature determined by the average shape of the populations of ions that create it. This structural signature is the basis for biomolecular separations[39] observed in IM-MS, and is also the explanation for the observed difference in average IM *vs. m/z* trendline variability (*i.e.*, spread, structural richness) of the different biomolecular classes observed by IM-MS.[58]

Following the experimental determination of CCS, computational modeling is performed in the following general sequence: (i) the structure of the molecular ion is built by using one of the available structure-building software packages, (ii) the atomic charge parameters for the built structure are determined by using

quantum mechanical (QM) calculations, and point charge derivation, and (iii) molecular dynamics is performed to create a large number of structural conformers whose CCS can be computationally determined to allow experimental CCS based clustering analysis. A schematic of the workflow for combining the measured CCS with computational interpretation is illustrated in Figure 1.4.

There are several software packages well suited for structure building of lipids, some proprietary (*e.g.*, Molecular Operating Environment, Chemical Computing Group, Montreal, Canada), and some freely available (*e.g.*, SIRIUS, University of California, San Diego). Although computer-processing speed has increased exponentially over several decades, computation still puts a limit on how large a system can be realistically studied by using the protocol described here. QM geometry optimization and electrostatic potential calculations in charge parameter development at intermediate level of quantum theory on the most powerful desktop workstations give reasonable 24 h results on systems of 20 atoms. Calculations, however, scale up exponentially not only with the level of theory and number of atoms, but also with mass of included elements. For example, studies of lipids in the presence of metal ions may require additional specialized basis sets and time. Therefore, quantum charge parameterization of larger systems has to be done on properly capped fragments, which are later connected for molecular dynamics sampling.

Many free and proprietary QM software packages are capable of performing the needed geometry optimization and electrostatic potential

calculations (*e.g.*, Cerius, Jaguar, Gaussian, Spartan) at basic to intermediate levels of theory. The last step of the computational protocol is the conformational MD sampling coupled with computational clustering analysis based on the comparison of the computed CCS values for the generated structural conformers with the experimental CCS value. Once the charge parameters for each atom in the built structure are determined, one of the available molecular dynamics packages (*e.g.*, Amber,[77] CHARMM, ACCELRYS) can be used to perform conformational sampling.

Conformational sampling is a molecular dynamics calculation that yields a large number of structural conformers of the studied peptide/protein ion. Two primary challenges of MD-based conformational sampling methods are the use and development of reliable MD parameters that assure chemically and structurally relevant results and of temperature protocols that lead to a completely randomized pool of final structures. Aforementioned MD software packages typically contain reliable MD parameters for standard amino acids, carbohydrates and nucleotides. Fully randomized sampling without any bias toward one or several conformations can normally be guaranteed by selecting a temperature scheme (heating and cooling algorithm) for the MD calculation in which the studied lipid structure is heated to a temperature at which it can access all reasonably expected conformational states and then cooled slowly to relax into a low-energy structural conformer.

A. Measurement of the experimental arrival time distribution

↓

Absolute collision cross section calculation

↓

$$\Omega = \frac{(18\pi)^{\frac{1}{2}}}{16} \frac{ze}{(k_bT)^{\frac{1}{2}}} \left[\frac{1}{m_i} + \frac{1}{m_b}\right]^{\frac{1}{2}} \frac{t_dE}{L} \frac{760}{p} \frac{T}{273.15} \frac{1}{N_0}$$

B. QM charge derivatization (Gaussian 2003)

↓

Conformational sampling (AMBER)

↓

Collision cross section calculation (MOBCAL [M. F. Jarrold, IU])

C.

Potential energy (kcal/mol) vs. Collision cross section (Å²)

ca. 30,000 structures

ca. 1,000 structures of experimental CCS and low energy

Dendrogram comparison of atomic coordinates (Center for Structural Biology, VU)

D. Cluster analysis

RMS distance (Å)

Figure 1.4 (A) Experimentally determined collision cross-sections (CCSs) are calculated from the measured ion mobility drift times (arrival time distributions). (B) Lipid molecule is built and fully parameterized for molecular dynamics (MD) using Gaussian and AMBER software. MD calculations yield an ensemble of structures (each data point represents an individual structure) each with a unique potential energy. MOBCAL calculates the theoretical CCS for each structure. (C) Plot of potential energy *vs.* CCS of each structure is generated. The subgroup of structures corresponding to the experimentally determined CCS and of lowest energy (*e.g.,* here less than average < 55 kcal/mole) can then be examined to interpret structural similarities within the group of structures by (D) dendrogram and clustering analysis to better understand the prevailing intramolecular forces that govern the shape of the lipids in this study.

An important output result of the MD calculation is the relative potential energy value of each conformer within the pool of generated structures. The computational collision cross-section value for each conformer is then calculated

by using one of two currently available codes, Mobcal[78] or Sigma.[79,80] Once both the relative potential energy and collision cross-section values are computed for each member of the computationally generated ensemble of structures, a plot of energy *vs.* computed CCS is generated and visually inspected. Typically the lowest energy conformers with a computed CCS that matches the experimental value range are selected for further computational analysis (*e.g.*, analysis of selected average distances, or clustering on the basis of atomic positions). Following cluster analysis, general structural motifs are obtained that are consistent with the measurement, while other structural motifs can be ruled out.

1.3 Characterization of lipids by IM-MS

An important development in MS technology has been the recent incorporation of post-ionization gas-phase separation based on ion mobility (IM) into high-end commercial MS instrumentation.[81,82] Current state-of-the art ion mobility-mass spectrometry (IM-MS) instruments integrate seamlessly with both ESI and MALDI soft ionization sources, and are highly applicable to the described lipid analysis challenges. IM-MS affords rapid (µs to ms) two-dimensional size and mass based separations with unique benefits to the analysis of complex biological samples. Previously, IM-MS has been successfully used in studies of the gas-phase behavior and separations of peptides,[43,49,83,84,85,86] proteins,[44,45,74] and nucleotides.[87,88,89] More recently, Woods *et al.*[39] and Fenn *et al.*[57] demonstrated that IM analysis efficiently resolves

lipids from peptides, carbohydrates and nucleotides and exogenous noise based on differences in their gas-phase packing efficiencies. This signal partitioning in IM-MS was recently shown to be particularly useful in the direct analysis of lipids from mutant *Drosophila* brain tissues.[90] As compared with MS alone, the enhanced peak capacity of IM-MS analysis[91] not only provides a substantial reduction of chemical noise in lipidomic measurements,[54,58,92,93] and a concomitant increase in dynamic range, but it can also exploit an additional characteristic of lipid ions: various sub-classes of lipids display differences in gas-phase packing resolvable by IM-MS and this value-added information can be further utilized in the isolation, identification and characterization of specific lipid structures.[37,56,58,94,95,96]

1.4 Summary and objectives

In this dissertation work, I sought to highlight the opportunities provided by IM-MS technology and high-resolution lipid imaging for high confidence structural and spatial analysis of lipids. Traditional mass spectrometry approaches have dramatically advanced lipid characterization by allowing both parent and fragment lipid mass analysis and thus made great inroads into understanding the complexity of lipid structures. IM-MS, which was only recently applied in lipid research, provides a technological platform that allows fast mobility separation of lipids from other biomolecules, potentially in simultaneous analysis (Chapter 2). Moreover, mobility profiles of various classes of lipids differ in the IM-MS

conformation space and the underlying structural detail of such separations can be elucidated using a combination of empirical IM-MS CCS studies with detailed computational MD simulations (Chapter 3). Recent commercialization of IM-MS allows a seamless transfer of basic IM-MS lipid research to current problems in biology and medical sciences (Chapter 4). In addition to advanced lipid mobility separation studies, I explored an opportunity to use an advanced laser patterning system based on digital mirror array device in improving the spatial resolution of MALDI-TOF-MS and MALDI-IM-MS lipid imaging of tissues and cells (Chapter 5). The specific objectives I pursued, and the titles of chapters where each objective was addressed, are:

1. Where do lipids occur in the biomolecular conformation space of IM-MS, how well do they resolve from other biomolecules (*i.e.*, peptides, carbohydrates, and oligonucleotides)? What is the breath of the conformation space they occupy? This goal was addressed in Chapter 2: Ion Mobility-Mass Spectrometry Conformational Landscape of Anhydrous Biomolecules.

2. What overall trends of separation exist among membrane lipids? Can the IM-MS resolution of various classes of membrane lipids be described using computational structure analysis? This objective was addressed in Chapter 3: Structural Selectivity of Anhydrous Sphingolipids and Glycerophospholipids in Ion Mobility-Mass Spectrometry Analysis.

3. Over the last decade prototype IM-MS has successfully been applied in current problems of biology and medicinal research, primarily for the analysis of peptides and proteins. Can the newly commercialized IM-MS instrumentation prove to be as useful in lipid analysis? The work toward this objective was described in Chapter 4: Structural Mass Spectrometry Analysis of Lipid Changes in a *Drosophila* Epilepsy Model Brain.

4. The knowledge of the spatial distribution of specific lipid structures in cells and tissues is key to understanding the myriad roles lipids play in animal and plant biology. MALDI MS has been successfully applied in peptide and protein analysis at tens of micrometers spatial resolution. Can digital light patterning be used to narrow the current spatial resolution gap between MALDI MS and its older imaging partner SIMS? The data obtained toward this goal is summarized in Chapter 5: Dynamic Light Patterning for High Spatial Resolution Imaging of Lipids.

REFERENCES

[1] Brown, H. A.; Murphy, R. C., Working towards an exegesis for lipids in biology. *Nature Chemical Biology* **2009,** *5* (9), 602-606.

[2] Whitehouse, C. M.; Dreyer, R. N.; Yamashita, M.; Fenn, J. B., Electrospray interface for liquid chromatographs and mass spectrometers. *Analytical Chemistry* **1985,** *57* (3), 675-679.

[3] Ivanova, P. T.; Milne, S. B.; Myers, D. S.; Brown, H. A., Lipidomics: a mass spectrometry based systems level analysis of cellular lipids. *Current Opinion in Chemical Biology* **2009,** *13* (5-6), 526-531.

[4] Karas, M.; Hillenkamp, F., Laser desorption ionization of proteins with molecular masses exceeding 10,000 daltons. *Analytical Chemistry* **1988,** *60* (20), 2299-2301.

[5] Murphy, R. C.; Hankin, J. A.; Barkley, R. M., Imaging of lipid species by MALDI mass spectrometry. *Journal of Lipid Research* **2009,** *50*, S317-S322.

[6] Burnum, K. E.; Cornett, D. S.; Puolitaival, S. M.; Milne, S. B.; Myers, D. S.; Tranguch, S.; Brown, H. A.; Dey, S. K.; Caprioli, R. M., Spatial and temporal alterations of phospholipids determined by mass spectrometry during mouse embryo implantation. *Journal of Lipid Research* **2009,** *50* (11), 2290-2298.

[7] Murphy, S. C.; Fernandez-Pol, S.; Chung, P. H.; Murthy, S. N. P.; Milne, S. B.; Salomao, M.; Brown, H. A.; Lomasney, J. W.; Mohandas, N.; Haldar, K., Cytoplasmic remodeling of erythrocyte raft lipids during infection by the human malaria parasite Plasmodium falciparum. *Blood* **2007,** *110*, 2132-2139.

[8] Yetukuri, L.; Ekroos, K.; Vidal-Puig, A.; Oresic, M., Informatics and computational strategies for the study of lipids. *Molecular BioSystems* **2008,** *4* (2), 121-127.

[9] van Meer, G.; Voelker, D. R.; Feigenson, G. W., Membrane lipids: where they are and how they behave. *Nature Reviews Molecular Cell Biology* **2008,** *9* (2), 112-124.

[10] Wenk, M. R., The emerging field of lipidomics. *Nature Reviews Drug Discovery* **2005,** *4* (7), 594-610.

[11] Dowhan, W., Molecular basis for membrane phospholipid diversity: Why are there so many lipids? *Annual Review of Biochemistry* **1997,** *66*, 199-232.

[12] Engelman, D. M., Membranes are more mosaic than fluid. *Nature* **2005,** *438* (7068), 578-580.

[13] Chun, J., The sources of a lipid conundrum. *Science* **2007,** *316* (5822), 208-210.

[14] Dobrosotskaya, I. Y.; Seegmiller, A. C.; Brown, M. S.; Goldstein, J. L.; Rawson, R. B., Regulation of SREBP processing and membrane lipid production by phospholipids in Drosophila. *Science* **2002,** *296* (5569), 879-883.

[15] Hunte, C.; Richers, S., Lipids and membrane protein structures. *Current Opinion in Structural Biology* **2008,** *18* (4), 406-411.

[16] Phillips, R.; Ursell, T.; Wiggins, P.; Sens, P., Emerging roles for lipids in shaping membrane-protein function. *Nature* **2009,** *459* (7245), 379-385.

[17] Wang, S. C.; Politis, A.; Di Bartolo, N.; Bavro, V. N.; Tucker, S. J.; Booth, P. J.; Barrera, N. P.; Robinson, C. V., Ion Mobility Mass Spectrometry of Two Tetrameric Membrane Protein Complexes Reveals Compact Structures and Differences in Stability and Packing. *Journal of the American Chemical Society* **2010,** *132* (44), 15468-15470.

[18] van der Spoel, D.; Marklund, E. G.; Larsson, D. S. D.; Caleman, C., Proteins, Lipids, and Water in the Gas Phase. *Macromolecular Bioscience* **2011,** *11* (1), 50-59.

[19] Sud, M.; Fahy, E.; Cotter, D.; Brown, A.; Dennis, E. A.; Glass, C. K.; Merrill, A. H.; Murphy, R. C.; Raetz, C. R. H.; Russell, D. W.; Subramaniam, S., LMSD: LIPID MAPS structure database. *Nucleic Acids Research* **2007,** *35*, D527-D532.

[20] Petkovic, M.; Schiller, J.; Muller, M.; Benard, S.; Reichl, S.; Arnold, K.; Arnhold, J., Detection of individual phospholipids in lipid mixtures by matrix-assisted laser desorption/ionization time-of-flight mass spectrometry: Phosphatidylcholine prevents the detection of further species. *Analytical Biochemistry* **2001,** *289* (2), 202-216.

[21] Lou, X. W.; van Dongen, J. L. J.; Vekemans, J.; Meijer, E. W., Matrix suppression and analyte suppression effects of quaternary ammonium salts in matrix-assisted laser desorption/ionization time-of-flight mass spectrometry: an investigation of suppression mechanism. *Rapid Communications in Mass Spectrometry* **2009,** *23* (19), 3077-3082.

[22] McLean, J. A.; Ruotolo, B. T.; Gillig, K. J.; Russell, D. H., Ion mobility-mass spectrometry: a new paradigm for proteomics. *International Journal of Mass Spectrometry* **2005,** *240* (3), 301-315.

[23] Hilderbrand, A.E.; Myung, S.; Srebalus Barnes, C.A.; Clemmer, D.E., Development of LC-IMS-CID-TOFMS techniques: analysis of a 256 component tetrapeptide combinatorial library. *Journal of the American Society for Mass Spectrometry* **2003**, *14*, 1424-1436.

[24] Liu, X.; Plasencia, M.; Ragg, S.; Valentine, S.J.; Clemmer, D.E., Development of high throughput dispersive LC--ion mobility--TOFMS techniques for analysing the human plasma proteome. *Briefings in Functional Genomics and Proteomics* **2004,** *3*, 177-186.

[25] Valentine, S. J.; Plasencia, M. D.; Liu, X. Y.; Krishnan, M.; Naylor, S.; Udseth, H. R.; Smith, R. D.; Clemmer, D. E., Toward plasma proteome profiling with ion mobility-mass spectrometry. *Journal of Proteome Research* **2006,** *5* (11), 2977-2984.

[26] Liu, X. Y.; Valentine, S. J.; Plasencia, M. D.; Trimpin, S.; Naylor, S.; Clemmer, D. E., Mapping the human plasma proteome by SCX-LC-IMS-MS. *Journal of the American Society for Mass Spectrometry* **2007,** *18* (7), 1249-1264.

[27] Ivanova, P. T.; Milne, S. B.; Byrne, M. O.; Xiang, Y.; Brown, H. A., Glycerophospholipid identification and quantitation by electrospray ionization mass spectrometry. *Lipidomics and Bioactive Lipids: Mass-Spectrometry-Based Lipid Analysis* **2007,** *432*, 21-57.

[28] Jackson, S. N.; Wang, H. Y. J.; Woods, A. S., In situ structural characterization of glycerophospholipids and sulfatides in brain tissue using MALDI-MS/MS. *Journal of the American Society for Mass Spectrometry* **2007,** *18* (1), 17-26.

[29] Fuchs, B.; Suss, R.; Schiller, J., An update of MALDI-TOF mass spectrometry in lipid research. *Progress in Lipid Research* **2010,** *49* (4), 450-475.

[30] Murphy, R. C.; Hankin, J. A.; Barkley, R. M., Imaging of lipid species by MALDI mass spectrometry. *Journal of Lipid Research* **2009,** *50*, S317-S322.

[31] van Goor, H.; Gerrits, P.O.; Ground, J., The application of lipid-soluble stains in plastic embedded sections. *Histochemistry* **1986,** *85* (3), 251-253.

[32] Wigglesworth, V. B., Histological staining of lipids for the light and electron microscope. *Biological Reviews of the Cambridge Philosophical Society* **1988,** *63* (3), 417-431.

[33] Rudolf, M.; Curcio, C. A., Esterified Cholesterol Is Highly Localized to Bruch's Membrane, as Revealed by Lipid Histochemistry in Wholemounts of Human Choroid. *Journal of Histochemistry & Cytochemistry* **2009,** *57* (8), 731-739.

[34] Alving, C. R., Antibodies to liposomes, phospholipids and phosphate esters. *Chemistry and Physics of Lipids* **1986,** *40* (2-4), 303-314.

[35] Touboul, D.; Brunelle, A.; Laprevote, O., Mass spectrometry imaging: Towards a lipid microscope? *Biochimie* **2011,** *93* (1), 113-119.

[36] Blanksby, S. J.; Mitchell, T. W., Advances in Mass Spectrometry for Lipidomics. *Annual Review of Analytical Chemistry, Vol 3* **2010,** *3*, 433-465.

[37] McLean, J. A.; Ridenour, W. B.; Caprioli, R. M., Profiling and imaging of tissues by imaging ion mobility-mass spectrometry. *Journal of Mass Spectrometry* **2007,** *42* (8), 1099-1105.

[38] Kim, S. H.; Spangler, G. E., Ion mobility spectrometry / mass spectrometry (IMS/MS) of two structurally different ions having identical ion mass**.** *Analytical Chemistry* **1985,** 57 (2), 567-569.

[39] Woods, A. S.; Ugarov, M.; Egan, T.; Koomen, J.; Gillig, K. J.; Fuhrer, K.; Gonin, M.; Schultz, J. A., Lipid/peptide/nucleotide separation with MALDI-ion mobility-TOF MS. *Analytical Chemistry* **2004,** *76* (8), 2187-2195.

[40] von Helden, G.; Hsu, M.-T.; Gotts, N.; Bowers, M. T., Cobalt-hydrogen (Co+(H2)n) clusters: binding energies and molecular parameters. *Journal of Physical Chemistry* **1993,** *97* (1), 8182-8192.

[41] Mesleh, M. F.; Hunter, J. M.; Shvartsburg, A. A.; Schatz, G. C.; Jarrold, M. F., Structural information from ion mobility measurements: Effects of the long-range potential. *Journal of Physical Chemistry* **1996,** *100* (40), 16082-16086.

[42] von Helden, G.; Wyttenbach, T.; Bowers, M. T., Conformation of macromolecules in the gas phase: use of matrix-assisted laser desorption methods in ion chromatography. *Science* **1995,** *267* (5203), 1483-5.

[43] Wyttenbach, T.; vonHelden, G.; Bowers, M. T., Gas-phase conformation of biological molecules: Bradykinin. *Journal of the American Chemical Society* **1996,** *118* (35), 8355-8364.

[44] Clemmer, D. E.; Hudgins, R. R.; Jarrold, M. F., Naked Protein Conformations: Cytochrome c in the Gas Phase. *Journal of the American Chemical Society* **1995,** *117* (40), 10141-10142.

[45] Mao, Y.; Ratner, M. A.; Jarrold, M. F., One water molecule stiffens a protein. *Journal of the American Chemical Society* **2000,** *122* (12), 2950-2951.

[46] Lee, S.; Wyttenbach, T.; Bowers, M. T., Gas phase structures of sodiated oligosaccharides by ion mobility/ion chromatography methods. *International Journal of Mass Spectrometry and Ion Processes* **1997,** *167/168*, 605-614.

[47] Gidden, J.; Bushnell, J. E.; Bowers, M. T., Gas - Phase Conformations and Folding Energetics of Oligonucleotides: dTG- and dGT-. *Journal of the American Chemical Society* **2001,** *123* (23), 5610-5611.

[48] Gidden, J.; Bowers, M. T., Gas - phase conformations of deprotonated trinucleotides (dGTT-, dTGT-, and dTTG-): the question of zwitterion formation. *Journal of the American Society for Mass Spectrometry* **2003,** *14* (2), 161-170.

[49] Kohtani, M.; Jones, T. C.; Schneider, J. E.; Jarrold, M. F., Extreme stability of an unsolvated alpha-helix. *Journal of the American Chemical Society* **2004,** *126* (24), 7420-7421.

[50] Barran, P. E.; Polfer, N. C.; Campopiano, D. J.; Clarke, D. J.; Langridge-Smith, P. R. R.; Langley, R. J.; Govan, J. R. W.; Maxwell, A.; Dorin, J. R.; Millar, R. P.; Bowers, M. T., Is it biologically relevant to measure the structures of small peptides in the gas - phase? *International Journal of Mass Spectrometry* **2005,** *240* (3), 273-284.

[51] Bernstein, S. L.; Wyttenbach, T.; Baumketner, A.; Shea, J.-E.; Bitan, G.; Teplow, D. B.; Bowers, M. T., Amyloid β - Protein : Monomer Structure and Early Aggregation States of Aβ42 and Its Pro19 Alloform. *Journal of the American Chemical Society* **2005,** *127* (7), 2075-2084.

[52] Gidden, J.; Baker, E. S.; Ferzoco, A.; Bowers, M. T., Structural motifs of DNA complexes in the gas phase. *International Journal of Mass Spectrometry* **2005,** *240* (3), 183-193.

[53] Clowers, B. H.; Hill, H. H., Jr., Mass Analysis of Mobility-Selected Ion Populations Using Dual Gate, Ion Mobility, Quadrupole Ion Trap Mass Spectrometry. *Analytical Chemistry* **2005,** *77* (18), 5877-5885.

[54] Jackson, S. N.; Wang, H. Y. J.; Woods, A. S., Direct tissue analysis of phospholipids in rat brain using MALDI-TOFMS and MALDI-ion mobility-TOFMS. *Journal of the American Society for Mass Spectrometry* **2005,** *16* (2), 133-138.

[55] Jackson, S. N.; Ugarov, M.; Egan, T.; Post, J. D.; Langlais, D.; Schultz, J. A.; Woods, A. S., MALDI-ion mobility-TOFMS imaging of lipids in rat brain tissue. *Journal of Mass Spectrometry* **2007,** *42* (8), 1093-1098.

[56] Jackson, S. N.; Ugarov, M.; Post, J. D.; Egan, T.; Langlais, D.; Schultz, J. A.; Woods, A. S., A Study of Phospholipids by Ion Mobility TOFMS. *Journal of the American Society for Mass Spectrometry* **2008,** *19* (11), 1655-1662.

[57] Fenn, L. S.; McLean, J. A., Biomolecular structural separations by ion mobility-mass spectrometry. *Analytical and Bioanalytical Chemistry* **2008,** *391* (3), 905-909.

[58] Fenn, L. S.; Kliman, M.; Mahsut, A.; Zhao, S. R.; McLean, J. A., Characterizing ion mobility-mass spectrometry conformation space for the analysis of complex biological samples. *Analytical and Bioanalytical Chemistry* **2009,** *394* (1), 235-244.

[59] Wyttenbach, T.; Kemper, P. R.; Bowers, M. T., Design of a new electrospray ion mobility mass spectrometer. *International Journal of Mass Spectrometry* **2001,** *212* (1-3), 13-23.

[60] Dugourd, P.; Hudgins, R. R.; Clemmer, D. E.; Jarrold, M. F., High-resolution ion mobility measurements. *Review of Scientific Instruments* **1997,** *68* (2), 1122-1129.

[61] Giles, K.; Pringle, S. D.; Worthington, K. R.; Little, D.; Wildgoose, J. L.; Bateman, R. H., Applications of a travelling wave-based radio-frequency-only stacked ring ion guide. *Rapid Commun Mass Spectrom* **2004,** *18* (20), 2401-14.

[62] Pringle, S. D.; Giles, K.; Wildgoose, J. L.; Williams, J. P.; Slade, S. E.; Thalassinos, K.; Bateman, R. H.; Bowers, M. T.; Scrivens, J. H., An investigation of the mobility separation of some peptide and protein ions using a new hybrid quadrupole/travelling wave IMS/oa-ToF instrument. *International Journal of Mass Spectrometry* **2007,** *261* (1), 1-12.

[63] Ruotolo, B. T.; Benesch, J. L. P.; Sandercock, A. M.; Hyung, S. J.; Robinson, C. V., Ion mobility-mass spectrometry analysis of large protein complexes. *Nature Protocols* **2008,** *3* (7), 1139-1152.

[64] Williams, J. P.; Scrivens, J. H., Coupling desorption electrospray ionisation and neutral desorption/extractive electrospray ionisation with a travelling-wave based ion mobility mass spectrometer for the analysis of drugs. *Rapid Communications in Mass Spectrometry* **2008,** *22* (2), 187-196.

[65] Buryakov, I. A.; Krylov, E. V.; Nazarov, E. G.; Rasulev, U. K., A New Method of Separation of Mult-Atomic Ions by Mobility at Atmospheric-Pressure Using a High-Frequency Amplitude-Asymmetric Strong Electric-Field *International Journal of Mass Spectrometry and Ion Processes* **1993**, *128*, 143-148.

[66] Krylov, E. V.; Nazarov, E. G.; Miller, R. A., Differential mobility spectrometer: Model of operation. *International Journal of Mass Spectrometry* **2007,** *266*, 76-85.

[67] Shvartsburg, A. A.; Smith, R. D., Fundamentals of Traveling Wave Ion Mobility Spectrometry. *Analytical Chemistry* **2008,** *80* (24), 9689-9699.

[68] Revercomb, H. E.; Mason, E. A., Theory of Plasma Chromatography Gaseous Electrophoresis - Review. *Analytical Chemistry* **1975,** *47* (7), 970-983.

[69] Carr, T. W., *Plasma Chromatography*. Springer-Verlag New York, 1984; p 274.

[70] Mason, E. A.; McDaniel, E. W., Transport Properties of Ions in Gases, John Wiley & Sons, Inc. New York, **1988.**

[71] Koutselos, A. D.; Mason, E. A., Generalized Einstein Relations for Ions in Molecular Gases. *Chemical Physics* **1991,** *153* (3), 351-370.

[72] McDaniel, E. W.; Viehland, L. A., The Transport of Slow Ions in Gases - Experiment, Theory, and Applications. *Physics Reports-Review Section of Physics Letters* **1984,** *110* (5-6), 333-367.

[73] Shvartsburg, A. A.; Jarrold, M. F., An exact hard-spheres scattering model for the mobilities o polyatomic ions. *Chemical Physics Letters* **1996,** *261* (1-2), 86-91.
[74] Wyttenbach, T.; Liu, D. F.; Bowers, M. T., Interactions of the hormone oxytocin with divalent metal ions. *Journal of the American Chemical Society* **2008,** *130* (18), 5993-6000.

[75] Ruotolo, B. T.; Giles, K.; Campuzano, I.; Sandercock, A. M.; Bateman, R. H.; Robinson, C. V., Evidence for macromolecular protein rings in the absence of bulk water. *Science* **2005,** *310* (5754), 1658-1661.

[76] Koeniger, S. L.; Merenbloom, S. I.; Clemmer, D. E., Evidence for many resolvable structures within conformation types of electrosprayed ubiquitin ions. *Journal of Physical Chemistry B* **2006,** *110* (13), 7017-7021.

[77] Case, D. A.; Cheatham, T. E.; Darden, T.; Gohlke, H.; Luo, R.; Merz, K. M.; Onufriev, A.; Simmerling, C.; Wang, B.; Woods, R. J., The Amber biomolecular simulation programs. *Journal of Computational Chemistry* **2005,** *26* (16), 1668-1688.

[78] Mesleh, M. F.; Hunter, J. M.; Shvartsburg, A. A.; Schatz, G. C.; Jarrold, M. F., Structural information from ion mobility measurements: Effects of the long-range potential. *Journal of Physical Chemistry* **1996,** *100* (40), 16082-16086.

[79] von Helden, G.; Hsu, M. T.; Gotts, N.; Bowers, M. T., Carbon Cluster Cations with up to 84 Atoms - Structures, Formation Mechanism, and Reactivity. *Journal of Physical Chemistry* **1993,** *97* (31), 8182-8192.

[80] Wyttenbach, T.; vonHelden, G.; Batka, J. J.; Carlat, D.; Bowers, M. T., Effect of the long-range potential on ion mobility measurements. *Journal of the American Society for Mass Spectrometry* **1997,** *8* (3), 275-282.

[81] Shvartsburg, A. A.; Smith, R. D., Fundamentals of Traveling Wave Ion Mobility Spectrometry. *Analytical Chemistry* **2008,** *80* (24), 9689-9699.

[82] Wallace, A.; Millar, A.; Langridge, J., New structural insights from high-efficiency ion mobility and tandem mass spectrometry. *Nature Methods* **2007**, AN12-AN13.

[83] Hoaglund, C. S.; Valentine, S. J.; Sporleder, C. R.; Reilly, J. P.; Clemmer, D. E., Three-dimensional ion mobility TOFMS analysis of electrosprayed biomolecules. *Analytical Chemistry* **1998,** *70* (11), 2236-2242.

[84] Ruotolo, B. T.; Gillig, K. J.; Woods, A. S.; Egan, T. F.; Ugarov, M. V.; Schultz, J. A.; Russell, D. H., Analysis of phosphorylated peptides by ion mobility-mass spectrometry. *Analytical Chemistry* **2004,** *76* (22), 6727-6733.

[85] Dugourd, P.; Antoine, R.; Breaux, G.; Broyer, M.; Jarrold, M. F., Entropic stabilization of isolated beta-sheets. *Journal of the American Chemical Society* **2005,** *127* (13), 4675-4679.

[86] Thalassinos, K.; Grabenauer, M.; Slade, S. E.; Hilton, G. R.; Bowers, M. T.; Scrivens, J. H., Characterization of Phosphorylated Peptides Using Traveling Wave-Based and Drift Cell Ion Mobility Mass Spectrometry. *Analytical Chemistry* **2009,** *81* (1), 248-254.

[87] Wyttenbach, T.; Bushnell, J. E.; Bowers, M. T., Salt bridge structures in the absence of solvent? The case for the oligoglycines. *Journal of the American Chemical Society* **1998,** *120* (20), 5098-5103.

[88] Liu, D. F.; Wyttenbach, T.; Bowers, M. T., Hydration of mononucleotides. *Journal of the American Chemical Society* **2006,** *128* (47), 15155-15163.

[89] Koomen, J. M.; Ruotolo, B. T.; Gillig, K. J.; McLean, J. A.; Russell, D. H.; Kang, M. J.; Dunbar, K. R.; Fuhrer, K.; Gonin, M.; Schultz, J. A., Oligonucleotide

analysis with MALDI-ion-mobility-TOFMS. *Analytical and Bioanalytical Chemistry* **2002,** *373* (7), 612-617.

[90] Kliman, M.; Vijayakrishnan, N.; Wang, L.; Tapp, J. T.; Broadie, K.; McLean, J. A., Structural mass spectrometry analysis of lipid changes in a Drosophila epilepsy model brain. *Molecular BioSystems* **2010,** *6* (6), 958-966.

[91] Ruotolo, B. T.; McLean, J. A.; Gillig, K. J.; Russell, D. H., Peak capacity of ion mobility mass spectrometry: the utility of varying drift gas polarizability for the separation of tryptic peptides. *Journal of Mass Spectrometry* **2004,** *39* (4), 361-367

[92] McLean, J. A.; Ridenour, W. B.; Caprioli, R. M., Profiling and imaging of tissues by imaging ion mobility-mass spectrometry. *Journal of Mass Spectrometry* **2007,** *42* (8), 1099-1105.

[93] Ridenour, W. B.; Kliman, M.; McLean, J. A.; Caprioli, R. M., Structural Characterization of Phospholipids and Peptides Directly from Tissue Sections by MALDI Traveling-Wave Ion Mobility-Mass Spectrometry. *Analytical Chemistry* **2010,** *82* (5), 1881-1889.

[94] Trimpin, S.; Tan, B.; Bohrer, B. C.; O'Dell, D. K.; Merenbloom, S. I.; Pazos, M. X.; Clemmer, D. E.; Walker, J. M., Profiling of phospholipids and related lipid structures using multidimensional ion mobility spectrometry-mass spectrometry. *International Journal of Mass Spectrometry* **2009,** *287* (1-3), 58-69.

[95] McLean, J. A., The Mass-Mobility Correlation Redux: The Conformational Landscape of Anhydrous Biomolecules. *Journal of the American Society for Mass Spectrometry* **2009,** *20* (10), 1775-1781.

[96] Kim, H. I.; Kim, H.; Pang, E. S.; Ryu, E. K.; Beegle, L. W.; Loo, J. A.; Goddard, W. A.; Kanik, I., Structural Characterization of Unsaturated Phosphatidylcholines Using Traveling Wave Ion Mobility Spectrometry. *Analytical Chemistry* **2009,** *81* (20), 8289-8297.

CHAPTER II

Ion Mobility-Mass Spectrometry

Conformational Landscape of Anhydrous Biomolecules.

2.1 Introduction

Contemporary biomolecular studies often have to focus on structural and functional characterization of one biological class at a time, and then try to uncover a system wide view of the relationships between the different classes of biomolecules.[1,2] Ideally, all biomolecular classes would be studied simultaneously and their interdependences preserved. There are several key advantages to performing simultaneous biomolecular measurements. First, such an approach would provide a rapid, high throughput method of analysis. Second, sample losses and analysis artifacts would be minimized, and last, biological context would be preserved.

Ion mobility-mass spectrometry (IM-MS) has proven to be a valuable tool in contemporary life science research.[3,4] In ion mobility (IM), biomolecular separations occur on the basis of directed ion-neutral collisions with a background gas, where the rate of movement of biomolecular ions is proportional to their apparent gas phase surface area. Thus, when coupled with mass spectrometry, IM provides separation on the basis of structure and mass spectrometry on the basis of mass to charge (m/z).

IM also affords structural interpretation when empirically determined gas phase collision cross-sections (CCS) are compared with a large pool of molecular dynamics (MD) generated structures whose computed CCSs match the empirical result. Unlike the atomic detail of X-ray crystallography and nuclear magnetic resonance, IM-MS structural interpretation only provides a relatively low resolution, coarse-grained view of the structural reasons for the observed biomolecular separations. However, IM-MS can provide this information for small sample quantities, often directly from complex biological mixtures (*e.g.*, cell lysates, cells, tissues).

Prior studies utilizing IM-MS have first focused on structural characterization of peptides[5] and proteins,[6,7] carbohydrates[8] and more recently oligonucleotides[9,10] and lipids.[11,12,13] Impressive work has also been performed in IM-MS characterization of large protein complexes,[14] its application in imaging of thin tissue sections[15,16] and comprehensive proteomics.[17,18] IM-MS has gradually been shown to provide biomolecular separations on the basis of structure, since different biomolecular classes can be readily resolved based on differences in their gas-phase densities, where the gas phase density of lipids<peptides<carbohydrate<nucleotides.[11]

In this work, I contributed to the study of IM-MS conformation space of biomolecules by providing a database of lipid gas phase collision cross-sections. My colleagues explored the conformation space of oligonucleotides, carbohydrates, and performed statistical analysis of where their signals fall on the ion mobility *vs.* m/z conformational space. To illustrate the information

enhancement of molecular dynamics, I performed computational analysis for the observed IM separation of two isobaric oligonucleotide tetramers.

2.2 Experimental

2.2.1 Samples and Preparation

2.2.1.1 Oligonucleotides

Oligonucleotide standards, matrix (2,4,6-trihydroxyacetophenone, THAP), and ammonium citrate were purchased from Sigma (St. Louis, MO, USA) and used for MALDI-IM-MS CCS studies without further purification. Oligonucleotide standards were initially dissolved in distilled deionized (DDI) water (18 MΩ cm, Millipore). Matrix solutions were prepared fresh daily by mixing 50 mg/mL THAP and 50 mg/mL ammonium citrate at a 9:1 ratio (v/v) in DDI. Samples were then prepared for MALDI by mixing 10 µL (10 nmoles) of oligonucleotide solution with 30 µL (10,000 nmoles) matrix solution. An aliquot of 3 µL of the mixture was then spotted onto a MALDI plate and vacuum- dried prior to MALDI-IM-MS analysis.

2.2.1.2 Carbohydrates

For MALDI-IM-MS measurements of CCSs of individual standards, Lacto-N-fucopentaoses (LNFP) 1 and LNFP2 from human milk were obtained from Dextra Laboratories (Reading, UK); LNFP3, LNFP5, Lacto-N-difucohexaose (LNDFH) 1, and LNDFH2 were obtained from V Labs (Covington, LA, USA). Synthetic glycans, Gala3-type1, P1, H-type2-LN-LN, P1 antigen-sp, Di-LeA, P1

penta, LNT, Lec-Lec, Tri-LacNAc, GNLNLN, and 3′SLN-Lec were obtained through the Carbohydrate Synthesis/Protein Expression Core of The Consortium for Functional Glycomics. 2,5- Dihydroxybenzoic acid (DHB), NaCl, and all other reagents were purchased from Sigma and used without further purification. The matrix used for MALDI-IM-TOFMS was saturated DHB in 50% ethanol. The matrix and analyte were combined in a 1:1 volume ratio (or 200:1 molar ratio). NaCl was added to make a final concentration of 0.1% for purposes of converting all signals to those corresponding to sodium-coordinated ions. The samples were prepared using the dried droplet method.[19]

2.2.1.3 Lipids

For proof-of-concept experiments five lyophilized lipid extracts, two sphingolipids, sphingomyelins (porcine brain) and cerebrosides (porcine brain), and three phospholipids, phosphatidylcholines (chicken egg), phosphatidylserines (porcine brain), and phosphatidylethanolamines (chicken egg), were obtained from Avanti Lipids (Birmingham, AL, USA). Each of these extracts were individually dissolved in a 2:1v/v CHCl3/ MeOH mixture to yield 2 mM solutions. DHB was dissolved in 50% ethanol to yield a 200 mM solution. The individual lipid extracts were premixed with DHB matrix solution in a 1:10 ratio (v/v) and manually spotted onto a 100-well steel MALDI plate and flash-evaporated under vacuum.[19] Identification of lipid species was aided by information available from Avanti Lipids,[20] the LIPIDMAPS database,[21] and previously published identification of MALDI lipid spectra.[12]

2.2.2 Instrumentation

MALDI-IM-TOFMS measurements were performed with MALDI ionization at the pressure of the mobility drift cell (3.8 Torr) with a frequency-tripled Nd-YLF (349 nm) laser (Explorer, Newport/Spectra-Physics, Mountain View, CA, USA). Once the ionized species moved through the helium filled drift cell under the influence of a weak electric field, they were guided by ion optics into the low-pressure region of a TOFMS. Two-dimensional spectra (arrival time versus m/z) of each sample were analyzed and compared using custom visualization software (Ionwerks, Houston, TX, USA) developed on the IDL platform (ITT Visual Information Solutions, Boulder, CO, USA). Mass calibration of the instrument was performed externally using a mixture of C60 and C70.

2.2.3 Molecular Dynamics Calculations

Computational starting structures of TGC and CGA trinucleotides were modified in the LEaP module of AMBER 9.0.[22] Physical presence of protons neutralizing the negative charge of phosphates was deemed essential to the modeling of hydrogen bonding interactions. Protons were added to one oxygen of each phosphate of the TGC and CGA trinucleotides, and to the basic nitrogen of the guanine base. Quantum mechanical (QM) Hartree-Fock geometry geometry optimization and electrostatic potential calculations of protonated trinucleotides were performed using Gaussian 2003 with a 6-31G* basis set.[23] Partial charges were derived by fitting the QM electrostatic potential to an atom-

centered point charge model using the RESP procedure.[24] Terminal nucleosides A and T were connected to the trinucleotides TGC and CGA in LEaP to yield TGCA and CGAT tetranucleotides with a +1 net charge. Standard AMBER 99 parameters were used for bond, angle, dihedral, and van der Waals interactions. For molecular dynamics (MD) simulation, the AMBER atom type of the phosphate protons was changed from H to HS. The smaller van der Waals radius of the HS atom type resolved the instability of the 1-4 electrostatic interaction energy term observed with the H atom type. Molecular dynamics (MD) simulations of tetranucleotide ions were performed with the SANDER module of AMBER 9[25] using a high temperature conformational sampling protocol. In this approach, each examined oligonucleotide ion was gradually heated to 1000 Kelvin and allowed to sample high-energy conformations at this temperature for nine nanoseconds of simulation time. Utilizing a modified simulated annealing approach, 24000 structures were extracted throughout this high temperature trajectory, gradually cooled to 50 Kelvin, and subsequently energy minimized. Mobcal[26,27] was used to determine the projection approximation (PA) collision cross-section of cooled oligonucleotide conformational snapshots obtained from the modified simulated annealing procedure. Low energy (*i.e.*, potential energy lower than the average energy of all simulated structures) MD snapshots whose collision cross-section matched experimental values were chosen for cluster analysis. Superposition and clustering programs available and partially developed at the Vanderbilt Center for Structural Biology were used to separate structures into clusters based on conformational similarity.[28]

2.3 Results and Discussion

Past isolated studies of peptides, proteins, nucleotides and lipids by IM-MS revealed that individual biomolecular classes occupy relatively distinct regions in the two-dimensional IM-MS arrival time or CCS *vs.* m/z plot.[11] Since the gas phase packing density of biomolecules is largely guided by constraining intramolecular interactions, such as hydrogen bonding, pi-pi stacking, and salt bridging, the two dimensional representation is often referred to as the IM-MS conformation space. Better knowledge of where different biomolecular signals occur in the IM-MS conformation space can greatly aid the identification of unknown signals.

In this work we combined CCS *vs.* m/z datasets of singly charged ion signals from oligonucleotide, carbohydrate and lipid standards (n=96,192,53, respectively). These results were compared to a large database of previously reported CCS values of singly charged peptide standards (n=610)[29] and are summarized in Figure 2.1. In agreement with previous reports, the various classes of analytes occupy different regions of IM-MS conformation space. Relative collision cross-sections (CCSs) at a particular m/z decrease in the following order: lipids>peptides>carbohydrates>oligonucleotides. The separation of signals indicates different gas phase packing density of each biomolecular class. Since CCS, as area, scales as length squared and mass scales as length cubed, we decided to use the logarithmic function to fit the CCS *vs.* m/z data.
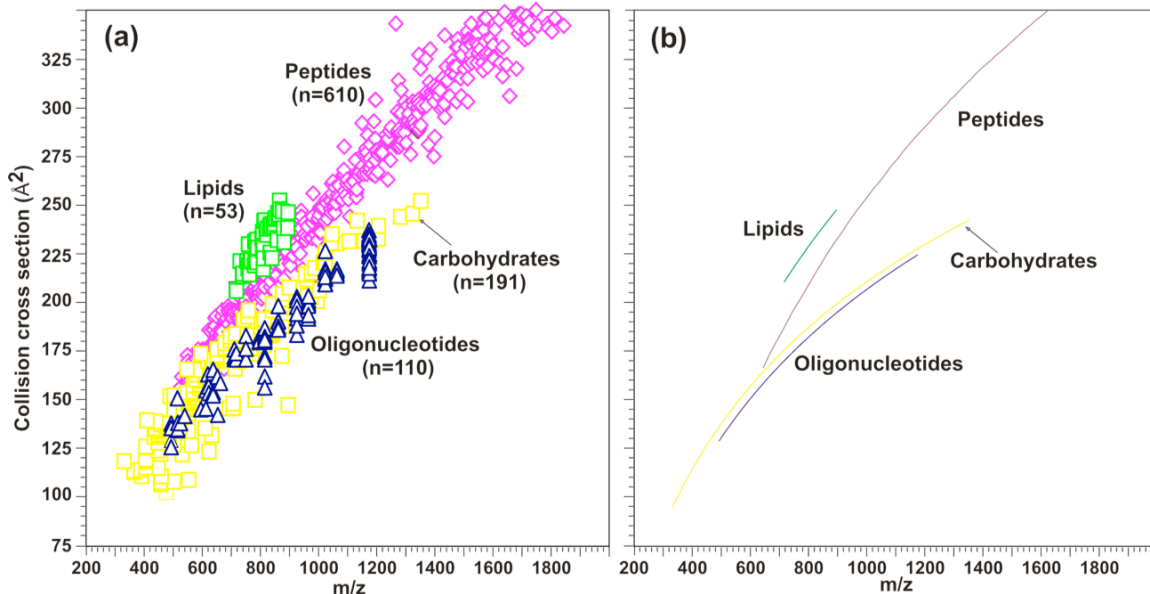
Figure 2.1 MALDI-IM-MS CCS *vs*. m/z plot of individually analyzed lipid, carbohydrate and oligonucleotide standards, here compared to previously published library of peptide CCS values.[29] **(a).** Differences in intramolecular packing of different types of biomolecules results in different correlations of CCS at a given *m/z.* Phospholipids with fatty acid tails tend to pack the least tightly in vacuum among other biomolecules due to the lack of strong intramolecular interactions between the fatty acid tails and the headgroup region. **(b).** A 2D plot of MALDI-IM-MS conformation space: average logarithmic regression fit functions are based on the CCS datasets for lipids (n=53), peptides (n=610),[29] carbohydrates (n=191), and oligonucleotides (n=110). With kind permission from Springer Science+Business Media: *Analytical and Bioanalytical Chemistry*. "Characterizing Ion Mobility-Mass Spectrometry (IM-MS) Conformation Space for the Analysis of Complex Biological Samples." 394, 2009, 235-244, L.S. Fenn, M. Kliman, A. Mahsut, S.R. Zhao, J.A. McLean, adapted from Figure 1.

Among the available fit functions, the logarithmic fit best approximates the decreasing incremental increase of CCS at the limit of high mass. The average regression fit for each biomolecular dataset is shown in Figure 2.1 (b). The distribution, of CCS values around the average logarithmic regressions is presented in Figure 2.2. Whereas a previous study of peptide conformation

space found the residual deviation from a linear regression fit of 2.5% (±σ),[30] the

residuals from the logarithmic regression of a larger library of 610 peptide signals

used in this work have a relative deviation of 7.33% (±σ).
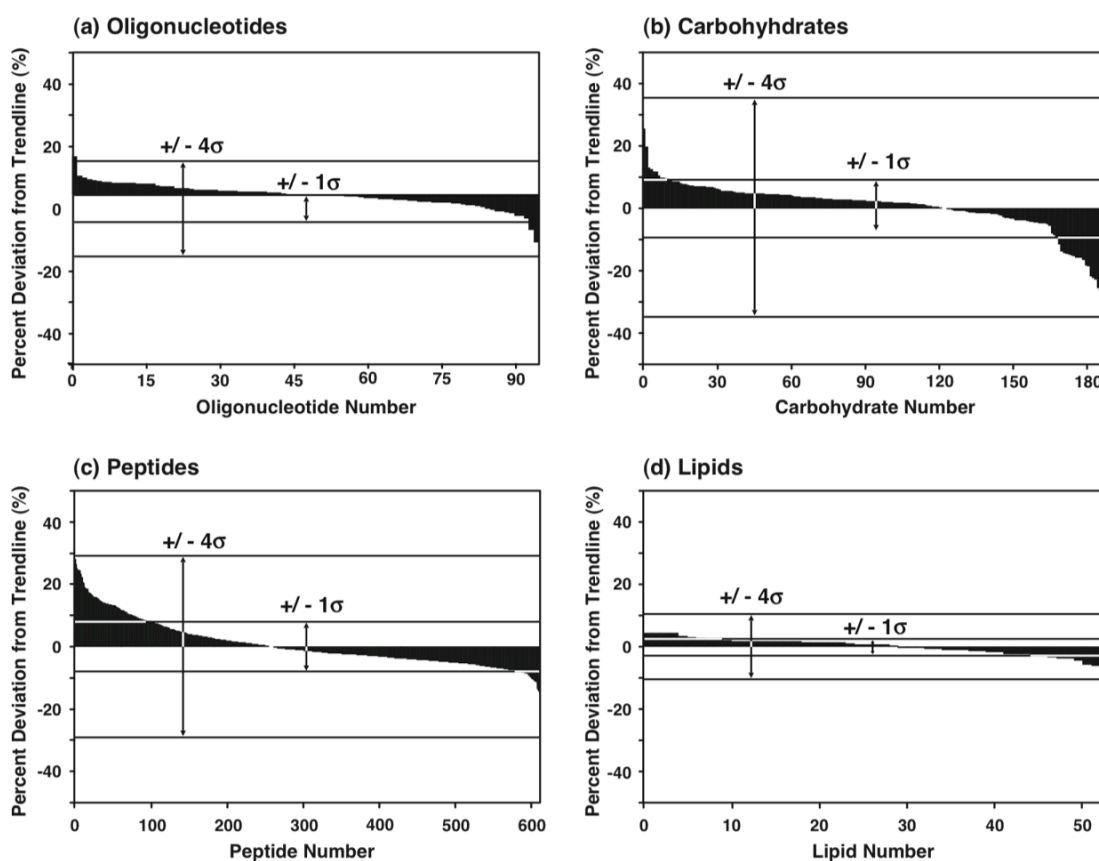
Figure 2.2 Residual plots of biomolecular standard CCS values around their logarithmic regression fit functions presented in Figure 2.1 (b). The plots represent the percent relative deviation for the reported signals ordered by descending values of percent relative deviation from left to right. Calculated variance from each of the residual plots is 3.70, 8.81, 7.33, and 2.64 for oligonucleotides, carbohydrates, peptides, and lipids, respectively. With kind permission from Springer Science+Business Media: *Analytical and Bioanalytical Chemistry*. "Characterizing Ion Mobility-Mass Spectrometry (IM-MS) Conformation Space for the Analysis of Complex Biological Samples." 394, 2009, 235-244, L.S. Fenn, M. Kliman, A. Mahsut, S.R. Zhao, J.A. McLean, Figure 2.

Statistical analysis of lipid, carbohydrate, and oligonucleotide CCS values yielded $\pm\sigma$ relative deviation values of 2.64%, 8.81%, and 3.70%, respectively. Thus, the order of biomolecular classes based on increasing standard deviation of each respective dataset is lipids<oligonucleotides<peptides<carbohydrates.

Structural analysis of each biomolecular class analyzed provides an intriguing explanation for the observed amount of variability. The relative narrowness of the distribution of lipid signals may reflect the limited number of analytes tested but may also be indicative of the structural simplicity of the examined lipids (*i.e.*, in all cases here lipids consist of long hydrophobic fatty acids and relatively smaller polar head groups), which limits the number of distinct structural forms they can adopt. Similarly, low standard deviation of the oligonucleotide dataset may be a result of the limited number of monomeric units that comprise this class. In contrast, both carbohydrates and peptides have greater structural diversity, which arises from the larger number of monomeric units and the potential for significant branching and cyclization.

From a more fundamental perspective of gas phase packing efficiency, it is the prevailing intramolecular folding forces that dictate the structural diversity of different biomolecular classes. Even this, more fundamental perspective, provides a valid explanation for the varying diversity observed, especially in combination with in-depth molecular modeling of various biomolecular ions. Such modeling can effectively elucidate the relative contibutions of various structurally constraining forces, such as hydrogen bonding, pi-pi stacking, salt bridging, or even van der Waals interactions, to the structural diversity of each class of

compounds. The relative contributions of these intramolecular forces are strikingly different in each biomolecular class, again primarily because of the difference in chemical composition, the number of monomeric units, and the type of linkages that comprise each.

In Figure 2.3, we show the residuals from each regression analysis in histogram form. The histograms profiles for lipids and oligonucleotides, the two classes with smallest standard deviations, appear to have a Gaussian distribution, whereas he broader profiles of carbohydrates and peptides appear to have a skewed distribution, carbohydrates toward signals with lower CCSs than the average logarithmic fit, peptides toward signals with higher CCSs than the average fit. Clearly, despite the fact the logarithmic regression is mathematically the most appropriate, it seems to overestimate the relative frequency of signals deviating from the average correlation of carbohydrates and peptides. Importantly, fitting this data to a polynomial function does result in more Gaussian histograms, but does not capture the mathematical limit of high mass best approximated by the logarithmic fit.

The presented data describes the conformation space of biomolecules over a relatively narrow range of masses and it should therefore not be used to approximate CCS values of biomolecular signals of greater mass. At present, we lack sufficient experimental data for, for example, the transition region from peptides to ordered protein complexes in the mass range of 3kDa to 200kDa. The correlation between CCS and m/z in this region cannot yet be established. Nevertheless, the correlations presented provide a strong guide for identification

of unknown signals in the analysis of biological samples in the mass range up to

2kDa, a typical range for proteomic and lipidomic experiments.
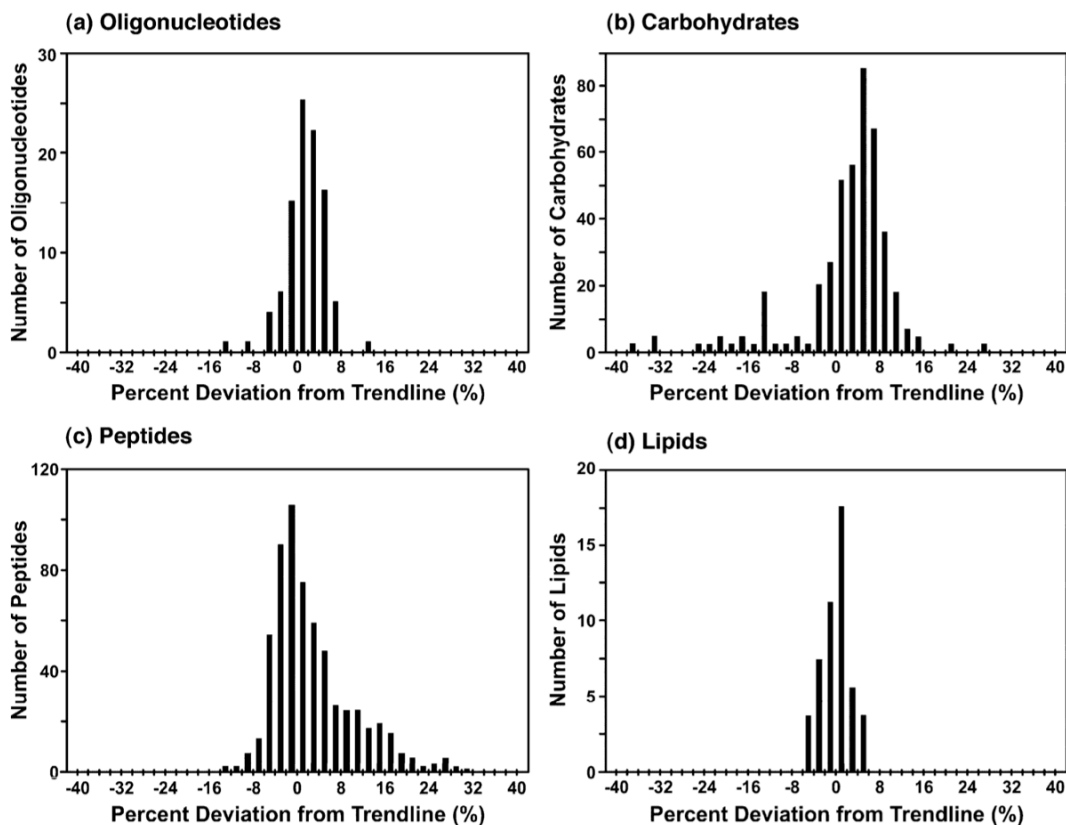
Figure 2.3 Histograms of statistical frequency of analyte signal deviations from the logarithmic regressions for each molecular class shown in Figure 1 (b). With kind permission from Springer Science+Business Media: *Analytical and Bioanalytical Chemistry*. "Characterizing Ion Mobility-Mass Spectrometry (IM-MS) Conformation Space for the Analysis of Complex Biological Samples." 394, 2009, 235-244, L.S. Fenn, M. Kliman, A. Mahsut, S.R. Zhao, J.A. McLean, Figure 3.

The historgrams in Figure 2.3 have approximately normal distributions, yet

we should not fail to recognize that each class contains deviations from the

average correlation that are due to specific structural forms of each class. For

example, peptide secondary structure is often retained in the gas phase,[31,32,33,34]

the branching ratio and glycosidic linkage variation of carbohydrates[35,36] can be expected to have a effect on mobility, as can lipid backbone and headgroup differences as show in Chapter 3.
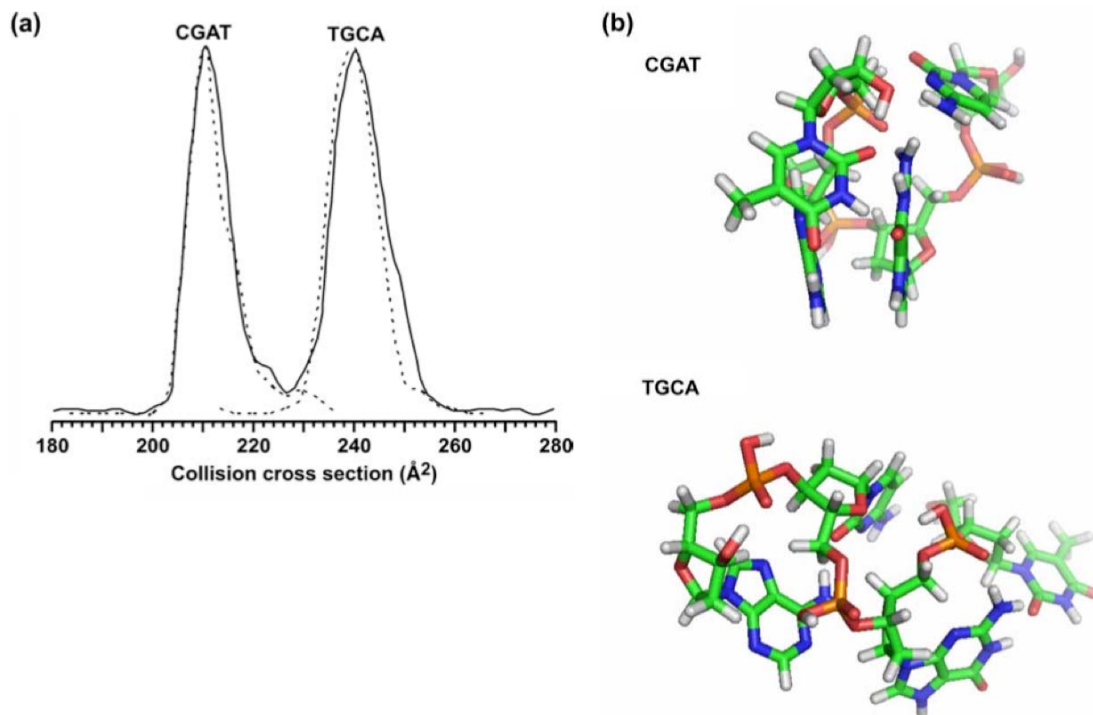
Figure 2.4 (a) CCS profile of the IM separation of a mixture of two same mass tetranucleotide species, CGAT and TGCA (m/z = 1,174.3 Da). The solid line corresponds to an IM CCS profile for the mixture of the two components. Dashed lines correspond to IM CCS profile for each oligonucleotide analyzed separately. **(b)** Representative structures for the molecular dynamics output for each of the two oligonucleotide species. For each tetramer I calculated close to 21,000 total structures among which 667 and 1,405 structures were considered low energy and matched the empirically determined CCS to within ±2.5 Å^2 (*i.e.*, ±1%). The representative structures were obtained by root mean squared (RMS) analysis. With kind permission from Springer Science+Business Media: *Analytical and Bioanalytical Chemistry*. "Characterizing Ion Mobility-Mass Spectrometry (IM-MS) Conformation Space for the Analysis of Complex Biological Samples." 394, 2009, 235-244, L.S. Fenn, M. Kliman, A. Mahsut, S.R. Zhao, J.A. McLean, Figure 4.

To illustrate the complexity that can arise within a probability conformation space distribution profile of a single biomolecular class, we show in Figure 4 the separation of two oligonucleotides composed of the same four monomeric units, but of permuted sequence (*i.e.*, CGAT and TGCA). The two oligonucleotides have the same mass, yet are nearly baseline resolved on the basis of structure in IM (Figure 4(a)). Figure 4(b) shows representative structures of the conformations these two oligomers preferentially adopt in the gas phase. The two single stranded DNA tetramers adopt structures with strikingly different average gas phase surface areas. CGAT adopts a compact structure dominated by base-stacking, whereas the TGCA structure is more extended, and exhibits extensive hydrogen bonding. In a similar fashion molecular dynamics simulations can provide a fine structure level of information about the preferential conformations within broader biomolecular correlations of other classes such as carbohydrates, peptides, proteins and lipids. Chapter 3 details an application of the molecular dynamics protocol to IM separation of glycerophospholipids and sphingolipids.

2.4 Conclusions

The analysis presented in this work forms a broad view of the conformation dependent landscape of different biomolecular classes. This study provides an initial general metric for assigning unknown signals to particular classes based on where the unknowns occur in the conformation space. Molecular dynamics based analysis of fine structure can be used effectively to

elucidate various trends within each biomolecular class related to sub-populations of structurally similar bioanalytes. In case of peptides these sub-populations can occur due to post-translational modification, retained secondary structure, metal coordination, in case of lipids, such as glycerophopholipids *vs.* sphingolipids as described in Chapter 3, the sub-populations can be resolved based on fine structure detail of the lipid backbone and metal coordination. Additional characterization of the IM-MS conformation space of different biomolecules will likely open new avenues for rapid integrated systems biology and life-science research.

2.5 Acknowledgements

REFERENCES

[1] Peterson, R. T., Chemical biology and the limits of reductionism. *Nature Chemical Biology* **2008,** *4* (11), 635-638.

[2] Simon, G. M.; Cravatt, B. F., Challenges for the 'chemical-systems' biologist. *Nature Chemical Biology* **2008,** *4* (11), 639-642.

[3] Ruotolo, B. T.; Benesch, J. L. P.; Sandercock, A. M.; Hyung, S. J.; Robinson, C. V., Ion mobility-mass spectrometry analysis of large protein complexes. *Nature Protocols* **2008,** *3*, 1139-1152.

[4] Wallace, A.; Millar, A.; Langridge, J., New structural insights from high-efficiency ion mobility and tandem mass spectrometry. *Nature Methods* **2007**, AN12-AN13.

[5] Wyttenbach, T.; vonHelden, G.; Bowers, M. T., Gas-phase conformation of biological molecules: Bradykinin. *Journal of the American Chemical Society* **1996,** *118* (35), 8355-8364.

[6] Clemmer, D. E.; Hudgins, R. R.; Jarrold, M. F., Naked Protein Conformations: Cytochrome c in the Gas Phase. *Journal of the American Chemical Society* **1995,** *117* (40), 10141-10142.

[7] Mao, Y.; Ratner, M. A.; Jarrold, M. F., One water molecule stiffens a protein. *Journal of the American Chemical Society* **2000,** *122* (12), 2950-2951.

[8] Lee, S.; Wyttenbach, T.; Bowers, M. T., Gas phase structures of sodiated oligosaccharides by ion mobility/ion chromatography methods. *International Journal of Mass Spectrometry and Ion Processes* **1997,** *167/168*, 605-614.

[9] Gidden, J.; Bushnell, J. E.; Bowers, M. T., Gas - Phase Conformations and Folding Energetics of Oligonucleotides: dTG- and dGT-. *Journal of the American Chemical Society* **2001,** *123* (23), 5610-5611.

[10] Gidden, J.; Bowers, M. T., Gas - phase conformations of deprotonated trinucleotides (dGTT-, dTGT-, and dTTG-): the question of zwitterion formation. *Journal of the American Society for Mass Spectrometry* **2003,** *14* (2), 161-170.

[11] Woods, A. S.; Ugarov, M.; Egan, T.; Koomen, J.; Gillig, K. J.; Fuhrer, K.; Gonin, M.; Schultz, J. A., Lipid/peptide/nucleotide separation with MALDI-ion mobility-TOF MS. *Analytical Chemistry* **2004,** *76* (8), 2187-2195.

[12] Jackson, S. N.; Wang, H. Y. J.; Woods, A. S., In situ structural characterization of glycerophospholipids and sulfatides in brain tissue using MALDI-MS/MS. *Journal of the American Society for Mass Spectrometry* **2007,** *18* (1), 17-26.

[13] Jackson, S. N.; Ugarov, M.; Post, J. D.; Egan, T.; Langlais, D.; Schultz, J. A.; Woods, A. S., A Study of Phospholipids by Ion Mobility TOFMS. *Journal of the American Society for Mass Spectrometry* **2008,** *19* (11), 1655-1662.

[14] Ruotolo, B. T.; Giles, K.; Campuzano, I.; Sandercock, A. M.; Bateman, R. H.; Robinson, C. V., Evidence for macromolecular protein rings in the absence of bulk water. *Science* **2005,** *310* (5754), 1658-1661.

[15] Jackson, S. N.; Ugarov, M.; Egan, T.; Post, J. D.; Langlais, D.; Schultz, J. A.; Woods, A. S., MALDI-ion mobility-TOFMS imaging of lipids in rat brain tissue. *Journal of Mass Spectrometry* **2007,** *42* (8), 1093-1098.

[16] McLean, J. A.; Ridenour, W. B.; Caprioli, R. M., Profiling and imaging of tissues by imaging ion mobility-mass spectrometry. *Journal of Mass Spectrometry* **2007,** *42* (8), 1099-1105.

[17] Valentine, S. J.; Plasencia, M. D.; Liu, X. Y.; Krishnan, M.; Naylor, S.; Udseth, H. R.; Smith, R. D.; Clemmer, D. E., Toward plasma proteome profiling with ion mobility-mass spectrometry. *Journal of Proteome Research* **2006,** *5* (11), 2977-2984.

[18] Liu, X. Y.; Valentine, S. J.; Plasencia, M. D.; Trimpin, S.; Naylor, S.; Clemmer, D. E., Mapping the human plasma proteome by SCX-LC-IMS-MS. *Journal of the American Society for Mass Spectrometry* **2007,** *18* (7), 1249-1264.

[19] Karas, M.; Hillenkamp, F., Laser desorption ionization of proteins with molecular masses exceeding 10,000 daltons. *Analytical Chemistry* **1988,** *60* (20), 2299-2301.

[20] Avanti Polar Lipids http://www.avantilipids.com/ (accessed 2007, 2008).

[21] Sud, M.; Fahy, E.; Cotter, D.; Brown, A.; Dennis, E. A.; Glass, C. K.; Merrill, A. H.; Murphy, R. C.; Raetz, C. R. H.; Russell, D. W.; Subramaniam, S., LMSD: LIPID MAPS structure database. *Nucleic Acids Research* **2007,** *35*, D527-D532.

[22] Case, D. A.; Cheatham, T. E.; Darden, T.; Gohlke, H.; Luo, R.; Merz, K. M.; Onufriev, A.; Simmerling, C.; Wang, B.; Woods, R. J., The Amber biomolecular simulation programs. *Journal of Computational Chemistry* **2005,** *26* (16), 1668-1688.

[23] *Gaussian 03*, version 2003.D.01; Gaussian, Inc.: Wallingford, CT; (accessed 2008, 2009).

[24] Bayly, C. I.; Cieplak, P.; Cornell, W. D.; Kollman, P. A., A Well-behaved Electrostatic Potential Based Method Using Charge Restraints for Deriving Atomic Charges – The RESP Model. *Journal of Physical Chemistry* **1993,** *97* (40), 10269-10280.

[25] *AMBER Molecular Modeling Package*, version 9; University of California: San Francisco; (accessed 2008).

[26] Mesleh, M. F.; Hunter, J. M.; Shvartsburg, A. A.; Schatz, G. C.; Jarrold, M. F., Structural information from ion mobility measurements: Effects of the long-range potential. *Journal of Physical Chemistry* **1996,** *100* (40), 16082-16086.

[27] Shvartsburg, A. A.; Jarrold, M. F., An exact hard-spheres scattering model for the mobilities of polyatomic ions. *Chemical Physics Letters* **1996,** *261* (1-2), 86-91.

[28] *Suppose – superposition software*, version 2006; Vanderbilt University: Nashville, TN; (accessed 2008, 2009).; *OC - A cluster analysis program*, version 2002; University of Dundee, Scotland, UK; (accessed 2008, 2009).

[29] Tao, L.; McLean, J. R.; McLean, J. A.; Russell, D. H., A collision cross-section database of singly-charged peptide ions. *Journal of the American Society for Mass Spectrometry* **2007,** *18* (7), 1232-1238.

[30] Ruotolo, B. T.; McLean, J. A.; Gillig, K. J.; Russell, D. H., Peak capacity of ion mobility mass spectrometry: the utility of varying drift gas polarizability for the separation of tryptic peptides. *Journal of Mass Spectrometry* **2004,** *39* (4), 361-367.

[31] Hoaglund-Hyzer, C. S.; Counterman, A. E.; Clemmer, D. E., Anhydrous protein ions. *Chemical Reviews* **1999,** *99* (10), 3037-3079.

[32] Jarrold, M. F., Peptides and proteins in the vapor phase. *Annual Review of Physical Chemistry* **2000,** *51*, 179-207.

[33] Wyttenbach, T.; Bowers, M. T., Gas-phase conformations: The ion mobility/ion chromatography method. *Modern Mass Spectrometry* **2003,** *225*, 207-232.

[34] Barran, P. E.; Polfer, N. C.; Campopiano, D. J.; Clarke, D. J.; Langridge-Smith, P. R. R.; Langley, R. J.; Govan, J. R. W.; Maxwell, A.; Dorin, J. R.; Millar, R. P.; Bowers, M. T., Is it biologically relevant to measure the structures of small

peptides in the gas - phase? *International Journal of Mass Spectrometry* **2005,** *240* (3), 273-284.

[35] Dwivedi, P.; Wu, C.; Matz, L. M.; Clowers, B. H.; Siems, W. F.; Hill, H. H., Gas-phase chiral separations by ion mobility spectrometry. *Analytical Chemistry* **2006,** *78* (24), 8200-8206.

[36] Isailovic, D.; Kurulugama, R. T.; Plasencia, M. D.; Stokes, S. T.; Kyselova, Z.; Goldman, R.; Mechref, Y.; Novotny, M. V.; Clemmer, D. E., Profiling of human serum glycans associated with liver cancer and cirrhosis by IMS-MS. *Journal of Proteome Research* **2008,** *7* (3), 1109-1117.

CHAPTER III

Structural Selectivity of Anhydrous Sphingolipids and

Glycerophospholipids in Ion Mobility-Mass Spectrometry Analysis

3.1 Introduction

In the last decade, mass spectrometry (MS) has enabled the comprehensive characterization of the myriad lipid structures and their structure specific functions,[1,2,3] building upon prior fundamental lipid research.[4,5,6,7] Lipidomics is still a relatively young discipline yet is quickly progressing through enhancements in the data acquisition,[8] bioinformatics,[9] and systems biology approaches[10] which have paralleled the development of the other omics initiatives.

The discovery of the enormous diversity of lipid structures[11] created an ongoing analytical challenge that requires the adoption of selective separation strategies for the deconvolution of complex lipid MS data. The chief technological advances to date include: (i) tailored condensed phase separations coupled to MS,[12] (ii) tandem mass spectrometry strategies,[13,14] (iii) standardized lipid nomenclature,[15] (iv) comprehensive lipid database construction,[16] (v) synthesis of lipid standards,[17] and (vi) integration of bioinformatics towards automation of data analysis.[18,19] Collectively, these initiatives are advancing lipidomics towards absolute quantitation and systems biology integration.[20] These advances target

the key analytical challenges in lipid analysis. Firstly, the majority of naturally occurring lipid signals occur over relatively narrow mass ranges and can often suffer from isobaric interferences (*i.e.*, different lipids possessing the same nominal mass). Secondly, lipids present in high concentration partially or fully suppress the detection of numerous important low abundance lipids.[21,22] Lastly, the identification of lipid signals from complex biological samples is often hindered by the detection of endogenous and exogenous chemical noise.[23]

An emerging technology which has only recently been applied in lipid analysis is ion mobility-mass spectrometry (IM-MS).[24,25] In the first comprehensive MALDI IM-MS study of phospholipids, Jackson *et al.*[26] demonstrated that specific lipid species are resolved in the ion mobility analysis based on the type of headgroup and the number of carbons and double bonds present in the phospholipids' fatty acid subdomains. This study also reported intriguing differences in gas-phase ion mobility and ionization efficiency based on adduction of lipid ions to different alkali metals (Li^+, Na^+, K^+, Cs^+). Trimpin, *et al.*[27] and Kim *et al.*[28] have investigated phospholipids and N-acyl amino acids by using ESI IM-MS. Trimpin *et al.* reported that the same sphingomyelin (SM) lipid cationized with H^+, Na^+, K^+ and NH_4^+ appears to have indistinguishable gas-phase ion mobilities (referred to as isodrifts). Jackson *et al.* have also previously shown that cationization of SM to the smaller alkali metals (Na^+, K^+, Rb^+) does not lead to significant mobility shifts, while cationization with the larger Cs^+ significantly shifts the SM lipid signal in the ion mobility dimension away from the ions adducted with the smaller alkali metals.

I report here the results of MALDI IM-MS study of five abundant mammalian phospholipids, three glycerophospholipids: phosphatidylcholine (PtdCho), phosphatidylethanolamine (PtdEtn), phosphatidylserine (PtdSer), and two sphingolipids: choline headgroup sphingomyelin (SM) and galactocerebroside (CB). Based on mobility measurements, I derived gas-phase collision cross-section values for each identified IM-MS lipid signal and then used computational modeling to derive a structural interpretation for the observed mobility resolution of glycerophospholipids and sphingolipids.

Consistent with the observations of Jackson *et al.*[26] and Trimpin *et al.*,[27] I confirm the ability of IM-MS to separate lipids in mobility space on the basis of fatty acid chain length, the number of double bonds, and type of headgroup. These findings are extended by a more general observation of ion mobility separation of glycerophospholipids and sphingolipids. Thus, gas-phase ion mobility separation of lipids appears feasible not only on the basis of differences in headgroup and fatty acids but also on the basis of structural differences of the main lipid backbone (*i.e.*, glycerol *vs.* sphingosine).

3.2 Experimental

3.2.1 Lipid samples and preparation

For proof-of-concept experiments five lyophilized lipid extracts were purchased from Avanti Lipids, Inc. (Birmingham, AL) and individually dissolved in 2:1 chloroform:methanol mixture to yield 2mM solutions. The lipid extracts

included the sphingolipids, sphingomyelin (SM, porcine brain), and cerebroside (CB, porcine brain) and the phospholipids, phosphatidylcholine (PtdCho, chicken egg), phosphatidylserine (PtdSer, porcine brain), and phosphatidylethanolamine (PtdEtn, chicken egg). The MALDI organic matrix 2,5-dihydroxybenzoic acid (DHB, Sigma, St. Louis, MO) was dissolved in 50% ethanol to yield a 200mM solution. The individual lipid extract solutions were each mixed with the DHB MALDI matrix solution in a 1:10 ratio, and then manually spotted onto a 100 well stainless steel MALDI plate (Applied Biosystems, Foster City, CA). Sample spots were prepared *via* the vacuum dried droplet method, whereby the solution spots were flash evaporated under vacuum to promote uniform crystallization of sample and matrix.

3.2.2 IM-MS and MS analysis

Measurements were obtained on a custom built ion mobility-mass spectrometer (Ionwerks, Houston, TX) incorporating a MALDI ionization source (MALDI IM-MS).[29] In this instrument, MALDI ionization occurs at the pressure of the drift cell (helium at 3.8 Torr) utilizing a frequency tripled Nd-YLF (349nm) MALDI laser (Explorer, Newport / Spectra-Physics Corp., Mountain View, CA). The ionized species traverse a helium filled drift cell under the influence of a weak electric field where they are temporally dispersed based on their ion mobilities. Following the ion mobility (IM) separation, ions are guided by ion optics into the low pressure region of an orthogonal geometry time-of-flight (TOF) mass spectrometer. Arrival time data is measured for both the mobility and mass

dimensions and assembled into two dimensional spectra, while recording detector response (relative ion abundances) as a third dimension of information.[30] These multi-dimensional spectra were recorded for each individual lipid extract and were then analyzed and compared by using custom visualization software (Ionwerks, Houston, TX) developed on the IDL platform (ITT Visual Information Solutions, Boulder, CO).

The identities of intact lipid signals were confirmed with high-resolution MALDI – TOF MS (Voyager DE – STR, Applied Biosystems, Foster City, CA) and high-resolution MALDI – TOF/TOF MS (Ultraflex III, Bruker Daltonics, Billerica, MA) both operated in reflectron mode. A 337 nm N_2 laser operated at 20Hz was utilized for the MALDI-TOF MS analysis, while a Smartbeam frequency-tripled Nd:YLF (349nm) 200 Hz laser was used for MALDI-TOF/TOF MS analysis. Lipid identification was aided by information available from the website of Avanti Lipids Inc. (Birmingham, AL),[31] the LIPIDMAPS database,[15,16,17] and previously published identification of MALDI lipid spectra.[32] Laser ionized spherical fullerenes C_{60} (720 m/z) and C_{70} (840 m/z) were used as mass calibrants for the IM-MS. The cardiac peptide bradykinin has been extensively studied with ion mobility methods[33] and was used in this study as a collision cross-section standard for the calibration of the ion mobility drift time data.

3.2.3 Collision cross-section (CCS) determination.

The raw mobility time data recorded by the instrument is a composite of the time it takes the ions to traverse the drift cell, t_d, plus the time the ions spend in the ion optic interface, t_{int}. To determine the CCS of the measured lipid ions, t_{int}

must be calculated and subtracted from the total recorded mobility time in order to obtain the ion's drift time in the IM, t_d. Time correction plots were generated as follows: ion mobilities of each sample are recorded at a series of decreasing drift cell voltages. Under low field conditions of this experiment the mobility drift time is directly proportional to the inverse of voltage (1/V) due to the direct relationship between the drift velocity and electric field.[34] In a linear fit of the data projected as mobility drift time (x-axis) *vs.* 1/V (y-axis), the y-intercept determines t_{int}. The corrected ion mobility drift time, t_d, can thus be calculated by subtracting t_{int} from the mobility time recorded by the instrument.

The exact hard sphere scattering model is used to extract CCS values from ion transport data. In general, the accuracy of the hard sphere model improves as the size of the analyte with respect to the drift gas increases.[35] The low mass and polarizability of helium drift gas and the low electric field conditions of the ion mobility experiment lead to the predominant elastic hard sphere scattering contribution to measured drift time data. CCS values are calculated using the Mason-Schamp equation corrected for standard temperature and pressure (*i.e.*, reduced ion mobility)[36];

$$\Omega_D = \frac{\sqrt{18\pi}}{16} \cdot \frac{ze}{\sqrt{k_B \cdot T}} \cdot \sqrt{\frac{1}{m_{ion}} + \frac{1}{m_{He}}} \cdot \frac{t_d \cdot E}{L} \cdot \frac{760\,Torr}{P} \cdot \frac{T}{273.15\,K} \cdot \frac{1}{N_o}$$

here z is the charge of the ion, k_B is the Boltzmann constant, T is the temperature of the drift gas, t_d is the ion mobility drift time through the drift cell region, L is the

length of the drift region, E = V/L is the magnitude of the electric field, P is the

pressure of drift gas (He), and N_0 is the number density of helium gas at standard

temperature and pressure (T = 273.15 K, P = 760 Torr).

3.2.4 Computational modeling.

Computational starting structures of lipid headgroups and fatty acid tails

were built using the Molecular Operating Environment (MOE) package (Chemical

Computing Group, Montreal, Canada).[37] Quantum mechanical Hartree-Fock

(QM) geometry optimization and electrostatic potential calculations were

performed using Gaussian03[38] with a 6-31G* basis set. Partial charges for fatty

acids were derived by fitting the QM electrostatic potential to an atom-centered

point charge model using the RESP procedure.[39,40] Standard AMBER 99

parameters were used for bond, angle, dihedral, and van der Waals interactions.

Additional dihedral parameters needed for unsaturated fatty acid side chains

were taken from previous parameterization for arachidonic acid.[41,42] Molecular

dynamics (MD) simulations of lipid ions were performed with the SANDER

module of AMBER 10[43] using a high temperature conformational sampling

protocol. In this approach, each examined lipid ion was gradually heated to 1100

Kelvin and allowed to sample high-energy conformations at this temperature for

nine nanoseconds of simulation time. Utilizing a modified simulated annealing

approach, 30000 structures were extracted throughout this high temperature

trajectory, gradually cooled to 50 Kelvin, and subsequently energy minimized. I

used the MOBCAL[35] program to determine the projection approximation (PA)

collision cross-section of cooled lipid conformational snapshots obtained from the modified simulated annealing procedure. Low energy (*i.e.*, potential energy lower than the average energy of all simulated structures) MD snapshots whose collision cross-section matched experimental values were chosen for cluster analysis. Superposition and clustering programs partially developed at the Vanderbilt Center for Structural Biology[44] were used to sort structures into clusters based on conformational similarity (Figure 1.2). Selected atoms were included in the clustering analysis based on their expected contribution to the conformational arrangement of lipid ion atoms, including the metal cation, phosphate, carboxyl ester linkage (phospholipids), carboxyl ester and amide linkage (sphingolipids) and selected headroup atoms (*e.g.*, nitrogen of quaternary ammonium cation of choline in PtdCho and SM structures). Structures featuring the correct sodium coordination were then analyzed for equivalent intercarbon distances as outlined in Figures 3.3 and 3.5 using the ptraj structure analysis software of AMBER.

3.3 Results and Discussion

In eukaryotic organisms, the overwhelming majority of membrane lipids are comprised of glycerolipids, glycerophospholipids and sphingolipids. Example structures of the glycerophospholipid and sphingolipid animal lipid extracts investigated in this work are provided in Figure 3.1. Glycerophospholipids and sphingolipids are characterized by different backbones (*i.e.*, glycerol,

sphingosine) and appear to serve a diverse and in some cases distinctive structural and biochemical functions.[3,45,46,47] In these lipids, glycerol and sphingosine backbones can both esterify to phosphate and it is through this phosphate that the lipids functionalize to various polar headgroups (*e.g.*, ethanolamine, serine, choline, carbohydrates). In positive mode MS experiments, phosphatidylcholines (PtdChol, PC) and sphingomyelins (SM) with a choline headgroup cationize most efficiently from complex mixtures due to the positively charged quaternary ammonium ion of the choline headgroup. Across organisms, these two classes of lipids represent the most abundant membrane lipid species. Other lipid species, such as phosphatidylethanolamines (PtdEtn, PE) and phosphatidylserines (PtdSer, PS) also tend to form stable negative ions, and thus are also observable in negative ion mode MS.
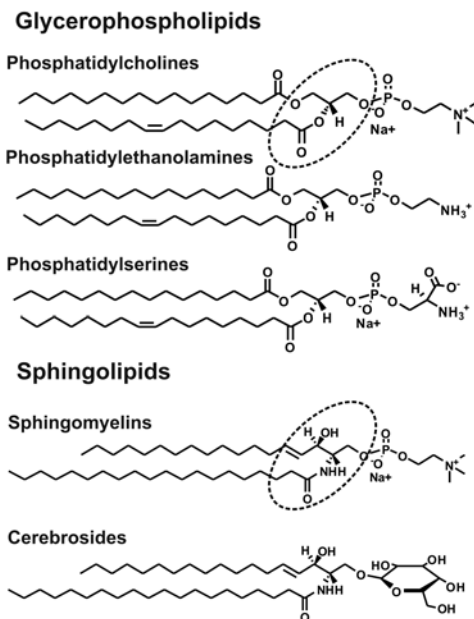
Figure 3.1 Representative structures for the lipids that constitute the animal extracts investigated for mobility separation properties. The circled areas denote the principal structural difference between glycerophospholipids and sphingolipids.

Previous IM-MS studies of lipids focused on the mobility drift time characterization of glycerophospholipids and the choline headgroup bearing sphingomyelin.[26,27,28] I extend these observations by noting an important trend in glycerophospholipid and sphingolipid IM separation. In addition to previously observed structural separation of glycerophospholipids based on headgroup and alkali metal coordination, I find that sphingolipids, on a more general level, tend to mobility separate from glycerophospholipids. This represents a practical finding that in the future may become applicable to the deconvolution of lipid signals from complex samples using the IM-MS analytical approach.[23]

Recently a review of MALDI/secondary ionization MS analysis of lipids underscored the need for a database of lipid ion collision cross-section (CCS) values.[48] The prototype MALDI IM-MS instrument utilized in this work incorporates a uniform electric field IM spectrometer operated under low field conditions, which allows first principles based determination of absolute gas-phase CCS of both positive and negative lipid ion species. Following the experimental MALDI IM-MS protocol of Woods and coworkers,[26] mobility drift time data was first acquired for signals from tested lipid standards. Then, mobility drift time measurements were transformed into absolute CCS values (in Å^2). We present here the first cross-section and reduced mobility lipid database of positive and negative lipid species (Table 3.1, Appendix Table A.1).

Table 3.1 Table of assigned phosphatidylcholine (PC) and sphingomyelin (SM) signals with their respective measured CCS and reduced mobility (K_o) values.

Lipid	Mass-to-Charge (m/z) Value		CCS	Reduced Mobility (K_o)
[M+X]$^+$ X=H or Na	Experimental	Theoretical	Å^2	cm^2·V^{-1}·sec^{-1}
SM (36:1) H$^+$	731.63	731.61	221.1 ± 1.9	2.430 ± 0.021
SM (36:1) Na$^+$	753.58	753.59	221.3 ± 2.6	2.427 ± 0.029
PC 34:2 H$^+$	758.59	758.57	217.4 ± 3.2	2.472 ± 0.037
SM (38:1) H$^+$	759.60	759.64	229.8 ± 3.4	2.337 ± 0.034
PC 34:1 H$^+$	760.59	760.59	219.1 ± 2.7	2.452 ± 0.030
PC 34:2 Na$^+$	780.58	780.55	218.9 ± 2.8	2.454 ± 0.032
SM (38:1) Na$^+$	781.63	781.62	231.3 ± 2.5	2.323 ± 0.025
PC 34:1 Na$^+$	782.57	782.57	221.7 ± 3.2	2.423 ± 0.034
PC 36:2 H$^+$	786.65	786.60	222.6 ± 2.2	2.413 ± 0.023
SM (40:1) H$^+$	787.65	787.67	232.2 ± 5.0	2.314 ± 0.050
PC 36:1 H$^+$	788.66	788.62	227.4 ± 4.3	2.362 ± 0.044
PC 36:2 Na$^+$	808.59	808.58	226.7 ± 4.6	2.370 ± 0.048
PC 36:1 Na$^+$	810.64	810.60	228.1 ± 2.0	2.354 ± 0.021
SM (42:2) H$^+$	813.73	813.68	241.8 ± 2.5	2.221 ± 0.023
SM (42:1) H$^+$	815.72	815.70	242.1 ± 6.3	2.219 ± 0.058
SM (42:2) Na$^+$	835.69	835.67	239.4 ± 2.8	2.243 ± 0.026
SM (42:1) Na$^+$	837.71	837.68	239.3 ± 4.7	2.245 ± 0.044
SM (44:1) Na$^+$	865.56	865.71	247.9 ± 4.3	2.167 ± 0.037
PC 42:1 Na$^+$	894.54	894.69	238.2 ± 2.3	2.254 ± 0.021

The nomenclature of PC X:Y, indicates that there are X carbons in the fatty acid chains and Y sites of unsaturation. In the nomenclature of SM X:Y, X indicates the number of carbons in the amide linked fatty acid plus eighteen carbons of the sphingosine backbone and Y the total number of double bonds in the entire lipid structure. Parentheses () distinguish sphingolipid from glycerophospholipid nomenclature in the table. Summary tables for positive and negative mode PtdSer (PS), PtdEtn (PE) and cerebroside (CB) signals are included in Appendix Table A.1.

Mobility drift time investigation and the subsequent CCS analysis of positive mode signals from two sphingolipid extracts and three glycerophospholipid extracts reveal that sphingolipid signals tend to adopt less compact gas-phase structures than glycerophospholipids, which allows for the mobility separation of these two lipids classes by IM-MS (Figure 3.2). Note that in Figure 3.2, the average peptide mobility-mass correlation trendline is also provided as a frame-of-reference[49].
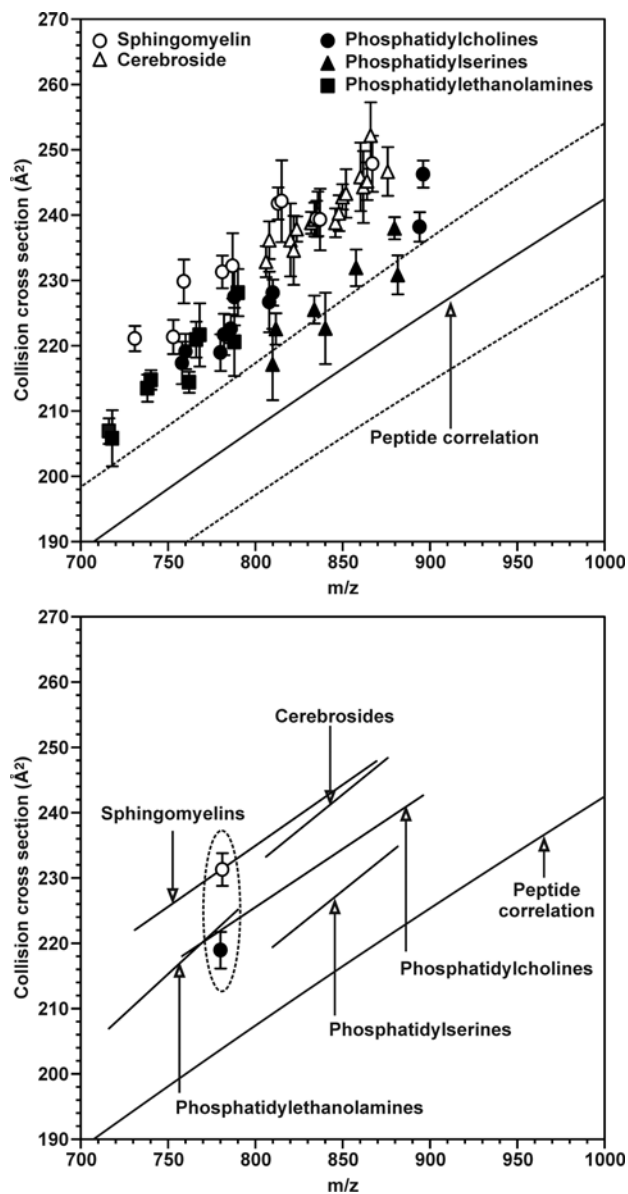
Figure 3.2 (top) A plot of collision cross-section versus m/z for sphingolipids (sphingomyelins, n = 10 and cerebrosides, n = 17) and glycerophospholipids (phosphatidylethanolamines, n = 9, phosphatidylserines, n = 7, and phosphatidylcholines, n = 10). Error bars represent ± 1σ for a minimum of 30 measurements. The average collision cross-section versus m/z for *ca.* 600 singly-charged peptides is indicated as a solid-line whereby ± 5% of the correlation is shown as dashed-lines. (bottom) Linear regressions plotted for each lipid class from the experimental data above. The specific species used in the modeling data presented in Figure 3.3 are circled.

The results also confirm previously observed mobility resolution of glycerophospholipids based on headgrooup differences (*i.e.*, phosphatidylserines from PtdCho and PtdEtn lipids), but also reveal that on a more general level, ion mobility separation can resolve glycerophospholipid and sphingolipid classes. The elucidation of the more subtle mobility differences within glycerophospholipid and sphingolipid classes will be reserved for future studies on IM-MS instruments with higher mobility resolution.

At the low electric field strengths utilized in the ion mobility experiments each IM-MS signal consists of populations of ions that are near thermal equilibrium with the room temperature drift gas as they travel through the drift region. These ion populations can be expected to consist of structurally similar ions that either undergo thermally accessible structural isomerization or depending on intramolecular forces and atomic rearrangement may even be expected to remain in relatively fixed conformations on the time scale of the IM-MS experiment.[50] One can think of the experimental collision cross-section as a size constraint that can be used to discriminate for and interpret a subset of structures from a large pool of computationally generated conformers.

In an effort to derive structural information from the IM measurements, selected PtdCho and SM experimental collision cross-section values were compared to lowest energy structures generated *in silico* and matched using theoretically generated CCS values in an approach pioneered by Jarrold[35,51] and Bowers.[33, 52] The computational modeling results appear to explain the main structural reasons for the observed ion mobility differences between the modeled

64

PtdCho and SM lipids, but also elucidate the relative lack of cationization (*i.e.*, small cation adduction) effect on the measured ion mobility of SM lipids previously observed by both Jackson *et al.* and Trimpin *et al.*
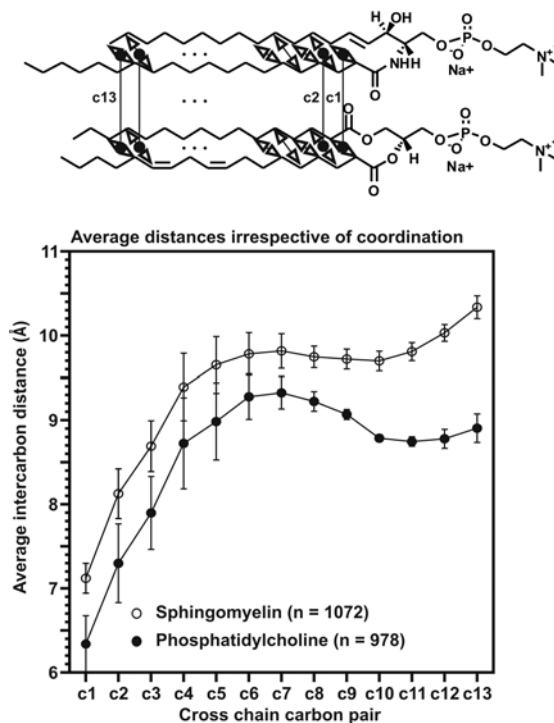
Figure 3.3 Average carbon pair distances d1 – d13 for SM and PtdCho irrespective of coordination. Equivalent carbon-carbon distances are significantly shorter in the PtdCho structures and thus PtdCho ions occupy a smaller volume in gas phase. Average carbon-carbon distances were determined from *ca.* 1000 structures whose theoretical CCS value matched the experimentally measured CCS.

In order to investigate the underlying reasons for the observed mobility separation of PtdCho and SM I chose to model two representative ions, which differ in mass by about a single mass unit, however their isotopic distributions effectively overlap with a mass difference of just 0.052 m/z; sodiated phosphatidylcholine PtdCho 34:2 (16:0 – 18:2) Na$^+$ at 780.552 m/z and sphingomyelin SM 38:1 (18:1d – 20:0) Na$^+$ at 781.604 m/z. Using the outlined

65

molecular dynamics protocol, I generated *ca.* 30,000 model structures for each selected ion, out of which approximately one thousand low energy structures matched the empirically derived collision cross-section to within 1% of the experimentally derived value. Based on initial MD simulations it appears reasonable to expect that the CCS of lipid species as they tumble through the helium drift gas depends primarily on the degree of acyl tail separation. In the MD simulations the fatty acids have a high propensity to wrap around the headgroup (*i.e.*, self solvate), which results in a roughly spherical compact ion. Thus, the acyl tail separation, if critical for the observed mobility separation of PtdCho and SM ions, should be distinctly different for each lipid type. An analysis of the tail distances (as outlined in Figure 3.3, top) of the modeled PtdCho and SM structures reveal that the mean acyl tail separation distances of the SM structures are indeed significantly larger than the mean acyl tail separation distances of the PtdCho structures (Figure 3.3, bottom). Tail separation thus appears to be a good descriptor of the gas-phase size of lipid ions.

After noting different coordination schemes of the sodium ion at the phosphate region of the modeled SM and PtdCho ions, conformational effects were further investigated by clustering analyses of the modeled structures based on conformational similarity. Superposition and clustering programs were used to compare MD generated structures based on the relative positions of selected backbone and headgroup atoms and the position of the sodium ion. Two primary coordination schemes existed (Figure 3.4); (i) a single coordination scheme in which the phosphate region of the lipid interacts with one feature of the tail region

(*i.e.*, one of the PtdCho carboxyls; the hydroxyl or amide group in SM) either *via*

sodium or hydrogen bonding, and (ii) a double coordination scheme in which the

phosphate region interacts with two features of the tail region (*i.e.*, both carboxyls

in PtdCho, both the hydroxyl and carbonyl group in SM).
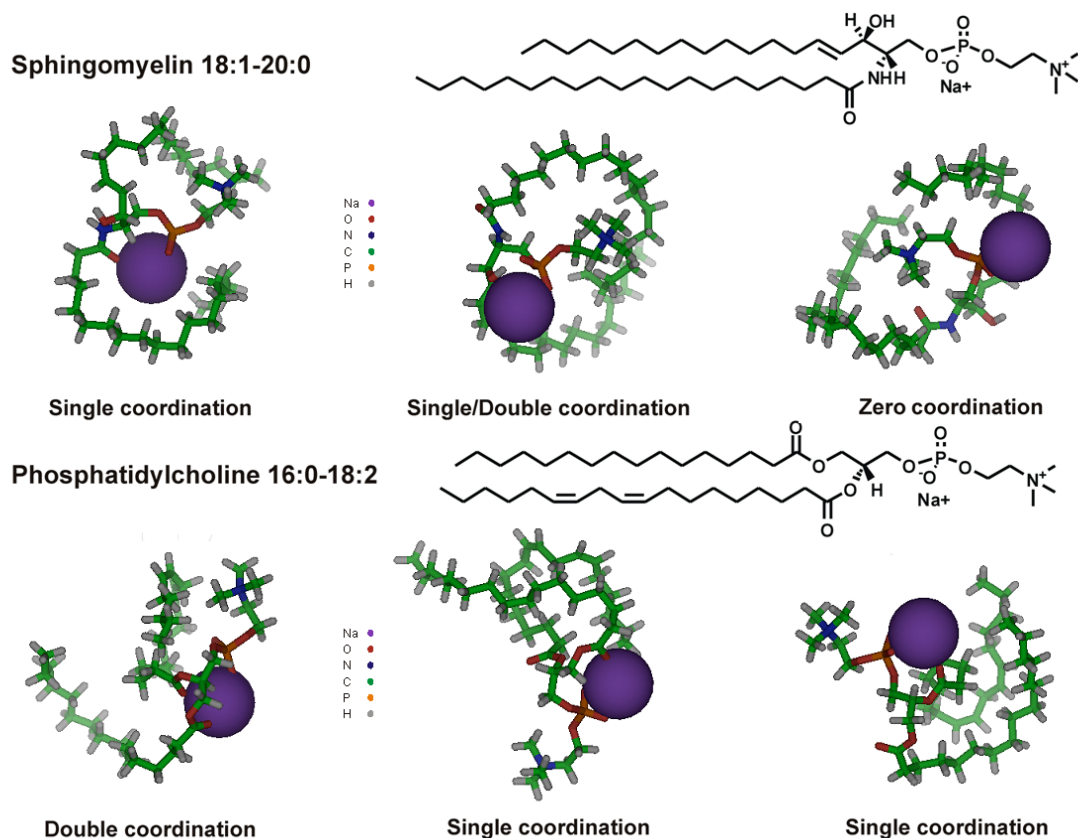
Figure 3.4 Examples of cation coordination: **(Top).** Representative structures of most populated MD clusters of SM 38:1 coordinated with Na$^+$ (*i.e.*, [M+Na]$^+$). The structures represent the predominant headgroup conformational arrangements of low energy structures whose computed CCS values match the experimentally measured CCS. **(Bottom).** Representative structures from the most populated MD clusters of PtdCho 34:2. Notable for both top and bottom representative structures are the oxophilic positioning of the sodium cation and its ability to act as a coordination bridge between the phosphate and other electron rich parts of the backbone. The coordination is termed single, double or zero, based on the number of non-phosphate atom centers coordinated to the sodium, and/or the tertiary amine of the choline headgroup.

I tested the hypothesis that the type of coordination leads to different tail separations within the SM and PtdCho structures and/or has different effects on the tail separation of their structures. The types of atomic interactions at the head group were found to play a significant role in tail separations of the modeled PtdCho lipid structures and a less significant role in tail separation differences of SM lipid structures (Figure 3.5). Based on the two plots presented in Figure 3.5, it appears that, while the type of coordination at the headgroup – tail interface leads to significant differences in tail separation of PtdCho structures.
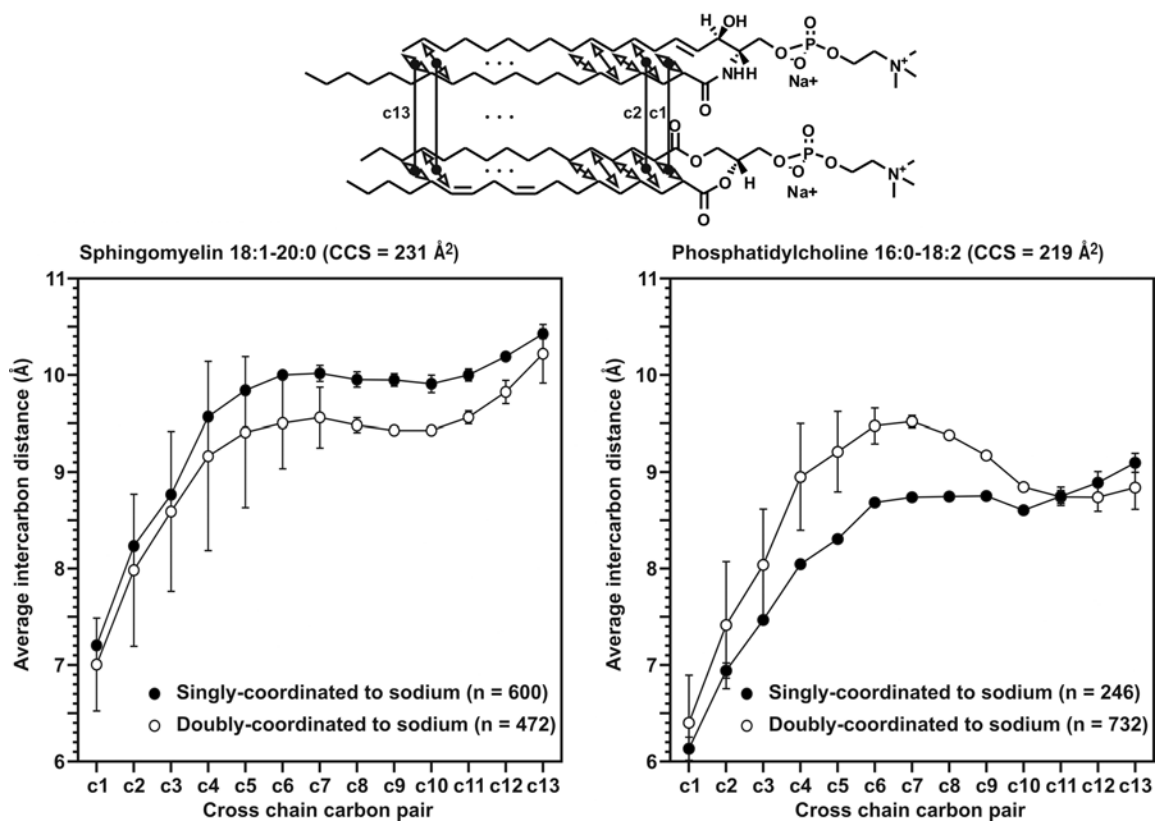
Figure 3.5 Clustering analysis of effect of coordination on average tail distances for SM (left) and PtdCho (right) lipids. A comparison of the two plots reveals that the average distances (*ca.* 1000 modeled structures) of equivalent carbons of PtdCho 34:2 and SM 38:1 are indeed larger in the SM lipid. Surprisingly, the distance remains larger even for carbons remote to the headgroup region and carbon-carbon distances are highly dependent on whether the prevailing sodium coordination is single or double.

The SM structures seem to be less responsive to the type of coordination at the headgroup-tail interface region. That is, on average, the sphingomyelin tail distances do not seem to strongly respond to single or double coordination to sodium cation, whereas the equivalent tail distances of phosphatidylcholine structures depend strongly on the type of cation coordination.

This apparent unresponsiveness of the sphingomyelin structures to the type of headgroup coordination of the sodium ion can be rationalized as follows: the reduced rotational degrees of freedom introduced by the presence of the trans-double bond and the amide bond in the sphingosine backbone most likely dominate the dynamics of SM, CB tail separation. Therefore, it appears that the experimentally observed gas-phase separation of sphingolipids from glycerophospholipids is most likely due to the relative rigidity of sphingosine backbone *vs.* the glycerophospholipids' relatively greater rotational flexibility of the glycerol backbone which allows it to more effectively self-solvate and form more compact, globular structures.

3.4 Conclusions

Ion mobility is a rapid gas-phase separation approach for the resolution of glycerophospholipids and sphingolipids based on structural differences of the glycerol and sphingosine backbones. In addition, the correlation of empirically-derived CCS with molecular dynamics simulations is used to better characterize where and why particular lipid signals occur in mobility separation space.

Whereas IM-MS experimental measurements are best suited to answer binary structural hypotheses (*e.g.*, is an ion in gas-phase predominantly compact or extended), here I combine IM-MS results with modern computer modeling approaches *via* empirical CCS analysis to elucidate 3D atomic level structural signatures of PtdCho and SM lipids. Additional experimental and modeling work will elucidate known and likely reveal new valuable resolution trends within the glycerophospholipid and sphingolipid classes.

3.5 Acknowledgements

REFERENCES

[1] Wenk, M. R., The emerging field of lipidomics. *Nature Reviews Drug Discovery* **2005,** *4* (7), 594-610.

[2] Watson, A. D., Lipidomics: a global approach to lipid analysis in biological systems. *Journal of Lipid Research* **2006,** *47* (10), 2101-2111.

[3] Brown, H. A.; Murphy, R. C., Working towards an exegesis for lipids in biology. *Nature Chemical Biology* **2009,** *5* (9), 602-606.

[4] Farias, R. N.; Bloj, B.; Morero, R. D.; Sineriz, F.; Trucco, R. E., Regulation of Allosteric Membrane-Bound Enzymes through Changes in Membrane Lipid-Composition. *Biochimica Et Biophysica Acta* **1975,** *415* (2), 231-251.

[5] Cullis, P. R.; Dekruijff, B., Lipid Polymorphism and the Functional Roles of Lipids in Biological-Membranes. *Biochimica Et Biophysica Acta* **1979,** *559* (4), 399-420.

[6] Spector, A. A.; Yorek, M. A., Membrane Lipid-Composition and Cellular Function. *Journal of Lipid Research* **1985,** *26* (9), 1015-1035.

[7] Dowhan, W., Molecular basis for membrane phospholipid diversity: Why are there so many lipids? *Annual Review of Biochemistry* **1997,** *66*, 199-232.

[8] Han, X. L.; Gross, R. W., Shotgun lipidomics: Electrospray ionization mass spectrometric analysis and quantitation of cellular lipidomes directly from crude extracts of biological samples. *Mass Spectrometry Reviews* **2005,** *24* (3), 367-412.

[9] Song, H. W.; Ladenson, J.; Turk, J., Algorithms for automatic processing of data from mass spectrometric analyses of lipids. *Journal of Chromatography B-Analytical Technologies in the Biomedical and Life Sciences* **2009,** *877* (26), 2847-2854.

[10] Shevchenko, A.; Simons, K., Lipidomics: coming to grips with lipid diversity. *Nature Reviews Molecular Cell Biology* **2010,** *11* (8), 593-598.

[11] Yetukuri, L.; Ekroos, K.; Vidal-Puig, A.; Oresic, M., Informatics and computational strategies for the study of lipids. *Molecular BioSystems* **2008,** *4* (2), 121-127.

[12] Merrill, A. H.; Sullards, M. C.; Allegood, J. C.; Kelly, S.; Wang, E., Sphingolipidomics: High-throughput, structure-specific, and quantitative analysis of sphingolipids by liquid chromatography tandem mass spectrometry. *Methods* **2005,** *36* (2), 207-224.

[13] Liebisch, G.; Lieser, B.; Rathenberg, J.; Drobnik, W.; Schmitz, G., High-throughput quantification of phosphatidylcholine and sphingomyelin by electrospray ionization tandem mass spectrometry coupled with isotope correction algorithm. *Biochimica Et Biophysica Acta-Molecular and Cell Biology of Lipids* **2004,** *1686* (1-2), 108-117.

[14] Han, X. L.; Gross, R. W., Shotgun lipidomics: multidimensional MS analysis of cellular lipidomes. *Expert Review of Proteomics* **2005,** *2* (2), 253-264.

[15] Fahy, E.; Subramaniam, S.; Murphy, R. C.; Nishijima, M.; Raetz, C. R. H.; Shimizu, T.; Spener, F.; van Meer, G.; Wakelam, M. J. O.; Dennis, E. A., Update of the LIPID MAPS comprehensive classification system for lipids. *Journal of Lipid Research* **2009,** *50*, S9-S14.

[16] Sud, M.; Fahy, E.; Cotter, D.; Brown, A.; Dennis, E. A.; Glass, C. K.; Merrill, A. H.; Murphy, R. C.; Raetz, C. R. H.; Russell, D. W.; Subramaniam, S., LMSD: LIPID MAPS structure database. *Nucleic Acids Research* **2007,** *35*, D527-D532.

[17] Fahy, E.; Sud, M.; Cotter, D.; Subramaniam, S., LIPID MAPS online tools for lipid research. *Nucleic Acids Research* **2007,** *35*, W606-W612.

[18] Niemela, P. S.; Castillo, S.; Sysi-Aho, M.; Oresic, M., Bioinformatics and computational methods for lipidomics. *Journal of Chromatography B-Analytical Technologies in the Biomedical and Life Sciences* **2009,** *877* (26), 2855-2862.

[19] Fahy, E.; Cotter, D.; Byrnes, R.; Sud, M.; Maer, A.; Li, J.; Nadeau, D.; Zhau, Y.; Subramanian, S., Bioinformatics for lipidomics. *Lipidomics and Bioactive Lipids: Mass-Spectrometry-Based Lipid Analysis* **2007,** *432*, 247-273.

[20] Ivanova, P. T.; Milne, S. B.; Myers, D. S.; Brown, H. A., Lipidomics: a mass spectrometry based systems level analysis of cellular lipids. *Current Opinion in Chemical Biology* **2009,** *13* (5-6), 526-531.

[21] Petkovic, M.; Schiller, J.; Muller, M.; Benard, S.; Reichl, S.; Arnold, K.; Arnhold, J., Detection of individual phospholipids in lipid mixtures by matrix-assisted laser desorption/ionization time-of-flight mass spectrometry: Phosphatidylcholine prevents the detection of further species. *Analytical Biochemistry* **2001,** *289* (2), 202-216.

[22] Lou, X. W.; van Dongen, J. L. J.; Vekemans, J.; Meijer, E. W., Matrix suppression and analyte suppression effects of quaternary ammonium salts in matrix-assisted laser desorption/ionization time-of-flight mass spectrometry: an investigation of suppression mechanism. *Rapid Communications in Mass Spectrometry* **2009,** *23* (19), 3077-3082.

[23] Ridenour, W. B.; Kliman, M.; McLean, J. A.; Caprioli, R. M., Structural Characterization of Phospholipids and Peptides Directly from Tissue Sections by MALDI Traveling-Wave Ion Mobility-Mass Spectrometry. *Analytical Chemistry* **2010,** *82* (5), 1881-1889.

[24] Shvartsburg, A. A.; Smith, R. D., Fundamentals of Traveling Wave Ion Mobility Spectrometry. *Analytical Chemistry* **2008,** *80* (24), 9689-9699.

[25] Wallace, A.; Millar, A.; Langridge, J., New structural insights from high-efficiency ion mobility and tandem mass spectrometry. *Nature Methods* **2007**, AN12-AN13.

[26] Jackson, S. N.; Ugarov, M.; Post, J. D.; Egan, T.; Langlais, D.; Schultz, J. A.; Woods, A. S., A Study of Phospholipids by Ion Mobility TOFMS. *Journal of the American Society for Mass Spectrometry* **2008,** *19* (11), 1655-1662.

[27] Trimpin, S.; Tan, B.; Bohrer, B. C.; O'Dell, D. K.; Merenbloom, S. I.; Pazos, M. X.; Clemmer, D. E.; Walker, J. M., Profiling of phospholipids and related lipid structures using multidimensional ion mobility spectrometry-mass spectrometry. *International Journal of Mass Spectrometry* **2009,** *287* (1-3), 58-69.

[28] Kim, H. I.; Kim, H.; Pang, E. S.; Ryu, E. K.; Beegle, L. W.; Loo, J. A.; Goddard, W. A.; Kanik, I., Structural Characterization of Unsaturated Phosphatidylcholines Using Traveling Wave Ion Mobility Spectrometry. *Analytical Chemistry* **2009,** *81* (20), 8289-8297.

[29] Sundarapandian, S.; May, J. C.; McLean, J. A., Dual Source Ion Mobility-Mass Spectrometer for Direct Comparison of Electrospray Ionization and MALDI Collision Cross Section Measurements. *Analytical Chemistry* **2010,** *82* (8), 3247-3254.

[30] Hoaglund, C. S.; Valentine, S. J.; Sporleder, C. R.; Reilly, J. P.; Clemmer, D. E., Three-dimensional ion mobility TOFMS analysis of electrosprayed biomolecules. *Analytical Chemistry* **1998,** *70* (11), 2236-2242.

[31] Avanti Polar Lipids http://www.avantilipids.com/ (accessed 2007, 2008).

[32] Jackson, S. N.; Wang, H. Y. J.; Woods, A. S., In situ structural characterization of glycerophospholipids and sulfatides in brain tissue using MALDI-MS/MS. *Journal of the American Society for Mass Spectrometry* **2007,** *18* (1), 17-26.

[33] Wyttenbach, T.; vonHelden, G.; Bowers, M. T., Gas-phase conformation of biological molecules: Bradykinin. *Journal of the American Chemical Society* **1996,** *118* (35), 8355-8364.

[34] Revercomb, H. E.; Mason, E. A., Theory of Plasma Chromatography Gaseous Electrophoresis - Review. *Analytical Chemistry* **1975,** *47* (7), 970-983.

[35] Shvartsburg, A. A.; Jarrold, M. F., An exact hard-spheres scattering model for the mobilities of polyatomic ions. *Chemical Physics Letters* **1996,** *261* (1-2), 86-91.

[36] Mason, E. A.; McDaniel, E. W., Measurement of Drift Velocities and Longitudinal Diffusion Coefficients. In *Transport Properties of Ions in Gases*, John Wiley & Sons: New York, 1988; pp 31-102.

[37] *Molecular Operating Environment*, version 2006.08; Chemical Computing Group, Inc.: Montreal, Quebec, Canada; (accessed 2008, 2009).

[38] *Gaussian 03*, version 2003.D.01; Gaussian, Inc.: Wallingford, CT; (accessed 2008, 2009).

[39] Bayly, C. I.; Cieplak, P.; Cornell, W. D.; Kollman, P. A., A Well-behaved Electrostatic Potential Based Method Using Charge Restraints for Deriving Atomic Charges – The RESP Model. *Journal of Physical Chemistry* **1993,** *97* (40), 10269-10280.

[40] Case, D. A.; Cheatham, T. E.; Darden, T.; Gohlke, H.; Luo, R.; Merz, K. M.; Onufriev, A.; Simmerling, C.; Wang, B.; Woods, R. J., The Amber biomolecular simulation programs. *Journal of Computational Chemistry* **2005,** *26* (16), 1668-1688.

[41] Furse, K. E.; Pratt, D. A.; Porter, N. A.; Lybrand, T. P., Molecular dynamics simulations of arachidonic acid complexes with COX-1 andCOX-2: Insights into equilibrium behavior. *Biochemistry* **2006,** *45* (10), 3189-3205.

[42] Furse, K. E.; Pratt, D. A.; Schneider, C.; Brash, A. R.; Porter, N. A.; Lybrand, T. P., Molecular dynamics simulations of arachidonic acid-derived pentadienyl radical intermediate complexes with COX-1 and COX-2: Insights into oxygenation regio- and stereoselectivity. *Biochemistry* **2006,** *45* (10), 3206-3218.

[43] *AMBER Molecular Modeling Package*, version 10; University of California: San Francisco; (accessed 2008, 2009).

[44] *Suppose – superposition software*, version 2006; Vanderbilt University: Nashville, TN; (accessed 2008, 2009).; *OC - A cluster analysis program*, version 2002; University of Dundee, Scotland, UK; (accessed 2008, 2009).

[45] van Meer, G.; Voelker, D. R.; Feigenson, G. W., Membrane lipids: where they are and how they behave. *Nature Reviews Molecular Cell Biology* **2008,** *9* (2), 112-124.

[46] Phillips, R.; Ursell, T.; Wiggins, P.; Sens, P., Emerging roles for lipids in shaping membrane-protein function. *Nature* **2009,** *459* (7245), 379-385.

[47] Merrill, A. H.; Stokes, T. H.; Momin, A.; Park, H.; Portz, B. J.; Kelly, S.; Wang, E.; Sullards, M. C.; Wang, M. D., Sphingolipidomics: a valuable tool for understanding the roles of sphingolipids in biology and disease. *Journal of Lipid Research* **2009,** *50*, S97-S102.

[48] Benabdellah, F.; Seyer, A.; Quinton, L.; Touboul, D.; Brunelle, A.; Laprevote, O., Mass spectrometry imaging of rat brain sections: nanomolar sensitivity with MALDI versus nanometer resolution by TOF-SIMS. *Analytical and Bioanalytical Chemistry* **2010,** *396* (1), 151-162.

[49] Tao, L.; McLean, J. R.; McLean, J. A.; Russell, D. H., A collision cross-section database of singly-charged peptide ions. *Journal of the American Society for Mass Spectrometry* **2007,** *18* (7), 1232-1238.

[50] Koeniger, S. L.; Merenbloom, S. I.; Clemmer, D. E., Evidence for many resolvable structures within conformation types of electrosprayed ubiquitin ions. *Journal of Physical Chemistry B* **2006,** *110* (13), 7017-7021.

[51] Clemmer, D. E.; Jarrold, M. F., Ion mobility measurements and their applications to clusters and biomolecules. *Journal of Mass Spectrometry* **1997,** *32* (6), 577-592.

[52] Wyttenbach, T.; vonHelden, G.; Batka, J. J.; Carlat, D.; Bowers, M. T., Effect of the long-range potential on ion mobility measurements. *Journal of the American Society for Mass Spectrometry* **1997,** *8* (3), 275-282.

Structural Mass Spectrometry Analysis of Lipid Changes in a

***Drosophila* Epilepsy Model Brain**

4.1 Introduction

Phosphatidylethanolamine (PtdEtn) is a highly abundant phospholipid in many species ranging from yeast to mammals. The second most abundant phospholipid after phophatidylcholine (PtdCho) in mammals, PtdEtn constitutes 15-25% of the total phospholipid content and is required in a diverse array of cellular functions.[1] In the *Drosophila* genetic model, PtdEtn lipid content is greater than 50%, making it the key component of phospholipid-dependent biology.[2] Due to cholesterol auxotrophy in *Drosophila*, lipid homeostasis is regulated by PtdEtn, rather than sterols, via the sterol element binding protein pathway.[3,4] Thus, PtdEtn synthesis and metabolism is central to *Drosophila* lipid biology.

The first step in PtdEtn biosynthesis in the CDP-ethanolamine pathway requires ethanolamine kinase. *Drosophila* possesses only a single ethanolamine kinase encoded by the *easily shocked* (*eas*) locus.[5] Adult *eas* mutant animals were previously isolated in a classic behavioral genetic screen for bang-sensitive paralysis.[6] Adult *eas* mutants are homozygous viable but display brief hyperactivity followed by complete paralysis when given a mechanical shock

such as banging on a bench top or short (10 second) vortex shaking.[7] The seizure-induced paralysis is transitory and is repeatedly manifest upon mechanical shock. In wildtype, PtdEtn is a major constituent of neuronal membranes. This *eas* mutant epileptic behavior results from defects in membrane neuronal excitability causing a burst of unregulated action potentials followed by neuronal transmission failure upon stimulation.[8-10] Compensatory mutations that decrease neuronal excitability eliminate the *eas* mutant defect.[11]

Previous studies have examined the link between the *eas* epileptic phenotype and the biochemistry of phospholipid metabolism by assaying whole head lipid levels using lipid extraction and thin layer chromatography (TLC) followed by colorimetric or fluorimetric reagent-based detection.[12] As expected, these studies showed an overall decrease in PtdEtn in *eas* mutants. However, these techniques did not reveal the specific lipid species present, nor could they distinguish a heterogeneous response within a specific lipid class in which the biosynthesis of particular lipid species is up or down regulated. Recent advances in mass spectrometry (MS) instrumentation coupled with the development of lipid databases (*e.g.*, LipidMaps, SphinGOMAP) have allowed rapid identification of lipids on the basis of highly accurate mass measurements and targeted fragmentation experiments. For example, isotopic pattern matching in tandem with controlled fragmentation can often yield unambiguous identification of lipid class and composition (*e.g.*, identification of sn-1 and sn-2 fatty acids in glycerophospholipids).[13-15]

In the present study, we have developed a rapid structural MS methodology using matrix assisted laser desorption ionization (MALDI) combined with ion mobility-MS (IM-MS) for the relative quantitation of intact phospholipid signals directly from isolated brain tissue. Importantly, IM-MS provides a rapid (<ms) 2D separation of species on the basis of structure, or apparent surface area, and mass-to-charge (*m/z*) in the IM and MS dimensions, respectively. At a particular *m/z* specific signals can be confidently assigned to being lipid species on the basis of their ion mobility drift time, or apparent surface area, in spite of a background of exogenous or endogenous chemical noise (*e.g.*, protein degradation products, peptides, carbohydrates, metabolites, etc.).[16,17,18] Unlike previous methods of overall *Drosophila* lipid class abundance comparisons,[5,12] the strategies we have developed provide a detailed molecular assay of specific lipid structures that show changes in abundance in the mutant brain. These methods can be generalized to any *Drosophila* tissue that can be selectively dissected, (*e.g.*, optical lobes, ring gland, garland cells). This approach paints a much more detailed picture of the entire lipid profile within the brain proper, with dramatically improved sensitivity, as well as decreased processing time for evaluating changes across PtdEtn, PtdIns, and PtdCho lipid species in the brains of *eas*[2] mutants relative to matched wildtype controls.

4.2 Experimental

4.2.1 *Drosophila* stocks

Control and mutant stocks were reared and maintained at $25^{\circ}C$ on standard agar/yeast/ molasses/cornmeal food. Canton S (CS) was used as the wildtype control. The eas^2 allele, kindly provided by Barry Ganetzky, University of Wisconsin, Madison, WI, is an amorphic allele with no detectable ethanolamine kinase (EK) activity.[12, 32]

4.2.2 MALDI preparation

Adult female animals (3-5 day old) were anesthetized with CO_2 and then immediately decapitated with forceps in phosphate buffered saline (PBS). Whole intact brains were dissected free with the optic lobes removed. The central brain in PBS was pipetted onto a MALDI plate prechilled on dry ice and then dried in the desiccator for 15 min. Lipid MALDI matrix 2,5-Dihydroxyacetophenone (DHA, Aldrich Chemicals) was selected from five MALDI matrices (2,5– Dihydroxybenzoic acid (DHB), Trihydroxyacetophenone (THAP), 2-Mercaptobenzothiazole (MBT), p-Nitroaniline (PNA)) on the basis of providing maximum lipid signal intensity. DHA crystals were first crushed through ball milling to submicrometer size. The nanoparticle crystals were carefully applied on top of desiccated brain tissues with a small paintbrush. The plate with DHA covered tissues was inserted into the ion source of a Synapt HD IM-MS instrument (Waters, Corp). One experimental dataset consisted of 3 wildtype

control and 3 *eas*[2] mutant brains. Three experimental datasets were generated in both positive and negative ionization modes on three different days, representing a total of 9 control and 9 mutant brains.

4.2.3 Ion mobility-mass spectrometry

Signals were generated using an Nd:YAG 355nm laser at an energy setting of 25 for 3 mins, rastering the entire area of the matrix covered tissue. IM was performed using traveling wave separation through nitrogen gas.[33] The ion guide T-wave was operated at 300 m/s and linearly ramped in amplitude from 5-20 V over each experiment. The Transfer guide T-wave was operated at 248 m/s with a constant 3 V amplitude. Ion injection voltages in the trap and transfer regions were set at 4 and 6 V, respectively. The TOF mass analyzer was calibrated in both ionization modes using a mixture of fullerenes C60 and C70 (Acros Organics) and typically provided *ca.* 10,000 resolution for both parent ion and fragmentation spectra. Both negative and positive mode experiments consisted of recording lipid signals from 9 wildtype control and 9 *eas*[2] mutant brains. Each extracted lipid profile consisted of a list of specific *m/z* signals with absolute number of measured counts. The number of counts for each *m/z* signal was normalized to the total number of lipid counts in the *m/z* range of 700 to 900. Normalization was used to correct for sample-to-sample variation due to differences in laser rastering accuracy (*i.e.*, laser residence time on tissue) and for the variation due to sample microdissection heterogeneity. Significantly changing lipid signals in both positive and negative modes were fragmented in

the transfer region of the Synapt HD MS using a collision energy (CE) setting of 50. The LM parameter, which controls the range of masses used for parent ion selection, of the mass selection quadrupole was adjusted from 4 to 16 to provide a 3 Da window, the narrowest available, for parent mass selection before fragmentation. The fragmentation data was used to validate the parent mass identity. All MS/MS spectra and annotation of the peaks used for lipid identification are provided in the electronic supplementary materials. MassLynx software (Waters Corp., Manchester, UK) was used for both instrument control and data analysis.

4.2.4 Peak alignment and statistical analysis

MS peak alignment was performed using a custom swift peak alignment (SPA) Visual Basic Excel (Microsoft) macro. SPA uses the longest sample *m/z* column (*i.e.*, containing the highest number of *m/z* signals) to search for closest *m/z* matches in the other data columns. Closeness is defined by the absolute value of the difference of two compared cells. SPA flags any differences greater than a user specified *m/z* threshold. Custom mass difference thresholds can be chosen based on the expected mass measurement accuracy of the instrument. Here, due to expected peak overlaps of nearly isobaric species that can lead to peak broadening we chose a single mass difference threshold value of 0.20 Da.

Statistical analysis was conducted using SAS (version 9.1.3, SAS institute, Cary, NC) Procedure GLIMMIX. To identify lipids differentially

expressed between wildtype control and mutant groups, we used the following Poisson Linear Mixed Model:

Let Y_{ijk} = spectral count for sample j from group i on day k;

We assume $Y_{ijk} \sim Poisson(\phi\mu_{ijk})$ for each lipid, to fit the following model:

$$Log\left(\frac{\mu_{ijk}}{N_{ijk}}\right) = \alpha + \beta \; \text{Group}_i + Day_k$$

where μ_{ijk} = the mean of assumed Poisson distribution above; N_{ijk} = total spectral count from all lipids for sample j from group i on day k; Group = 1 if the sample is from mutant group, 0 otherwise; β = parameter for fixed group effect that describes group differences, statistical significance of the null hypothesis Ho: $\beta = 0$ would indicate the average proportion (count for the particular lipid /total count) is significantly different for the two groups;

$Day_1, .., Day_{n\_days} \sim N(0, \sigma_d^2)$ are random effects that model effects due to days.

In addition, the model $Y_{ijk} \sim Poisson(\phi\mu_{ijk})$ includes an overdispersion parameter ϕ, which accounts for greater variability in the dataset than those accounted by assuming the Poisson model. Because both fixed and random effects are included, this model is a mixed effects model. We used the Kenward-Roger's adjusted degrees of freedom solution (option DDFM=KR in Proc GLIMMIX) for statistical inference,[34] an approach specifically proposed for small sample settings. Because many lipids were examined, to account for false positives caused by multiple comparisons, given the nominal p-values, we also

estimated False Discovery Rate (FDR) using the method of Benjamini and Hochberg.[35] The experimental p-values obtained using the poisson model were successfully tested for p-value stability. To quantify the stability of the p-values due to sampling variations, we took sub-samples from the 18 original samples and estimated the standard deviation of the p-values for each lipid. More specifically, the Poisson model described above was repeated 18 times, each time leaving out one sample in turn. Then, we have 18 sets of p-values, one for each repetition. In Appendix B, Table B.1, for each negative mode lipid signal change with p<0.1, we show the standard deviation based on the 18 p-values.

4.2.5 Lipid signal assignment

Negative mode assignments were based on intact lipid mass, fatty acid, headgroup and neutral loss fragment assignments based on previously published PtdEtn and PtdIns lipid fragmentation studies.[36,37] Positive mode assignments were based on intact lipid mass, PtdCho and PtdEtn signature peaks 147 (PtdCho), 163 (PtdCho), 184 (PtdCho), 121 (PtdEtn), 146.0 (PtdEtn), 164 (PtdEtn).[38,39,40] The LipidMaps database (Nature Lipidomics Gateway) in tandem with previously published lipid fragmentation studies were used in lipid identity assignment on the basis of obtained fragmentation spectra and accurate parent masses. Results were tabulated and graphed using Excel. Fragmentation spectra and peak assignments for all significantly changing lipid species are annotated and provided in the Supporting Materials of reference 41, M. Kliman, N. Vijayakrishnan, L. Wang, J.T. Tapp, K. Broadie, J.A. McLean, *Molecular*

BioSystems **2010**, 6, 958-966. – Reproduced here by permission of The Royal Society of Chemistry (RSC). Fragment mass assignments are also provided in tables B.2, B.3, B.4, and B5 of the Appendix B section.

4.3 Results

The adult brain proper was acutely dissected and optic lobes removed from wildtype control (Canton-S; CS) and *easily shocked* null (eas^2) mutants lacking ethanolamine kinase activity. Brain tissue microsectioning, MALDI matrix selection and tissue application were first optimized for maximum lipid MS signal response (Figure 4.1 A). To maximize signal intensities, we used MALDI ionization via a nanocrystalline organic matrix (2,5-dihydroxyacetophenone, DHA), a modification of previously described microcrystaline dry matrix deposition.[19] Isolated central brains were deposited onto a MALDI plate, microsectioned, and painted with nanocrystalline DHA matrix. One experimental data set consisted of three wild type control and three mutant brain tissues (three control and mutant replicates). Using both positive and negative ionization modes, three experimental datasets (recorded on three different days) were generated.

The IM-MS was used to rapidly separate the relatively large lipid ions from smaller concomitant ions (*e.g.*, MALDI matrix signals) based on size, followed by *m/z*. (Figure 4.1 B). Data was acquired using signal integration, *i.e.*, accumulation of all lipid signals throughout the course of the experiment, rather than signal

averaging. Lipid peak lists consisting of *m/z* values with corresponding intensities were extracted from 2D spectra and aligned using an in-house developed swift peak alignment (SPA) program for subsequent statistical analysis. The general structure of significantly changing glycerophospholipids reported in this work is given in Figure 4.1 C. Different fatty acids and polar headgroups give rise to the various PtdEtn, PtdIns, and PtdCho lipid species.

Representative 2D data obtained from wt control and mutant brains are illustrated in Figure 4.2 A for both negative and positive ionization modes. Over 200 lipid signals in negative ionization mode and over 1000 lipid signals in positive ionization mode were detected. Statistical analysis yielded 49 negative mode signals and 194 positive mode signals that changed significantly between the wild type control and *eas^2* mutant conditions. An expanded view for the highlighted region on the corresponding 2D spectrum (Figure 4.2 A) of typical extracted raw MS data from negative and positive mode operation is illustrated in Figure 4.2 B. The isotopic envelopes of the lipid signals tend to cluster and within clusters, the monoisotopic (exact mass) lipid peaks are separated by two mass units, each 2 Da separation corresponding to a single double bond difference. This distribution is the result of the natural occurrence of various degrees of unsaturation within the fatty acids comprising the lipid species. In negative (left) and positive (right) ionization modes, the comparison of *eas^2* mutant and control MS spectra visually illustrates the lipid intensity differences later identified as significant changes (p<0.03) by statistical analysis.
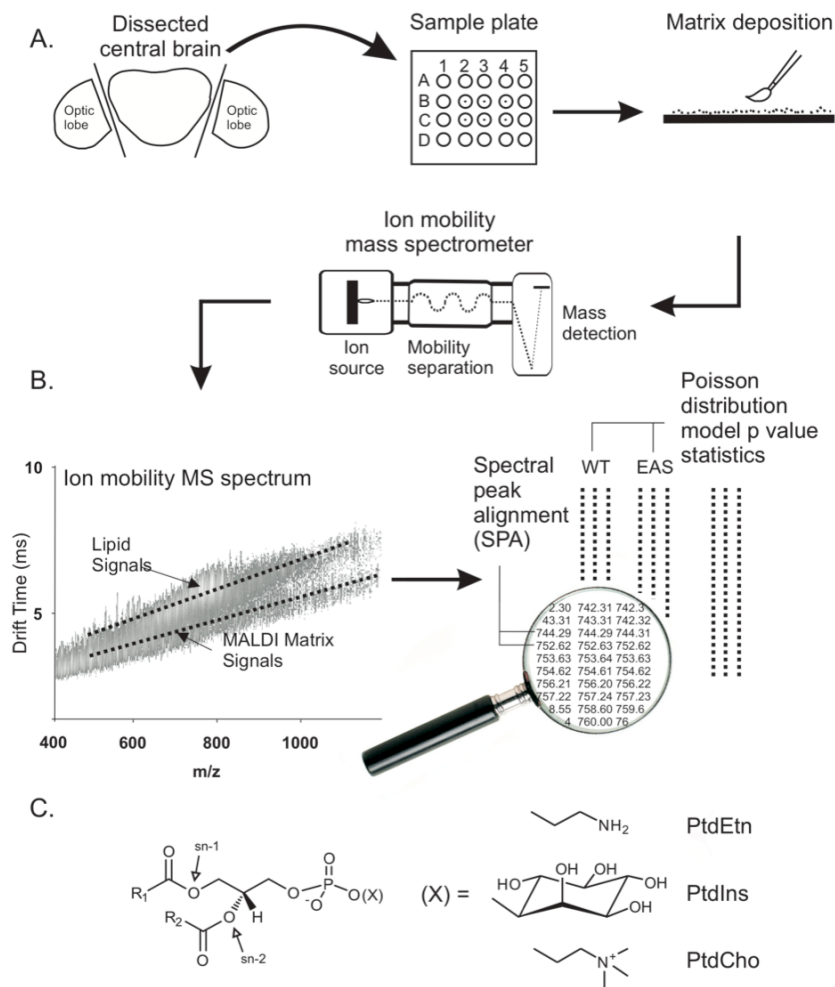
Figure 4.1 A schematic diagram of the workflow for MALDI-IM-MS analysis of phospholipids in the microdissected *Drosophila* brain. (A) The *Drosophila* central brain was spotted on a frozen MALDI plate and microsectioned. Finely crushed nanometer crystal size DHA MALDI matrix was deposited on the brain using a paint brush. Lipid signals were subsequently measured by MALDI-IM-MS. (B) Lipid MS data was extracted and aligned across three experimental sets using SPA peak alignment macro. Significance of lipid changes between control and mutant conditions were determined using Poisson model statistics. (C) The structures of significantly changing glycerophospholipids, where R_1 and R_2 are alkyl groups of fatty acids bound to the sn-1 and sn-2 hydroxyls of a glycerol phosphate and (X) are the structures of polar headgroups esterified to the phosphate that give rise to PtdEtn, PtdIns, and PtdCho lipid species. M. Kliman, N. Vijayakrishnan, L. Wang, J.T. Tapp, K. Broadie, J.A. McLean, *Molecular BioSystems* **2010**, 6, 958-966. - Reproduced by permission of The Royal Society of Chemistry (RSC).
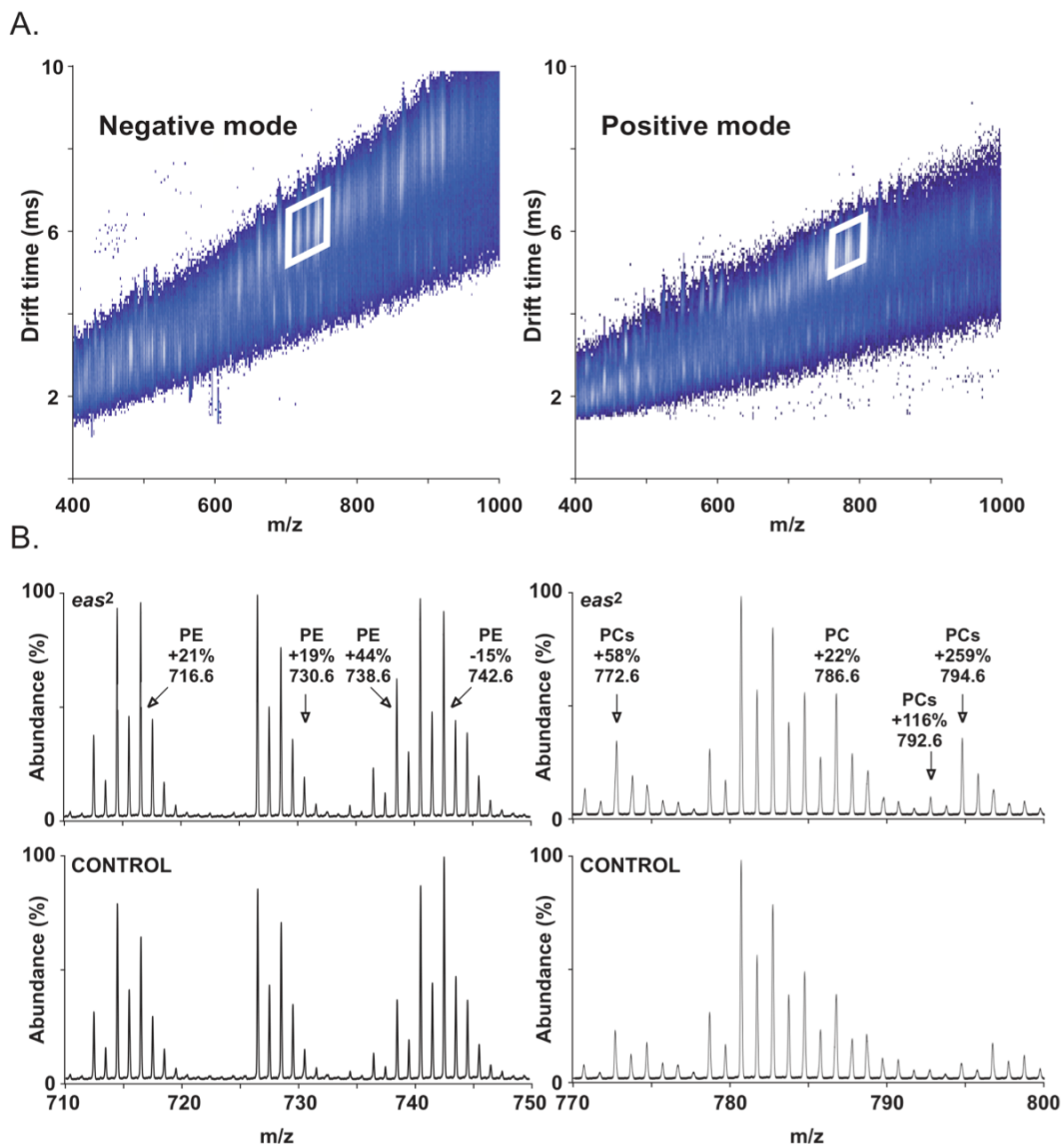
Figure 4.2 Spectral comparison of *eas* null versus control brains. (A) Raw 2D ion mobility drift time *vs. m/z* spectra used in the extraction of lipid signals in negative (left) and positive (right) ionization modes. (B) Comparison of wildtype control and eas^2 raw extracted mass spectra for the highlighted region of the lipid signal from the corresponding 2D spectrum. This spectral comparison of wildtype control and eas^2 null provides a visual illustration of changes later identified as significant by statistical analysis of aligned MS peak lists. M. Kliman, N. Vijayakrishnan, L. Wang, J.T. Tapp, K. Broadie, J.A. McLean, *Molecular BioSystems* **2010**, 6, 958-966. - Reproduced by permission of The Royal Society of Chemistry (RSC).

4.3.1 Changes in PtdEtn and PtdIns species in negative mode MALDI IM-MS

From negative mode MS experiments (Table 4.1, sections A and B) we identified five significantly changing (p<0.03) PtdEtn lipid species (36:2, 34:1, 36:4, 35:1, 38:3) and three significantly changing PtdIns lipid species (34:1, 36:2, 36:3) in the eas^2 null mutant brain compared to wt control. Three PtdEtn lipids show a significant increase in the mutant condition (34:1, +21.2%, p<0.001; 36:4, +43.6%, p<0.001; 35:1, +19.2%, p<0.03), whereas three PtdEtn species show a significant or nearly significant (p<0.10) concomitant decrease (36:2, -15.3%, p<0.001; 38:3, -20.8%, p<0.03; 36:3, -9.01%, p<0.1). In parallel, three PtdIns species display significant changes in the absence of ethanolamine kinase activity in the brain. Two PtdIns species show a significant or nearly significant decrease (34:1, -42.3%, p<0.01 and 34:2, -24.8%, p<0.1), while two show a significant increase (36:2, +41.1%, p<0.01; 36:3, +40.2%, p<0.01). Table 4.1 lists the 95% confidence intervals of the reported percent change values. Furthermore, in negative mode, we determined from fragmentation data the specific fatty acid composition of structures that result in the two most significantly changing PtdEtn and PtdIns signals, namely PtdEtn 36:2 (sn1-18:0/sn2-18:2), PtdEtn 34:1 (16:0/18:1), PtdIns 34:1 (16:0/18:1), PtdIns 36:2 (18:0/18:2).

4.3.2. Changes in PtdCho and PtdEtn in positive-mode MALDI IM-MS

In cells, PtdEtn can be synthesized by decarboxylation of phosphatidylserine (PtdSer) and reversible methylation from PtdCho.[20] We therefore examined the relative abundance of these species via positive mode analysis in the *eas*[2] null versus wildtype brain (Table 4.1 C and Table 4.2).

Table 4.1 Changes in PtdEtn, PtdIns and PtdCho lipids observed in negative and positive ionization modes between wild type control and *eas* mutant brains.[41]

Identity[a]	avg. m/z[b] (stdev)	% change between wt control and *eas* (95% conf. interval)	raw p value[c]	M.W. (exact) (detected as [M-H]- ion)[d]	M.W. (exact) (detected as [M+H]+ ion)[d]	M.W. (exact) (detected as [M+Na]+ ion)[d]	M.W. (exact) (detected as [M+K]+ ion)[d]
A. Negative mode significant PtdEtn (PE) lipid changes							
PE 36:2	742.60 (0.008)	-15.3 (-20.2, -10.2)	3.E-05	743.55			
PE 34:1	716.58 (0.006)	+21.2 (13.4 , 29.5)	2.E-05	717.53			
PE 36:4	738.56 (0.009)	+43.6 (26.0, 63.7)	4.E-05	739.52			
PE 35:1	730.63 (0.007)	+19.2 (3.97, 36.7)	2.E-02	731.55			
PE 38:3	768.60 (0.011)	-20.8 (-35.0, -3.52)	2.E-02	769.56			
PE 36:3	740.58 (0.008)	-9.01 (-18.8, 2.01)	0.099	741.53			
B. Negative mode significant PtdIns (PI) lipid changes							
PI 34:1	835.59 (0.010)	-42.3 (-57.9, -20.9)	2.E-03	836.54			
PI 36:2	861.62 (0.010)	+41.1 (15.3, 72.7)	3.E-03	862.56			
PI 36:3	859.59 (0.007)	+40.2 (12.2, 75.2)	6.E-03	860.54			
PI 34:2	833.58 (0.008)	-24.8 (-46.8, 6.09)	0.097	834.53			
C. Positive mode significantly changing signals with highest PtdEtn (PE) contribution							
PE 36:3 PC 35:6 PC 32:4 PC 33:3	764.54 (0.005)	-36.1 (-41.7, -29.9)	6.E-08		763.51	741.53 741.53 (<10%)	725.50 (<20%)
PE 36:2 PC 35:5 PC 32:3 PC 33:2	766.56 (0.006)	-33.6 (-39.4, -27.2)	2.E-07		765.53	743.55 743.55 (<10%)	727.51 (<20%)
PE 35:3 PC 32:3	750.56 (0.006)	-35.0 (-42.0, -27.3)	5.E-07			727.52 727.52	
PE 35:2 PC 32:2	752.57 (0.007)	-22.1 (-29.1, -14.5)	6.E-05			729.53 729.53	
PE 34:3 PC 30:4	736.52 (0.009)	-15.6 (-23.8, -6.62)	3.E-03			713.50	697.47 (<20%)
PE 36:1 PC 33:1 PC 35:4 PC 32:2	768.57 (0.008)	-8.27 (-15.9, 0.05)	0.051		767.55	745.56 745.56	729.57 (<10%)

Table 4.1 Notes: (a) Lipid identities determined by fragmentation and closest mass matches. Contribution from lipids with plasmalogen (p) and ether fatty acid linkages (o) cannot be determined at the mass resolution of the instrument (PE=PtdEtn, PI=PtdIns, PC=PtdCho, ex. PE X:Y, where X is the total number of carbons and Y is the total number of double bonds in the fatty acyl chains).
(b) Average and standard deviation of detected *m/z* from 18 measurements (9 control, 9 mutant)
(c) Only p values less than 3.E-02 were deemed significant
(d) Exact monoisotopic molecular weight of the identified lipid detected as either [M-H]-, [M+H]+ or metal (Na, K) coordinated ion. M. Kliman, N. Vijayakrishnan, L. Wang, J.T. Tapp, K. Broadie, J.A. McLean, *Molecular BioSystems* **2010**, 6, 958-966. - Reproduced by permission of The Royal Society of Chemistry (RSC).

The analysis of fragment spectra revealed protonated and sodium and potassium coodinated PtdCho signals with characteristic peaks at 184, 147, and 163 *m/z* respectively. PtdCho species constituted nearly 80% of significantly changing signals in positive mode. Fragmentation analysis of the remaining signals revealed primarily contribution from PtdEtn, with characteristic peaks at 164 and 146 *m/z*, and secondary contributions from isobaric (same *m/z*) PtdCho lipids. Most of the significantly changing positive mode signals have overlapping contribution from multiple lipids; however, overall lipid class changes can be readily characterized. Importantly, all statistically significant signals with primarily PtdEtn contribution in positive mode (Table 4.1 C) decrease in the *eas*[2] null condition (36:3+Na, -36.1%, p<0.001; 36:2+Na, -33.6%, p<0.001; 35:3+Na, -35.0%, p<0.001, 35:2+Na, -22.1%, p<0.001; 34:3+Na, -15.6%, p<0.01, 36:1+Na, -8.27%, p<0.06). Table 4.1 lists the 95% confidence intervals of the reported percent change values. Of the significantly changing signals with predominant PtdCho contribution, roughly half show a decrease in the *eas*[2] null brain (Table

90

4.2). Multiple significant PtdCho changes contain contributions from no more than one PtdCho lipid (32:0+H, +14.5%, p<0.001, 36:2+H, +21.5%, p<0.001; 36:1 + H, -40.3%, p<0.01; 34:1+H, +13.3%, p<0.01; 34:2+H, +23.6%, p<0.01; 36:4+Na, -17.8, p<0.03; 32:2+H, -11.1%, p<0.03). Table 4.2 lists the 95% confidence intervals of the reported percent change values. Based on normalized MS intensity values, there is a significant overall increase (12%) of PtdCho in brain lacking ethanolamine kinase activity.

Table 4.2 Changes in PtdCho lipids observed in positive ionization mode between wild type control and *eas* mutant brains.[41]

Identity[a]	avg. m/z[b] (stdev)	% change between wt control and *eas* (95% conf. interval)	raw p value	M.W. (exact)[c] (detected as [M-H+2Na]+ion)	M.W. (exact)[c] (detected as [M+H]+ ion)	M.W. (exact)[c] (detected as [M+Na]+ ion)	M.W. (exact)[c] (detected as [M+K]+ ion)
		Positive mode significantly changing signals with highest PtdCho (PC) contribution					
PC 35:2 **PC 34:3**	794.60 (0.022)	+259 (227, 294)	8.E-14			771.58	755.55
PC 32:1 **PC 35:3** **PC 33:0** **PE 35:4**	770.59 (0.024)	+96.2 (71.4, 125)	1.E-08	725.50	769.56	747.58	731.55
PC 35:3 **PC 34:4**	792.59 (0.024)	+116 (84.8, 151)	1.E-08			769.56	753.54
PC 35:2 **PC 32:0** **PE 35:3**	772.60 (0.041)	+58.3 (36.1, 84.2)	8.E-06	727.52	771.58		733.57
PC 32:0	734.59 (0.006)	+14.5 (8.57, 20.7)	8.E-05		733.57		
PC 36:5 **PC 37:1**	802.55 (0.008)	-28.6 (-36.2, -20.0)	2.E-05		801.62	779.55	
PC 30:0 **PC 32:3**	728.57 (0.006)	-22.6 (-29.3, -15.1)	3.E-05		727.51	705.53	
PC 31:0 **PC 33:3** **PE 34:0** **PC 30:1**	742.56 (0.005)	-20.6 (-27.9, -12.5)	2.E-04		741.53	719.55 719.55(<20%)	703.51(<20%)
PC 32:4 **PC 33:0** **PE 35:4**	748.59 (0.046)	-34.4 (-45.2, -21.5)	2.E-04		747.58	725.50 725.50 (<10%)	
PC 33:2 **PC 32:6**	744.58 (0.006)	-23.3 (-32.0, -13.5)	3.E-04		743.55	721.47	
PC 36:2	786.61 (0.009)	+21.5 (9.4, 34.9)	1.E-03		785.59		
PC 32:1 **PE 32:2**	732.58 (0.005)	+29.4 (12.5, 48.7)	1.E-03	687.48	731.55		
PC 34:3 **PC 32:0**	756.57 (0.003)	+8.5 (3.46, 13.8)	3.E-03		755.55	733.56	
PC 36:0 **PE 36:1**	790.56 (0.009)	-19.7 (-29.6, -8.53)	3.E-03	745.56	789.62		
PC 36:1	788.60 (0.032)	-40.3 (-56.1, -18.9)	3.E-03		787.61		

	m/z avg (std)	% change (CI)	p			
PC 34:1	760.59 (0.007)	+13.3 (4.88, 22.3)	4.E-03	759.58		
PC 36:2 **PC 38:5**	808.60 (0.005)	+17.3 (5.63, 30.3)	6.E-03	807.58		785.59
PC 34:2	758.58 (0.004)	+23.6 (7.37, 42.3)	6.E-03	757.56		
PC 32:1 **PC 34:3** **PE 35:1**	754.56 (0.006)	+15.6 (4.77, 27.7)	7.E-03	753.53	731.55 (<20%)	731.55
PC 31:3 **PE 32:0**	714.53 (0.008)	-15.8 (-26.1, -4.01)	1.E-02	713.50	691.52	
PC 34:2 **PC 37:4** **PC 35:1**	796.57 (0.018)	+38.9 (8.03, 78.5)	1.E-02	795.58	773.59 (<20%)	757.56
PC 36:4	804.57 (0.006)	-17.8 (-30.0, -3.60)	2.E-02		781.56	
PC 30:5 **PC 31:1**	718.56 (0.005)	+23.6 (3.38, 47.8)	2.E-02	717.53 (<20%)	695.45	
PC 32:2	730.58 (0.006)	-11.1 (-19.8, -1.43)	0.028	729.53		

Table 4.2 Notes: (a) Lipid identities determined by fragmentation and closest mass matches. Contribution from lipids with plasmalogen (p) and ether fatty acid linkages (o) cannot be determined at the mass resolution of the instrument (PC=PtdCho, PE=PtdEtn, ex. PE X:Y, where X is the total number of carbons and Y is the total number of double bonds in the fatty acyl chains).
(b) Average and standard deviation of detected *m/z* from 18 measurements (9 control, 9 mutant)
(c) Exact monoisotopic molecular weight of the identified lipid detected as either [M-H]-, [M+H]+ or metal (Na, K) coordinated ion. M. Kliman, N. Vijayakrishnan, L. Wang, J.T. Tapp, K. Broadie, J.A. McLean, *Molecular BioSystems* **2010**, 6, 958-966. - Reproduced by permission of The Royal Society of Chemistry (RSC).

These results reveal that specific molecular lipids may either be biosynthetically up or down regulated in the *Drosophila eas* mutant. Such changes could not be elucidated by previous TLC techniques examining gross changes in glycerophospholipid levels.[12]

4.4 Discussion

Drosophila bang-sensitive paralytic mutants such as *easily shocked* provide an exceptionally well characterized genetic model of epilepsy.[5-8, 11, 21]

However, using traditional TLC methods the mechanistic link between the *eas* epileptic phenotype and phosphatidylethanolamine (PtdEtn) metabolism could only be superficially assayed from whole head tissue and body.[12] In the current study, we developed a MALDI-IM-MS measurement strategy to directly assay relative phospholipid levels directly from dissected central brains. Ethanolamine kinase is required for the synthesis of PtdEtn via the Kennedy pathway, just one of several pathways available for PtdEtn synthesis (Figure 4.3).[22,23] We therefore examined the levels of PtdEtn and biosynthetically related lipids directly and selectively from brain tissue.

Previous studies[5,12] required large amounts (>100) of whole animals and/or heads to solvent extract the lipids and to subsequently perform TLC. In the current study, we assayed individual central brains from 9 wt control and 9 *eas*[2] mutant animals. Intact lipid masses were detected directly from central brain tissue without the need for extraction and reagent-based detection. This approach minimizes potential contamination and oxidative degradation, while providing a detailed molecular view of relevant lipid changes.

Based on differences in the composition of the lipid headgroup, different classes of lipids are more likely to ionize in the negative or the positive mode.[24,25] For example, PtdEtn, PtdIns, fatty acids, phosphatidylglycerol (PG) preferentially ionize in negative mode, while positive mode ionization can be expected of PtdCho and PtdSer. In the ethanolamine kinase null brain, we identified 38 significantly changing (p<0.03) lipid species from >1200 lipid signals, 8 via negative mode and 30 via positive mode. Due to high abundance of PtdEtn in the

Drosophila brain, several signals containing significant contributions of PtdEtn were identified in both negative and positive modes while no significantly changing PtdSer signals were detected.

By examining specific lipid species in this work, we found that not all PtdEtn lipids decrease in the *eas* mutant as was previously reported.[5,12] Specifically, five PtdEtn species, expected to be made by the CDP-ethanolamine biosynthetic pathway (Figure 4.3)[22,23,26] show a significant decrease in the *eas²* null brain. In contrast, three PtdEtn species, expected to be made primarily by the alternate PtdSer decarboxylase pathway (Figure 4.3), show a significant increase in the mutant condition. In negative mode, the trend set by the two most significantly changing PtdEtn 36:2 (down) and PtdEtn 34:1 (up) is exactly opposite for the two most significantly changing PtdIns 36:2 (up) and PtdIns 34:1 (down). The fatty acid composition and position in the respective PtdEtn/PtdIns 36:2 and PtdEtn/PtdIns 34:1 is the same. In positive mode, except for PtdEtn 36:2, the significantly changing signals with predominant PtdEtn contribution are not the same as the PtdEtn lipid species detected in negative mode, most likely due to preferential ionization of different PtdEtn species in positive and negative ionization modes. The PtdEtn 36:2 signal that appears in both modes shows a significant decrease in *eas²* null mutant brain. The decrease in positive mode is more pronounced and is most likely due to the presence of overlapping PtdCho signals that also decrease in the mutant condition, for which we see evidence in Table 4.2 (*i.e.*, significant decrease in signals with PtdCho 32:3 and PtdCho 33:2 contribution).
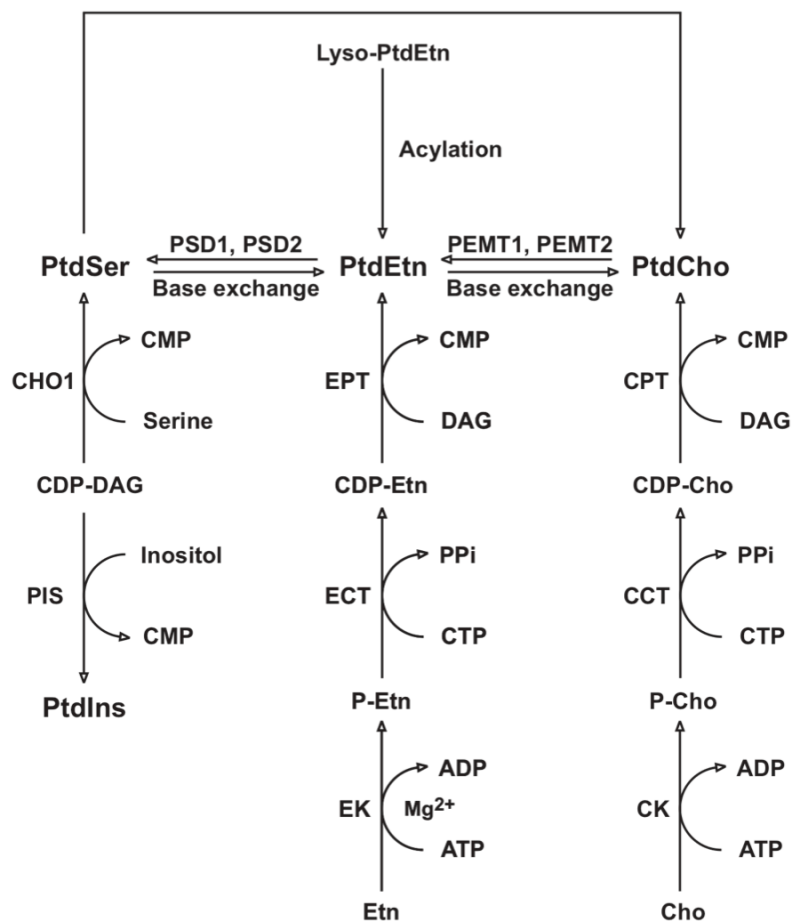
Figure 4.3 Schematic diagram of the known PtdEtn biosynthetic pathways. PtdEtn can be synthesized by several routes. The major route is the CDP-Etn pathway (Kennedy Pathway). Dietary Etn is converted to PtdEtn, by the stepwise action of ethanolamine (Etn) kinase (encoded by the *Drosophila eas* locus), Etn cytidyltransferase (ECT) and Etn phosphotransferase (EPT). PtdEtn can also be produced by PtdSer decarboxylation and converted to PtdCho by sequential methylation. The known enzymes required for the various steps in the pathway are shown. Abbreviations: choline (Cho), phosphoethanolamine (P-Etn), phosphatidylinositol (PtdIns), phosphatidylethanolamine (PtdEtn), phosphatidylcholine (PtdCho), phosphocholine (P-Cho), phosphatidylserine (PtdSer). M. Kliman, N. Vijayakrishnan, L. Wang, J.T. Tapp, K. Broadie, J.A. McLean, *Molecular BioSystems* **2010**, 6, 958-966. - Reproduced by permission of The Royal Society of Chemistry (RSC).

4.5 Conclusions

The MALDI-IM-MS method reported here provides a rapid and sensitive assay to quantify phospholipid species, potentially providing a diagnostic tool in a variety of mutant and disease comparative studies. This method provides great molecular detail compared to traditionally used detection techniques. Future studies will optimize and adapt this method for the detection of other classes of lipids, many of which are lower in abundance. This method used in concert with genetic manipulations may shed new light on the regulation of lipid biosynthetic pathways and alterations that occur in a range of disease conditions.

4.6 Acknowledgements

References

---

[1] Voelker, D. R., Lipid Transport Pathways in Mammalian-Cells. *Experientia* **1990,** *46* (6), 569-579.

[2] Jones, H. E.; Harwood, J. L.; Bowen, I. D.; Griffiths, G., Lipid composition of subcellular membranes from larvae and prepupae of Drosophila melanogaster. *Lipids* **1992,** *27* (12), 984-7.

[3] Dobrosotskaya, I. Y.; Seegmiller, A. C.; Brown, M. S.; Goldstein, J. L.; Rawson, R. B., Regulation of SREBP processing and membrane lipid production by phospholipids in Drosophila. *Science* **2002,** *296* (5569), 879-83.

[4] Seegmiller, A. C.; Dobrosotskaya, I.; Goldstein, J. L.; Ho, Y. K.; Brown, M. S.; Rawson, R. B., The SREBP pathway in Drosophila: regulation by palmitate, not sterols. *Dev Cell* **2002,** *2* (2), 229-38.

[5] Pavlidis, P.; Ramaswami, M.; Tanouye, M. A., The Drosophila easily shocked gene: a mutation in a phospholipid synthetic pathway causes seizure, neuronal failure, and paralysis. *Cell* **1994,** *79* (1), 23-33.

[6] Benzer, S., From the gene to behavior. *Jama* **1971,** *218* (7), 1015-22.

[7] Reynolds, E. R.; Stauffer, E. A.; Feeney, L.; Rojahn, E.; Jacobs, B.; McKeever, C., Treatment with the antiepileptic drugs phenytoin and gabapentin ameliorates seizure and paralysis of Drosophila bang-sensitive mutants. *J Neurobiol* **2004,** *58* (4), 503-13.

[8] Pavlidis, P.; Tanouye, M. A., Seizures and failures in the giant fiber pathway of Drosophila bang-sensitive paralytic mutants. *J Neurosci* **1995,** *15* (8), 5810-9.

[9] Hekmat-Scafe, D. S.; Dang, K. N.; Tanouye, M. A., Seizure suppression by gain-of-function escargot mutations. *Genetics* **2005,** *169* (3), 1477-93.

[10] Glasscock, E.; Singhania, A.; Tanouye, M. A., The mei-P26 gene encodes a RING finger B-box coiled-coil-NHL protein that regulates seizure susceptibility in Drosophilia. *Genetics* **2005,** *170* (4), 1677-89.

[11] Song, J.; Tanouye, M. A., Seizure suppression by shakB2, a gap junction mutation in Drosophila. *J Neurophysiol* **2006,** *95* (2), 627-35.

[12] Nyako, M.; Marks, C.; Sherma, J.; Reynolds, E. R., Tissue-specific and developmental effects of the easily shocked mutation on ethanolamine kinase activity and phospholipid composition in Drosophila melanogaster. *Biochem Genet* **2001,** *39* (9-10), 339-49.

13. Hsu, F. F.; Turk, J., Electrospray ionization with low-energy collisionally activated dissociation tandem mass spectrometry of glycerophospholipids: Mechanisms of fragmentation and structural characterization. *Journal of Chromatography B-Analytical Technologies in the Biomedical and Life Sciences* **2009,** *877* (26), 2673-2695.

14. Thomas, M. C.; Mitchell, T. W.; Harman, D. G.; Deeley, J. M.; Murphy, R. C.; Blanksby, S. J., Elucidation of double bond position in unsaturated lipids by ozone electrospray ionization mass spectrometry. *Analytical Chemistry* **2007,** *79* (13), 5013-5022.

15. Brown, H. A.; Murphy, R. C., Working towards an exegesis for lipids in biology. *Nature Chemical Biology* **2009,** *5* (9), 602-606.

16. Fenn, L. S.; McLean, J. A., Biomolecular structural separations by ion mobility-mass spectrometry. *Analytical and Bioanalytical Chemistry* **2008,** *391* (3), 905-909.

17. Fenn, L. S.; Kliman, M.; Mahsut, A.; Zhao, S. R.; McLean, J. A., Characterizing ion mobility-mass spectrometry conformation space for the analysis of complex biological samples. *Analytical and Bioanalytical Chemistry* **2009,** *394* (1), 235-244.

18. McLean, J. A., The Mass-Mobility Correlation Redux: The Conformational Landscape of Anhydrous Biomolecules. *Journal of the American Society for Mass Spectrometry* **2009,** *20* (10), 1775-1781.

19. Puolitaival, S. M.; Burnum, K. E.; Cornett, D. S.; Caprioli, R. M., Solvent-free matrix dry-coating for MALDI Imaging of phospholipids. *Journal of the American Society for Mass Spectrometry* **2008,** *19* (6), 882-886.

20. Vance, J. E., Molecular and cell biology of phosphatidylserine and phosphatidylethanolamine metabolism. *Prog Nucleic Acid Res Mol Biol* **2003,** *75*, 69-111.

21. Ganetzky, B.; Wu, C. F., Indirect Suppression Involving Behavioral Mutants with Altered Nerve Excitability in Drosophila Melanogaster. *Genetics* **1982,** *100* (4), 597-614.

22. Riekhof, W. R.; Voelker, D. R., Uptake and utilization of lyso-phosphatidylethanolamine by Saccharomyces cerevisiae. *Journal of Biological Chemistry* **2006,** *281* (48), 36588-36596.

23. Bakovic, M.; Fullerton, M. D.; Michel, V., Metabolic and molecular aspects of ethanolamine phospholipid biosynthesis: the role of CTP : phosphoethanolamine

cytidylyltransferase (Pcyt2). *Biochemistry and Cell Biology-Biochimie Et Biologie Cellulaire* **2007,** *85* (3), 283-300.; Chang, Y. F.; Carman, G. M., CTP synthetase and its role in phospholipid synthesis in the yeast Saccharomyces cerevisiae. *Progress in Lipid Research* **2008,** *47* (5), 333-339.

24. Astigarraga, E.; Barreda-Gomez, G.; Lombardero, L.; Fresnedo, O.; Castano, F.; Giralt, M. T.; Ochoa, B.; Rodriguez-Puertas, R.; Fernandez, J. A., Profiling and imaging of lipids on brain and liver tissue by matrix-assisted laser desorption/ionization mass spectrometry using 2-mercaptobenzothiazole as a matrix. *Anal Chem* **2008,** *80* (23), 9105-14.

25. Jackson, S. N.; Wang, H. Y. J.; Woods, A. S., Direct profiling of lipid distribution in brain tissue using MALDI-TOFMS. *Analytical Chemistry* **2005,** *77* (14), 4523-4527.

26. Bleijerveld, O. B.; Brouwers, J. F.; Vaandrager, A. B.; Helms, J. B.; Houweling, M., The CDP-ethanolamine pathway and phosphatidylserine decarboxylation generate different phosphatidylethanolamine molecular species. *J Biol Chem* **2007,** *282* (39), 28362-72.

27. Menon, A. K.; Stevens, V. L., Phosphatidylethanolamine is the donor of the ethanolamine residue linking a glycosylphosphatidylinositol anchor to protein. *J Biol Chem* **1992,** *267* (22), 15277-80.

28. Bogdanov, M.; Sun, J.; Kaback, H. R.; Dowhan, W., A phospholipid acts as a chaperone in assembly of a membrane transport protein. *J Biol Chem* **1996,** *271* (20), 11615-8.

29. Emoto, K.; Umeda, M., An essential role for a membrane lipid in cytokinesis. Regulation of contractile ring disassembly by redistribution of phosphatidylethanolamine. *J Cell Biol* **2000,** *149* (6), 1215-24.

30. Beljebbar, A.; Amharref, N.; Leveques, A.; Dukic, S.; Venteo, L.; Schneider, L.; Pluot, M.; Manfait, M., Modeling and quantifying biochemical changes in C6 tumor gliomas by Fourier transform infrared imaging. *Anal Chem* **2008,** *80* (22), 8406-15.

31. Punnonen, K.; Hietanen, E.; Auvinen, O.; Punnonen, R., Phospholipids and fatty acids in breast cancer tissue. *Journal of cancer research and clinical oncology* **1989,** *115* (6), 575-8.

32. Pascual, A.; Chaminade, M.; Preat, T., Ethanolamine kinase controls neuroblast divisions in Drosophila mushroom bodies. *Dev Biol* **2005,** *280* (1), 177-86.

33. Giles, K.; Pringle, S. D.; Worthington, K. R.; Little, D.; Wildgoose, J. L.; Bateman, R. H., Applications of a travelling wave-based radio-frequency-only stacked ring ion guide. *Rapid Commun Mass Spectrom* **2004,** *18* (20), 2401-14.

34. Kenward, M. G.; Roger, J. H., Small sample inference for fixed effects from restricted maximum likelihood. *Biometrics* **1997,** *53* (3), 983-997.

35. Benjamini, Y.; Hochberg, Y., Controlling the False Discovery Rate - a Practical and Powerful Approach to Multiple Testing. *Journal of the Royal Statistical Society Series B-Methodological* **1995,** *57* (1), 289-300.

36. Hsu, F. F.; Turk, J., Charge-remote and charge-driven fragmentation processes in diacyl glycerophosphoethanolamine upon low-energy collisional activation: A mechanistic proposal. *Journal of the American Society for Mass Spectrometry* **2000,** *11* (10), 892-899.

37. Hsu, F. F.; Turk, J., Characterization of phosphatidylinositol, phosphatidylinositol-4-phosphate, and phosphatidylinositol-4,5-bisphosphate by electrospray ionization tandem mass spectrometry: A mechanistic study. *Journal of the American Society for Mass Spectrometry* **2000,** *11* (11), 986-999.

38. Murphy, R. C.; Hankin, J. A.; Barkley, R. M., Imaging of lipid species by MALDI mass spectrometry. *Journal of Lipid Research* **2009,** *50*, S317-S322.

39. Simoes, C.; Simoes, V.; Reis, A.; Domingues, P.; Domingues, M. R., Determination of the fatty acyl profiles of phosphatidylethanolamines by tandem mass spectrometry of sodium adducts. *Rapid Commun Mass Spectrom* **2008,** *22* (20), 3238-44.

40. Stubiger, G.; Pittenauer, E.; Allmaier, G., MALDI seamless postsource decay fragment ion analysis of sodiated and lithiated phospholipids. *Analytical Chemistry* **2008,** *80* (5), 1664-1678.

41. Kliman, M.; Vijayakrishnan, N.; Wang, L.; Tapp, J. T.; Broadie, K.; McLean, J. A., Structural mass spectrometry analysis of lipid changes in a Drosophila epilepsy model brain. *Molecular BioSystems* **2010,** *6* (6), 958-966.

CHAPTER V

Dynamic Light Patterning for High Spatial

Resolution Imaging of Lipids

5.1 Introduction

Biomolecular imaging mass spectrometry has been successfully applied to spatial characterization of peptides and proteins, and more recently lipids.[1,2,3] In imaging MS, tissue slices,[4,5] cellular monolayers,[6,7] even individual cells or vesicles deposited on a flat substrate,[8,9,10] can be spatially interrogated by dividing their area into a regular 2-D array of pixels and obtaining a full MS profile at each pixel.[11,12] The mass to charge and intensity (*i.e.*, % relative abundance) information of the MS spectra at each pixel can be combined into abundance images of individual m/z signals using specialized free and proprietary MS imaging software. MS image spatial resolution is limited by the size of each pixel and the step size (*i.e.*, smallest unit of lateral movement with respect to laser impact) of the sample stage.

Matrix assisted laser desorption ionization (MALDI) appears to be well suited for spatial interrogation of larger (*i.e.*, >500 Da) lipid species at resolutions of tens of micrometers,[2] while secondary ionization mass spectrometry (SIMS), especially in combination with energy absorbing matrices on imaged surfaces can provide spatial information about cholesterol mass range lipids, fatty acids and lipid fragments at hundreds of nanometers spatial resolution.[13,14] Currently

neither MALDI nor SIMS are particularly well suited for imaging of intact lipids at resolutions of *ca.* one micrometer.[15]

Several recent developments have led to improvements in the imaging resolution attainable by laser light ionization. New matrix deposition methods, such as sublimation,[11,16] dry matrix deposition,[17,18] and metal nanoparticles[19,20] have been shown to provide surfaces that do not constrain mass imaging spatial resolution by matrix crystal size; others have used nanostructured surfaces to overcome this limitation.[21] Another approach to increased resolution of MALDI experiments is improving the final focus of the ionizing laser beam at the sample surface. Tighter focus of the laser beam leads to smaller pixel size of the resulting MS image, and therefore to higher imaging spatial resolution.[22] Highly sensitive MS platforms that offer detection of all ionized species, such as time-of-flight MS instruments are best suited for typical high resolution MALDI imaging with organic matrix compounds, due to the relatively low ionization efficiency of the organic matrix assisted LDI process (*i.e.*, one ion estimated for every ten thousand neutral desorbed species).[23] However, size selected nanoparticles with much higher ionization efficiencies currently explored by several groups have the potential to substantially improve lipid detection in high spatial resolution experiments on an expanded number of instrumental platforms.[24,25,26,27]

In principle, the focusing ability of any laser optics for MALDI imaging is limited by the properties of laser light (*i.e.*, spot size and shape, divergence, and wavelength) and the diffraction limited demagnification of the laser optics. Current approaches to sub-micron focusing of laser beams require positioning of

optical components close to the imaged surface.[28,29] Such methods require custom optics and specialized instrumental hardware, and are limited to producing symmetrical (i.e., typically round) laser spot shapes. Building on previous work by Sherrod et al.,[30] I optimized a digital micro-mirror array (DMA) device for laser focusing and user defined laser patterning coupled to a highly sensitive commercial TOF MS instrument. This approach does not require positioning of optics close to the imaged surface inside the vacuum of the ion source, and has the potential to transfer seamlessly between different MS instrumental platforms, including commercial IM-MS instruments. When coupled to IM-MS instrumentation, such system has the potential to offer high resolution spatial interrogation of lipids, while simultaneously allowing their mobility separation from concomitant biomolecular signals.

5.2 Experimental

5.2.1 DMA optical train

The MS imaging laser optics shown in Figure 5.1 consist of the pulsed laser as described in section 5.2.2, optional beam homogenizer (2 microlens arrays and 2 cylindrical fourier-lenses) used to generate a flat laser beam energy profile, a digital micro mirror array (DMA) device based on the digital light patterning (DLP) technology, a set of 2 cylindrical filed lenses for correction of laser light divergence post DMA reflection and a final objective triplet lens with a focal length f =125 mm (BLZ-Bayerisches Laserzentrum, Erlagen, Germany).

The demagnification ratio β depends on the following properties of the optical setup: a is the distance between DMA and objective lens, b is the distance between the objective lens and MALDI target, f is the focal length of the objective lens, u is object height (size of area selected at DMA), and v is image height (size of focuses area projected onto the MALDI target). The properties of projection can be calculated with the following equations. Magnification $\beta = \dfrac{v}{u} = \dfrac{b}{a}$ and image distance $b = f(1+\beta)$. Thus increasing the distance a between the DMA device and objective results in a smaller demagnification ratio β (*i.e.*, smaller size image on the MALDI target). Optical support equipment (i.e., rails, stages, posts, and post holders) were purchased from OptoSigma (Santa Ana, CA) and Newport (Irvine, CA).

5.2.2 TOF-MS instrumentation

MS imaging data was collected on a high-resolution MALDI – TOF MS instrument (Voyager DE – STR, Applied Biosystems, Foster City, CA) operated in linear or reflectron modes. A 337 nm N_2 laser operated at 20Hz was utilized for MS signal and instrument method optimization, while a frequency-tripled Spectra-Physics (Newport, Irvine, CA) Nd:YLF (349nm) µJ energy range laser and a Tempest (ESI, Portland, OR) Nd:YAG (355 nm) flash lamp pumped mJ energy range laser were used for MALDI-TOF MS imaging either at default 3Hz or optimized 20Hz frequencies.

5.2.3 Sample preparation

Initial optics and instrument optimization were performed with cardiac peptide bradykinin and MALDI matrices α-Cyano-4-hydroxycinnamic acid (α-Cyano) and 2,5-dihydroxybenzoic acid (DHB), which were purchased from Sigma (St. Louis, MO) and used without further purification. For optimal signal intensity testing bradykinin 0.1mg/mL water solution was dissolved in 30 mg/mL α-Cyano in methanol (MeOH), pipetted at 1 µL amounts onto 2x2mm wells of an Applied Biosystems standard 100 well steel MALDI plate and flash evaporated under vacuum. For initial laser beam imaging either DHB or α-Cyano were dissolved at 3mg/mL concentration in MeOH and pipetted onto 45x45 mm indium tin oxide (ITO) coated glass slides and air dried. ITO slides were then mounted into Applied Biosystems standard gold plate MALDI plate holder.

5.2.4 Monolayer cell culture protocol

HT1080 cells (*i.e.*, a human fibroblast like cell line) were maintained in Dulbeco's Modified Eagles Medium (DMEM) (Invitrogen) with 10% fetal bovine serum (FBS) (HyClone, Logan, UT) and 1% penicillin/streptomycin (Invitrogen). Cells were then trypsinized with 0.25% Trypson-EDTA (Invitrogen) and plated on ITO slides (previously sterilized under UV light). Cells were allowed to become confluent, and a scratch wound was made using a 20 µL pipette tip. Three hours post wounding, the growth media was removed and the sample was washed twice with PBS. Excess PBS was aspirated, and the sample was frozen at -80°C. For analysis the ITO slides were vacuum dried and equilibrated to room

temperature. Before imaging the monolayers were coated with nanoparticle elemental gold using a Cressington 108 manual sputter coater (Ted Pella, Redding, CA). Optimal tissue silver coating times at half maximum height of the sputter coater sample stage were between 15 and 30 seconds.

5.2.5 Tissue sectioning and coating

Mice were bred in Division of Animal Care facilities at Vanderbilt University. Embryos at E20 or postnatal, day 0, pups were dissected. Heads were removed, brains were rapidly dissected, and instantly frozen in precooled 2-methylbutane (on dry ice) and stored at -80ºC until sectioning. Coronal cryostat sections (10 to 50 μm thick) were prepared from fresh frozen KO and WT brains. All procedures were performed in accordance with the Guide for the Humane Use and Care of Laboratory Animals. The use of mice in this study was approved by the IACUC of the Vanderbilt University.

Tissue sections were thaw mounted on metal MALDI plates, microscope or indium tin oxide (ITO) glass slides. All sections were stored in -80°C freezer until analysis. Before imaging the tissues were coated with nanoparticle elemental silver using a Cressington 108 manual sputter coater (Ted Pella, Redding, CA). Optimal tissue silver coating times at half maximum height of the sputter coater sample stage were between 5 and 15 seconds.

5.3 Results and Discussion

Mass spectrometry imaging has demonstrated great potential for spatially profiling biomolecular content of tissues and cells.[10,22,31] The main advantage of this technology is that biomolecules are intrinsically labeled by mass, and also by size and thus it is well suited for studies characterizing the distribution of lipid species directly from complex biological samples, especially in combination with IM-MS instrumentation as described in chapters 1 to 4.

In contrast with contemporary MS imaging using matrix assisted laser desorption/ionization (MALDI), the proposed dynamic light patterning MALDI optical system for MS imaging provides 5 significant advantages: (1) diffraction limited spatial resolution at UV laser wavelengths of < 1 μm (compared with *ca.* 30-150μm in typical MALDI experiments), (2) the ability to generate complex shapes for selective ionization from user defined cellular regions, (3) selective and simultaneous ionization can be performed from multiple non-congruent regions, (4) the ability to rapidly raster the laser across the sample optically, rather than physically moving the target, and (5) elimination of perspective distortion from ionization at oblique angles relative to the target.[32,33,34] In my dissertation work I focused on optimization of parameters needed to attain the first three advantages.

The principal component of the new optical system is a digital micro-mirror array (DMA) device, described in mid-1980s by Hornbeck.[35] DMA device is a 1x1.5 cm array of *ca.* one million 13x13 μm size mirrors. Each one of the micro-

mirrors can be individually controlled to tilt + or − 12 degrees to either reflect or deflect parts of an incident laser beam (Figure 5.1). Using this device the laser beam can be patterned at the MALDI target into regular or complex shapes of variable dimensions and even non-congruent spatial regions can be irradiated simultaneously. Importantly, the ability to use the DMA as a non-diffractive aperture to reflect micron sized laser beams and focus these using a high numerical aperture triplet lens objective allows sub-micron laser beam sizes at the MALDI target.
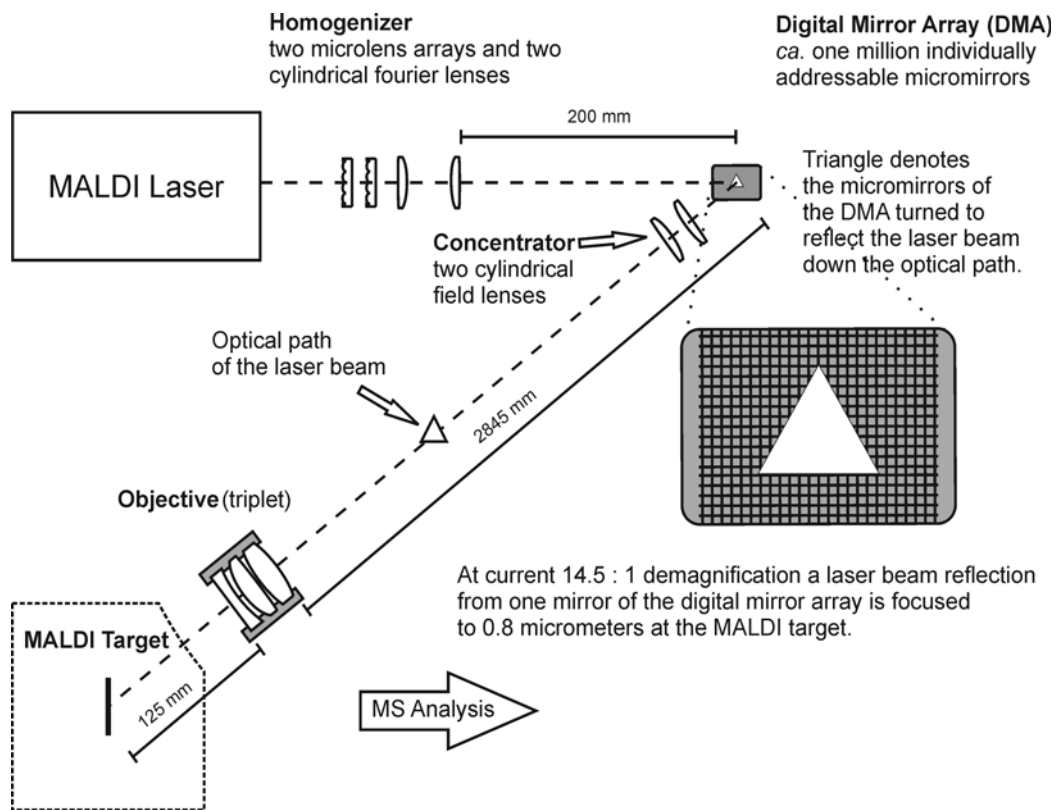
Figure 5.1 A schematic of the optical arrangement incorporating laser light patterning with a digital micro-mirror array. Regular (*e.g.* triangular, elliptical) or irregular laser patterns can be reflected and focused at the MALDI target. The current demagnification ratio allows ionization experiments with a spatial resolution of *ca.* 800 nm.

Prior to reflection from the DMA a laser homogenizer can be used to produce a laser beam with uniform photon density to ensure a uniform energy profile across any arbitrary pattern at the target and therefore uniform ionization across such pattern. Owing to the potentially large demagnification of the individual micro-mirrors of the DMA (*i.e.* hundreds of nm in the diffraction limit of the objective triplet lens) the "true" image will be limited in pixel resolution to several hundred nm, which is still within an acceptable range for most imaging applications.
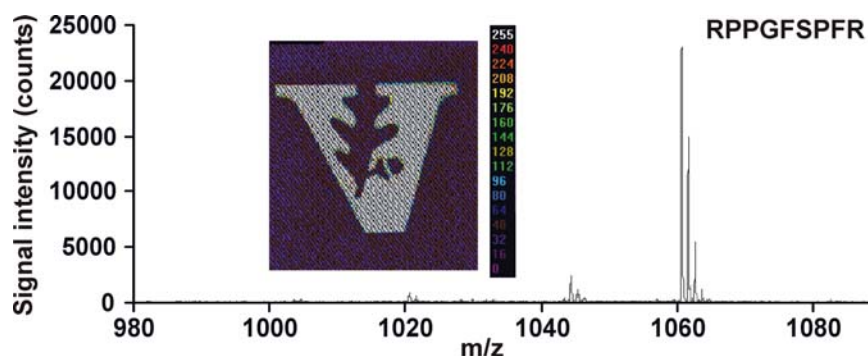
Figure 5.2 Mass spectrum of the peptide RPPGFSPFR ([M+H]$^+$ = 1060 m/z) obtained from an image generated by *ca.* 300000 mirrors on the DMA (200 µm at the MALDI target). Inset: the image of the patterned laser beam taken by a CCD camera confirmed that the homogenizer produces a beam with a flat-top energy profile, energy scale is right of inset.

After initial alignment, the work focused on demonstrating the patterning viability of the optical system proposed for cellular and sub cellular imaging. I was able to achieve MALDI ionization from a complex laser pattern of roughly 200 microns in size at the MALDI target, as shown in Figure 5.2, in initial experiments

with a standard MALDI Nitrogen gas laser. In subsequent testing, I installed a higher energy solid state diode laser into the optical train.

The solid state laser is capable of producing laser pulses at 120 µJ of energy per pulse, and provides about double fluence (*i.e.*, energy per unit of area) at the target compared to the Nitrogen gas laser first used. The increase in photon density achieved with the solid state laser at the MALDI target over the traditional Nitrogen laser led to a striking observation. The signal intensity obtained during initial experiments (10^4 counts from 0.1 pmoles of peptide RPPGFSPFR) with a 200 µm pattern reflected from *ca.* 300,000 mirrors at the DMA was also achieved when an equilateral triangle pattern from only 500 mirrors (*i.e.*, tens of µm at target) was used in sample ionization. To achieve ionization from this small a pattern, laser energy incident on the MALDI target was measured and found to be approximately double. I now predict that significant ionization can be induced from even smaller patterns as long as increased laser energy can be supplied at these resolutions. Our group has recently purchased a high power Tempest solid state laser to achieve ionization with even fewer mirrors.

Preliminary experiments demonstrate that at sufficient photon densities, significant amounts of signal can be expected from a single mirror with < 1 µm resolution at target. In the experiments with beam sizes of tens of µm, total integrated signal from 0.1 pmole of peptide RPPGFSPFR reached close to 1 million counts per laser shot, which is equivalent to *ca.* two thousand counts of signal per single mirror. More recently, patterns of 5 x 5 mirrors (size on the

target 4 x 4 μm) yielded 10^5 integrated signal counts and a pattern of 4 x 4

mirrors (size on the target 3.3 x 3.3 μm) yielded 10^3 counts of integrated signal.

Therefore, in terms of counts per mirror, I am now able to generate up to 40,000

counts per mirror from 5 x 5 mirror patterns and 6,000 counts per mirror from 4 x

4 mirror patterns. Based on previous work by the groups of Dr. Knochenmuss,

Dr. Zenobi, and Dr. Karas, I expect that the difference in counts per mirror as the

images decrease in size will be overcome by utilizing a higher energy MALDI

laser.

Laser images created on photosensitive paper and by laser ablation of

MALDI organic matrix at the MALDI target showing images prior to and after

perspective correction are shown in Figure 5.3.
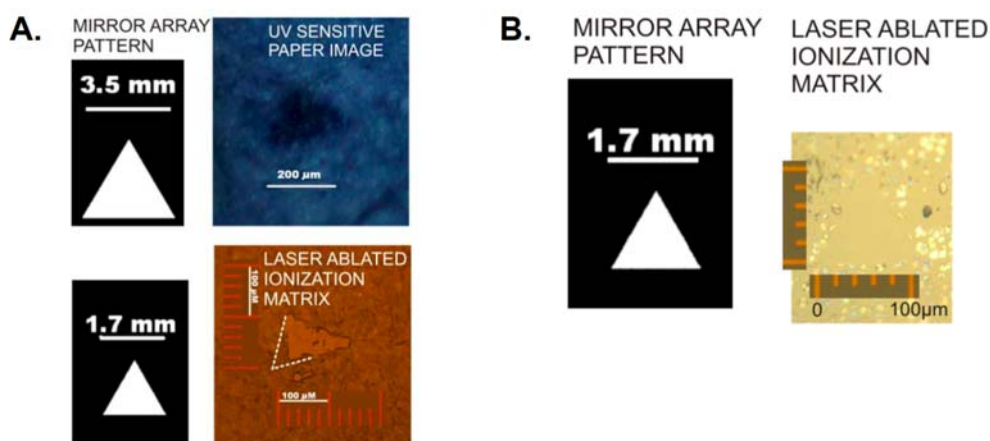
Figure 5.3 A. An equilateral triangle laser pattern with a side dimension of 3.5 mm at the mirror array focused onto a UV photosensitive paper (left) and an equilateral triangle pattern with side dimension of a 1.7 mm used to ablate a solid ionization matrix DHB (right). The dotted line delineates the area of partial DHB ablation which occurred due to excessive thickness corrected in later imaging experiments (see B.). **B.** An equilateral triangle laser pattern with side dimension of 1.7 mm at the mirror array was focused onto a thin monolayer of α-cyano-4-hydroxycinnamic acid MALDI matrix. The optical focus was modified manually to correct for perspective distortion observed in part A.

In Figure 5.3 the demagnification to obtain the resulting triangle side dimensions on ionization target is *ca.* 15:1 for all projected triangles. Under current experimental conditions this focusing power is sufficient to generate a < 1 μm image size from a laser beam reflected from a single mirror. The perspective distortion at the target in Figure 5.3A is due to the angle of incidence of the laser at the target plane, which has been manually corrected in Figure 5.3B.

To demonstrate the viability of the light patterning optics for high resolution MS lipid imaging of novel substrates, I imaged a monolayer of HT1080 cells, a human fibroblast like cell line, using a scratch-wound assay. In this assay, a confluent cell monolayer is scratched or "wounded" to generate an area denuded of cells, which causes the cells to become polarized and initiates directional migration to close the gap.[36] MS imaging was performed at the wound edge in the positive ion mode. These images correspond to choline containing lipids, such as phosphatidylcholines, and sphingomyelins. An example MS image across the wound edge is shown in Figure 5.4 for the phosphatidylcholine 34:1. In this image, a nominal spatial resolution of 29 μm was used, which is approximately one cell diameter. The highest intensity peaks for this particular lipid are *ca.* 10^4 counts, suggesting adequate sensitivity for the analysis of lipids at higher spatial resolution. The higher energy Tempest laser now available for DMA based MS imaging is expected to enhance MS imaging sensitivity even further.
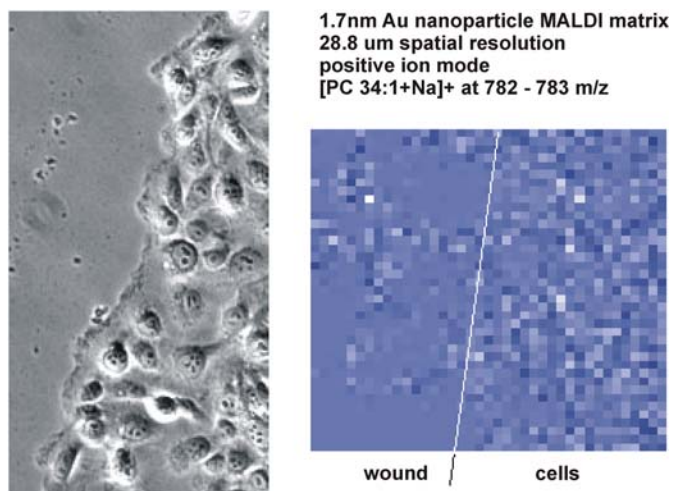
Figure 5.4 (Left) An optical micrograph of a wounded cell monolayer is shown. (Right) An extracted MS image of phosphatidylcholine 34:1 (m/z = 782-783) of a 1 x 1 mm square area of cells at the wound edge imaged at a resolution of 28.8 µm. Note that Au nanoparticles were used as the MALDI matrix. Some lipid signal was observed beyond the wound edge most likely reflecting a few cells (or parts of cells) that remained in the denuded area.

Further studies of these cellular monolayers will focus on MS imaging of lipids in both positive and negative modes at the wound edge. After wounding, the vast majority of cells become highly polarized and extend a leading edge protrusion into the wound in the direction of movement. Localized selective lipid composition at the leading edge is thought to be involved in cell polarization, which makes this assay ideal for studying lipids involved in migration. Thus, this measurement strategy potentially provides information for previously uncharacterized lipids involved in membrane polarization in support of cell migration. Temporal changes in concentration of various lipids can also be determined by imaging samples that were fixed at different time intervals after wounding. At higher spatial resolution, we will be able to outline and image a region that represents, for example, the first 800 nm behind the leading edge

membrane (Figure 5.5). Subsequently, we will continue to image in 800 nm intervals marching toward the interior of the cell. Thus, we can compare these images to assess the extent of lipid polarization within the various cellular regions. Importantly, because the proposed optical arrangement allows complex patterning of the laser we are not restricted to simple shapes. Therefore, we can accurately map the irregular contours of the cell.
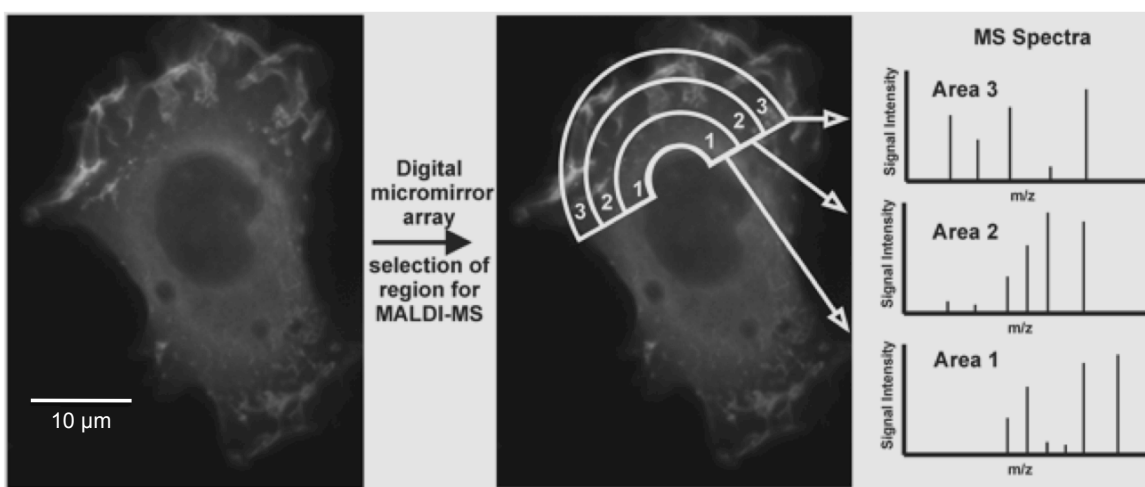
Figure 5.5 (left) An optical micrograph of a human fibrosarcoma HT1080 cell line serum polarized cell, where the leading edge protrusion appears at the top of the image. In this concept experiment, different regions of the optically imaged cell will be selectively targeted for laser desorption/ionization (center) and MS analyses, which may provide localized relative abundance of lipids, depending on the specific area to be analyzed (right). Typical cell diameter of individually grown and polarized HT1080 cells is 30 μm.

Previous experiments with peptide RPPGFSPFR showed that ionization from 5x5 and 4x4 μm laser spot sizes can be achieved, but requires considerably higher laser fluences. Toward the goal of imaging of endogenous compounds in cell monolayers and tissues at these spatial resolutions, we acquired a pulsed mJ laser that provides laser pulse energies in 1-30 mJ range, which translates

into one to two orders of magnitude higher fluences at the sample target than the fluences of nitrogen gas and diode lasers used at the beginning of this project. To test the capabilities of the new high energy laser I chose to image cholesterol distribution in coronal mouse tissue sections of various thicknesses, shown in Figure 5.6.
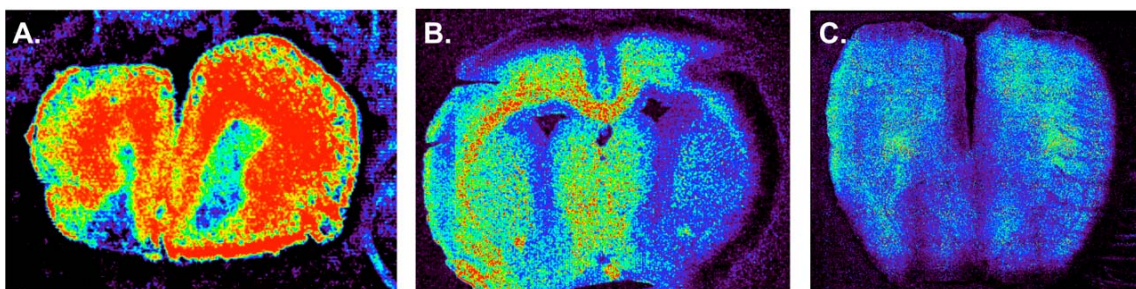
Figure 5.6. MS images of cholesterol silver adduct (*i.e.*, cholesterol+Ag$^+$ at 495.3 m/z) from three different coronal mouse brain sections, (A.) 10 micrometer tissue thickness, (B.) and (C.) 50 micrometer tissue thickness, at three different imaging spatial resolutions (A.) 20, (B.) 16, and (C.) 8 μm.

Notably, the silver nanoparticle coating protocol used in these experiments, coupled with higher laser fluence allowed imaging of tissues thicker than 10 μm typically used in laser desorption imaging experiments. I expect that further fine tuning of the sectioning, coating, and imaging protocols will soon allow similar lipid imaging of biological tissues and cells at or close to 1 μm resolution.

5.4 Conclusions

Mass spectrometry characterization of the spatial distribution of lipids in tissues and individual cells adds an important layer of information to the overall understanding of lipid function. Imaging methods based on laser desorption ionization have the potential to reveal the m/z distribution of lipids ionized and detected as intact molecules. In this work I built an optical system based on the digital micro-mirror array technology and tested its laser focusing and patterning capabilities. This system shows promise in bridging the current spatial resolution gap between the typical spatial resolutions currently afforded by the MALDI and SIMS imaging platforms. Since it does not require optics mounted inside the mass spectrometer, the DMA optical system can be aligned to other instrumental platforms, including MALDI IM-MS systems.

5.5 Acknowledgements

REFERENCES

[1] Caprioli, R. M.; Farmer, T. B.; Gile, J., Molecular imaging of biological samples: Localization of peptides and proteins using MALDI-TOF MS. *Analytical Chemistry* **1997,** *69* (23), 4751-4760.

[2] Stoeckli, M.; Chaurand, P.; Hallahan, D. E.; Caprioli, R. M., Imaging mass spectrometry: A new technology for the analysis of protein expression in mammalian tissues. *Nature Medicine* **2001,** *7* (4), 493-496.

[3] Burnum, K. E.; Cornett, D. S.; Puolitaival, S. M.; Milne, S. B.; Myers, D. S.; Tranguch, S.; Brown, H. A.; Dey, S. K.; Caprioli, R. M., Spatial and temporal alterations of phospholipids determined by mass spectrometry during mouse embryo implantation. *Journal of Lipid Research* **2009,** *50* (11), 2290-2298.

[4] Sjovall, P.; Lausmaa, J.; Johansson, B., Mass spectrometric imaging of lipids in brain tissue. *Analytical Chemistry* **2004,** *76* (15), 4271-4278.

[5] Chughtai, K.; Heeren, R. M. A., Mass Spectrometric Imaging for Biomedical Tissue Analysis. *Chemical Reviews* **2010,** *110* (5), 3237-3277.

[6] Malm, J.; Giannaras, D.; Riehle, M. O.; Gadegaard, N.; Sjovall, P., Fixation and Drying Protocols for the Preparation of Cell Samples for Time-of-Flight Secondary Ion Mass Spectrometry Analysis. *Analytical Chemistry* **2009,** *81* (17), 7197-7205.

[7] Zimmerman, T. A.; Rubakhin, S. S.; Sweedler, J. V., MALDI Mass Spectrometry Imaging of Neuronal Cell Cultures. *Journal of the American Society for Mass Spectrometry* **2011,** *22* (5), 828-836.

[8] Fletcher, J. S., Cellular imaging with secondary ion mass spectrometry. *Analyst* **2009,** *134* (11), 2204-2215.

[9] Szakal, C.; Narayan, K.; Fu, J.; Lefman, J.; Subramaniam, S., Compositional Mapping of the Surface and Interior of Mammalian Cells at Submicrometer Resolution. *Analytical Chemistry* **2011,** *83* (4), 1207-1213.

[10] Altelaar, A. F. M.; Luxembourg, S. L.; McDonnell, L. A.; Piersma, S. R.; Heeren, R. M. A., Imaging mass spectrometry at cellular length scales. *Nature Protocols* **2007,** *2* (5), 1185-1196.

[11] Murphy, R. C.; Hankin, J. A.; Barkley, R. M., Imaging of lipid species by MALDI mass spectrometry. *Journal of Lipid Research* **2009,** *50*, S317-S322.

[12] McDonnell, L. A.; Heeren, R. M. A., Imaging mass spectrometry. *Mass Spectrometry Reviews* **2007,** *26* (4), 606-643.

[13] Touboul, D.; Brunelle, A.; Laprevote, O., Mass spectrometry imaging: Towards a lipid microscope? *Biochimie* **2011,** *93* (1), 113-119.

[14] Nygren, H.; Malmberg, P.; Kriegeskotte, C.; Arlinghaus, H. F., Bioimaging TOF-SIMS: localization of cholesterol in rat kidney sections. *Febs Letters* **2004,** *566* (1-3), 291-293.

[15] Benabdellah, F.; Seyer, A.; Quinton, L.; Touboul, D.; Brunelle, A.; Laprevote, O., Mass spectrometry imaging of rat brain sections: nanomolar sensitivity with MALDI versus nanometer resolution by TOF-SIMS. *Analytical and Bioanalytical Chemistry* **2010,** *396* (1), 151-162.

[16] Grove, K. J.; Frappier, S. L.; Caprioli, R. M., Matrix Pre-Coated MALDI MS Targets for Small Molecule Imaging in Tissues. *Journal of the American Society for Mass Spectrometry* **2011,** *22* (1), 192-195.

[17] Puolitaival, S. M.; Burnum, K. E.; Cornett, D. S.; Caprioli, R. M., Solvent-free matrix dry-coating for MALDI Imaging of phospholipids. *Journal of the American Society for Mass Spectrometry* **2008,** *19* (6), 882-886.

[18] Kliman, M.; Vijayakrishnan, N.; Wang, L.; Tapp, J. T.; Broadie, K.; McLean, J. A., Structural mass spectrometry analysis of lipid changes in a Drosophila epilepsy model brain. *Molecular BioSystems* **2010,** *6* (6), 958-966.

[19] Goto-Inoue, N.; Hayasaka, T.; Zaima, N.; Kashiwagi, Y.; Yamamoto, M.; Nakamoto, M.; Setou, M., The Detection of Glycosphingolipids in Brain Tissue Sections by Imaging Mass Spectrometry Using Gold Nanoparticles. *Journal of the American Society for Mass Spectrometry* **2010,** *21* (11), 1940-1943.

[20] Taira, S.; Sugiura, Y.; Moritake, S.; Shimma, S.; Ichiyanagi, Y.; Setou, M., Nanoparticle-assisted laser desorption/ionization based mass imaging with cellular resolution. *Analytical Chemistry* **2008,** *80* (12), 4761-4766.

[21] Northen, T. R.; Yanes, O.; Northen, M. T.; Marrinucci, D.; Uritboonthai, W.; Apon, J.; Golledge, S. L.; Nordstrom, A.; Siuzdak, G., Clathrate nanostructures for mass spectrometry. *Nature* **2007,** *449*, 1033-U3.

[22] Chaurand, P.; Cornett, D. S.; Angel, P. M.; Caprioli, R. M., From Whole-body Sections Down to Cellular Level, Multiscale Imaging of Phospholipids by MALDI Mass Spectrometry. *Molecular & Cellular Proteomics* **2011,** *10* (2).

[23] Knochenmuss, R.; McCombie, G.; Faderl, M., Ion yields of thin MALDI samples: Dependence on matrix and metal substrate and implications for models. *Journal of Physical Chemistry A* **2006,** *110* (47), 12728-12733.

[24] McLean, J. A.; Stumpo, K. A.; Russell, D. H., Size-selected (2-10 nm) gold nanoparticles for matrix assisted laser desorption ionization of peptides. *Journal of the American Chemical Society* **2005,** *127* (15), 5304-5305.

[25] Castellana, E. T.; Russell, D. H., Tailoring nanoparticle surface chemistry to enhance laser desorption ionization of peptides and proteins. *Nano Letters* **2007,** *7,* 3023-3025.

[26] Gamez, F.; Hurtado, P.; Castillo, P. M.; Caro, C.; Hortal, A. R.; Zaderenko, P.; Martinez-Haya, B., UV-Vis-NIR Laser Desorption/Ionization of Synthetic Polymers Assisted by Gold Nanospheres, Nanorods and Nanostars. *Plasmonics* **2010,** *5* (2), 125-133.

[27] Shibamoto, K.; Sakata, K.; Nagoshi, K.; Korenaga, T., Laser Desorption Ionization Mass Spectrometry by Using Surface Plasmon Excitation on Gold Nanoparticle. *Journal of Physical Chemistry C* **2009,** *113* (41), 17774-17779.

[28] Stockle, R.; Setz, P.; Deckert, V.; Lippert, T.; Wokaun, A.; Zenobi, R., Nanoscale atmospheric pressure laser ablation-mass spectrometry. *Analytical Chemistry* **2001,** *73* (7), 1399-1402.

[29] Spengler, B.; Hubert, M., Scanning microprobe matrix-assisted laser desorption ionization (SMALDI) mass spectrometry: Instrumentation for sub-micrometer resolved LDI and MALDI surface analysis. *Journal of the American Society for Mass Spectrometry* **2002,** *13* (6), 735-748.

[30] Sherrod, S. D.; Castellana, E. T.; McLean, J. A.; Russell, D. H., Spatially dynamic laser patterning using advanced optics for imaging matrix assisted laser desorption/ionization (MALDI) mass spectrometry. *International Journal of Mass Spectrometry* **2007,** *262* (3), 256-262.

[31] Cornett, D. S.; Reyzer, M. L.; Chaurand, P.; Caprioli, R. M., MALDI imaging mass spectrometry: molecular snapshots of biochemical systems. *Nature Methods* **2007,** *4* (10), 828-833.

[32] McLean, J. A.; Minnich, M. G.; Montaser, A.; Su, J.; Lai, W., Optical patternation: A technique for three-dimensional aerosol diagnostics. *Analytical Chemistry* **2000,** *72* (20), 4796-4804.

[33] Lai, W.; Alfini, S.; Su, J., Development of an Optical Patternator for the Quantitative Characterization of Liquid Sprays. *10th International Symposium on Applications of Laser Techniques to Fluid Dynamics* July **2000**, Lisbon, Portugal.

[34] Minnich, M. G.; McLean, J. A.; Montaser, A., Spatial aerosol characteristics of a direct injection high efficiency nebulizer via optical patternation. *Spectrochimica Acta Part B-Atomic Spectroscopy* **2001,** *56* (7), 1113-1126.

[35] L. J. Hornbeck, Spatial Light Modulator and Method, US Patent No. 4,566,935 (January 28, 1986).

[36] Kupfer, A.; Louvard, D.; Singer, S. J., Polarization of the Golgi-apparatus and the Microtubule-organizing Center in Cultured Fibroblasts at the Edge of an Experimental Wound. *Proceedings of the National Academy of Sciences of the United States of America-Biological Sciences* **1982,** *79* (8), 2603-2607.

CHAPTER VI

CONCLUSIONS AND FUTURE DIRECTIONS

6.1 Summary and Conclusions

The key advantages of ion mobility-mass spectrometry (IM-MS), speed of mobility separation, sensitivity to small differences in gas phase densities, and compatibility with matrix assisted laser desorption ionization (MALDI) and modified electrospray ionization (ESI) sources, may soon make this technology a valuable tool for lipidomic research. Both the wealth of basic peptide and protein IM-MS research, and its technological advances over the last two decades, resulted in the recent commercialization of this instrumental platform for bioanalytical applications. The commercial success of IM-MS attests to the practicality of its dimensionality enhancement and high throughput capabilities.

In the presented work, IM-MS offers new insights into lipid structural separations, and, potentially, combined structural and spatial analysis of lipids directly from complex biological samples. At the time I joined the McLean group, only two other groups were actively involved in structural and imaging studies of lipids by IM-MS. Woods and coworkers focused solely on mobility separation trends of various classes of lipids without measuring collision cross-sections (CCSs) and performing computational analysis, while Kanik and coworkers studied mobility separation trends of one class of lipids, phosphatidylcholines,

with various degrees of unsaturation and ultimately used CCS values measured in the McLean lab for molecular dynamics simulations. To my knowledge, no other group to date has pursued laser focusing and patterning for mass spectrometry imaging using digital micro-mirror array (DMA) technology.

After joining the McLean group, I first contributed IM-MS data from various phospholipid and sphingolipid standards to an overall study of biomolecular mobility separations trends. In that study my colleagues and I examined the IM-MS conformational space correlations of lipids, peptides, carbohydrates and oligonucleotides. My lipid collision cross-section measurements and molecular dynamics simulations of the gas phase behavior of various bioanalytes provided the structural detail needed to elucidate the statistical variability of the IM-MS correlations of the different biomolecules.

Further computational analysis of the lipid IM-MS data uncovered an important result; in depth molecular dynamics of empirically studied phospholipids and sphingolipids pointed out the key structural differences of the glycerophospholipid and sphingolipid backbone that contribute to the previously unnoticed mobility separation of these two important classes of membrane lipids. In the gas phase sphingolipids are less compact, have lower folding density than glycerophospholipids. Based on computational modeling, the reason for the lower packing ability of sphingolipids appears to be the relative rigidity of the sphingolipid backbone.

Fundamental IM-MS lipid analysis in the context of other biomolecules and in the context of multiple lipid classes naturally led to application of the collected

122

knowledge into the study of lipids directly from complex biological samples. First, we focused on the ability of IM-MS to remove chemical noise (*i.e.*, MALDI matrix clusters) from the lipid mobility m/z correlation line. The ability to distinguish relatively small percent changes in abundance of lipid signals with high statistical significance from small (*i.e.*, 1 mm^2 on plate) *Drosophila* brain tissues, may open the door to high throughput studies of abundance changes of lipids in plant and animal tissues and cell monolayers exposed to external stimuli or challenged by mutations, using the inherently high throughput MALDI platform.

In parallel with IM-MS experiments, I built and characterized a novel optical system for high resolution mass spectrometry imaging of lipids based on the digital micro-mirror array (DMA) device. In my research, I focused on the laser focusing and patterning capabilities of this system. However, the additional capabilities, correction of perspective distortion, and tissue imaging by rapid laser beam rastering across stationary tissues remains an untapped potential of this technology. This optical train does not require optics positioned inside the vacuum of the imaging instrument, and can therefore be used on any other MALDI ready instrumental platform, including IM-MS.

6.2. Future Directions

Mass spectrometry, coupled to condensed phase separation, has enabled lipid structural characterization at an unprecedented level of detail and has the promise to inform our understanding of how lipid structures interact with other

biomolecules. Modern advances in lipid mass spectrometry, such as gas phase separation by ion mobility, coupling of condensed phase and ion mobility separations, and promising new approaches to MS/MS characterization of lipid structures by tailored chemical and electron transfer dissociation will continue to have high impact in lipid research.

Owing to the capability of IM-MS to separate lipids in the IM dimension of analysis by structure, improved detection of lower abundance lipids and/or lipids with low ionization efficiency directly from complex biological samples may be materializing. State of the art commercial IM-MS instruments now allow signal integration, *i.e.* accumulation of all MS signals during the course of an entire MS experiment. IM-MS also allows separation of endogenous and exogenous chemical noise away from the IM-MS spectrum area of lipid signal and IM readily couples to LC separations. I would like to perform proof of principle comparisons of lipid detection from LC/MS *vs.* LC-IM-MS and MALDI-MS *vs.* MALDI-IM-MS experiments to determine the contribution of IM separation to increased detection of molecular lipids.

In near future, I also see several opportunities in using nanoparticles in lipid MS analysis. I would like to pursue selective suppression of phosphatidylcholines by a modified gold nanoparticle approach. Using established synthesis protocols,[1] and commercially available starting materials, I intend to derivatize gold nanoparticles of various gold core diameters with thiol and phosphate terminated ligands. The final optimized synthesis product envisioned is a soluble ligand coated gold nanoparticle with the phosphate

terminus of the ligand oriented to the outside of the gold-ligand sphere. Based on previously published studies about the gas phase stability of the phosphate quaternary ammonium ion non-covalent interaction,[2,3] I propose to test the following hypothesis: I anticipate that laser desorption of lipids from cell and tissue samples in the presence of phosphate terminated gold-ligand nanoparticles will lead to selective suppression of ionization of high abundance choline containing lipid species by phosphate solvation of the preformed charge on the quaternary ammonium ion. If the hypothesis is correct, ionization and detection of lower abundance lipid species normally not available in LDI-MS experiments, due to their suppression by phosphatidylcholines, may be achieved.

The study of spatial distribution of both high and low abundance lipids at higher and higher spatial resolution, down to sub-cellular dimensions, will also continue to be a choice research focus. Metal nanoparticles, particularly those with dimensions of less than 5nm in diameter, may soon become extremely useful in lipid imaging of individual cells and parts of cells, as they have been shown to provide signal enhancement by, most likely, a surface plasmon resonance mechanism. Close on the horizon, I expect, specific metal nanoparticles and nanoparticle combinations will also prove useful in lipid signal selectivity experiments (*i.e.*, preferential ionization of selected lipids), and selective lipid fragmentation.

Plasma sputtering, a method of metal nanoparticle generation and deposition, commonly used to coat nonconductive samples for scanning electron microscopy (SEM), has previously been described to assist analyte desorption

and ionization in secondary ionization mass spectrometry (MS).[4,5,6] I propose to use plasma sputtering for sample preparation for laser desorption ionization (LDI) lipid profiling and imaging MS experiments. Based on previous studies and preliminary data I foresee quick adoption of the proposed plasma sputter deposition protocols by the wider LDI-MS community for reasons of sample preparation speed, selectivity,[7] imaging spatial resolution, and signal enhancement (*i.e.* sensitivity) due to both bulk[8,9] and quantum confinement effects.[10,11]

First, I intend to test and understand the effect of all adjustable parameters on the plasma sputtering process (*i.e.* electrode voltage, argon pressure, plasma to sample distance), on the size of individual deposited silver and iron nanoparticles, and on their deposition thickness. With this knowledge, I will optimize the use of plasma sputtering for silver and iron deposition for MS profiling and imaging of lipids (*e.g.* silver adducts of cholesterol and cholesterol derivatives) from cell and tissue samples. I will then test the potential to image and profile thick tissues, cell colonies, and cell extracts (afforded by the increased surface conductivity of silver and iron covered samples). Last, I will test signal enhancement capabilities due to previously observed quantum dot electronic excitation effects.[10,11]

My time spent with the McLean group and other perceptive collaborators convinced me that there is just as much value in using the proven analytical techniques to solve current challenges in biology, medicine, engineering, as there is in pursuing further and greater analytical capabilities on the horizon. In

fact, I believe, the current climate of science funding seems to encourage visionary projects at the expense of solving much needed problems in basic science for which plentiful analytical capabilities are already available. In this respect I found a much needed balance both within and without the McLean laboratory on the Vanderbilt campus. In my future endeavors I would like to take with me this particular lesson and always balance the yearning to discover and create with the responsibility to apply what we already know well.

REFERENCES

[1] Uzun, O.; Hu, Y.; Verma, A.; Chen, S.; Centrone, A.; Stellacci, F., Water-soluble amphiphilic gold nanoparticles with structured ligand shells. *Chemical Communications* **2008,** (2), 196-198.

[2] Woods, A. S.; Ferre, S., Amazing stability of the arginine-phosphate electrostatic interaction. *Journal of Proteome Research* **2005,** *4* (4), 1397-1402.

[3] Woods, A. S.; Moyer, S. C.; Jackson, S. N., Amazing stability of phosphate-quaternary amine interactions. *Journal of Proteome Research* **2008,** *7* (8), 3423-3427.

[4] Miller, D. J.; Sun, L.; Walzak, M. J.; McIntyre, N. S.; Chvedov, D.; Rosenfeld, A., Static SIMS studies of carboxylic acids on gold and aluminium-magnesium alloy surfaces. *Surface and Interface Analysis* **2003,** *35* (5), 463-476.

[5] Nygren, H.; Eriksson, C.; Malmberg, P.; Sahlin, H.; Carlsson, L.; Lausmaa, J.; Sjovall, P., A cell preparation method allowing subcellular localization of cholesterol and phosphocholine with imaging TOF-SIMS. *Colloids and Surfaces B-Biointerfaces* **2003,** *30* (1-2), 87-92.

[6] Wehbe, N.; Heile, A.; Arlinghaus, H. F.; Bertrand, P.; Delcorte, A., Effects of metal nanoparticles on the secondary ion yields of a model alkane molecule upon atomic and polyatomic projectiles in secondary ion mass spectrometry. *Analytical Chemistry* **2008,** *80* (16), 6235-6244.

[7] Sherrod, S. D.; Diaz, A. J.; Russell, W. K.; Cremer, P. S.; Russell, D. H., Silver nanoparticles as selective ionization probes for analysis of olefins by mass spectrometry. *Analytical Chemistry* **2008,** *80* (17), 6796-6799.

[8] McCombie, G.; Knochenmuss, R., Enhanced MALDI ionization efficiency at the metal-matrix interface: Practical and mechanistic consequences of sample thickness and preparation method. *Journal of the American Society for Mass Spectrometry* **2006,** *17* (5), 737-745.

[9] Knochenmuss, R.; McCombie, G.; Faderl, M., Ion yields of thin MALDI samples: Dependence on matrix and metal substrate and implications for models. *Journal of Physical Chemistry A* **2006,** *110* (47), 12728-12733.

[10] Daniel, M. C.; Astruc, D., Gold nanoparticles: Assembly, supramolecular chemistry, quantum-size-related properties, and applications toward biology, catalysis, and nanotechnology. *Chemical Reviews* **2004,** *104* (1), 293-346.

[11] McLean, J. A.; Stumpo, K. A.; Russell, D. H., Size-selected (2-10 nm) gold nanoparticles for matrix assisted laser desorption ionization of peptides. *Journal of the American Chemical Society* **2005,** *127* (15), 5304-5305.

APPENDIX A

DETAILED TABULAR DATA OF REDUCED MOBILITIES AND COLLISION CROSS-SECTIONS OF LIPIDS

Lipid	Mass-to-Charge Value	CCS			Reduced Mobility (K_o)		
[M+X]$^+$ X=H or Na	m/z	Å^2			cm$^2\cdot$V$^{-1}\cdot$sec^{-1}		
PE 34:2 H$^+$	716.52	206.9	±	2.0	2.627	±	0.068
PE 34:1 H$^+$	718.54	205.8	±	4.3	2.638	±	0.086
PE 34:2 Na$^+$	738.51	213.5	±	2.1	2.532	±	0.032
PE 34:1 Na$^+$	740.52	214.7	±	1.5	2.518	±	0.027
PE 36:4 Na$^+$	762.51	214.4	±	1.6	2.523	±	0.028
PE 36:2 Na$^+$	766.54	220.9	±	2.7	2.446	±	0.038
PE 36:1 Na$^+$	768.55	221.7	±	4.8	2.438	±	0.036
PE 38:5 Na$^+$	788.52	220.6	±	5.2	2.457	±	0.080
PE 38:4 Na$^+$	790.54	228.1	±	3.6	2.396	±	0.084
CB (40:1) Na$^+$	806.65	232.9	±	2.4	2.303	±	0.023
CB (39:1)h Na$^+$	808.63	236.2	±	2.9	2.271	±	0.028
PS 36:2 Na$^+$	810.53	217.1	±	5.5	2.484	±	0.054
PS 36:1 Na$^+$	812.54	222.6	±	2.4	2.407	±	0.026
CB (40:2)h Na$^+$	820.63	236.2	±	5.6	2.271	±	0.055
CB (40:1)h Na$^+$	822.64	234.6	±	5.3	2.286	±	0.052
CB (42:6) Na$^+$	824.60	237.9	±	1.9	2.254	±	0.018
CB (42:2) Na$^+$	832.66	238.8	±	1.7	2.245	±	0.016
PS 38:4 Na$^+$	834.53	225.5	±	2.1	2.376	±	0.022
CB (42:1) Na$^+$	834.68	239.3	±	2.6	2.240	±	0.024
CB (41:1)h Na$^+$	836.66	240.2	±	3.4	2.233	±	0.032
PS 38:1 Na$^+$	840.57	222.6	±	5.5	2.408	±	0.047
CB (42:3)h Na$^+$	846.64	238.8	±	2.2	2.245	±	0.021
CB (42:2)h Na$^+$	848.66	240.3	±	2.7	2.231	±	0.025
CB (44:7) Na$^+$	850.62	242.8	±	1.9	2.208	±	0.017
CB (44:6) Na$^+$	852.63	243.3	±	3.7	2.204	±	0.033

Lipid	Mass-to-Charge Value	CCS			Reduced Mobility (Ko)		
	m/z	Å²			cm²·V⁻¹·sec⁻¹		
PS 40:6 Na⁺	858.53	231.9	±	2.8	2.309	±	0.028
CB (44:2) Na⁺	860.70	245.9	±	5.2	2.181	±	0.046
CB (44:1) Na⁺	862.71	244.3	±	5.5	2.195	±	0.050
CB (44:8)h Na⁺	864.60	245.2	±	2.9	2.205	±	0.020
CB (44:7)h Na⁺	866.61	252.2	±	5.1	2.118	±	0.046
CB (44:2)h Na⁺	876.69	246.7	±	3.7	2.174	±	0.033
PS 42:9 Na⁺	880.51	238.0	±	1.7	2.265	±	0.027
PS 42:8 Na⁺	882.53	230.8	±	3.0	2.386	±	0.120

Lipid	Mass-to-Charge Value	CCS			Reduced Mobility (Ko)		
[M-H]-	m/z	Å²			cm²·V⁻¹·sec⁻¹		
PE 34:2 - H	714.51	207.7	±	1.6	2.587	±	0.020
PE 34:1 - H	716.52	205.6	±	2.6	2.613	±	0.033
PE 36:2 - H	742.54	210.8	±	1.4	2.548	±	0.017
PE 36:1 - H	744.55	211.5	±	4.4	2.540	±	0.053
PS 36:1 - H	788.54	233.3	±	1.5	2.302	±	0.023
PS 40:6 – H	834.53	237.3	±	2.3	2.263	±	0.029

Table A.1 Table of assigned positive and negative mode phosphatidylethanolamine (PE), cerebroside (CB), and phosphatidylserine (PS) signals with their respective measured CCS and reduced mobility (K_o) values. The nomenclature of PE and PS X:Y, indicates that there are X carbons in the fatty acid chains and Y sites of unsaturation. In the nomenclature of CB X:Y, X indicates the number of carbons in the amide linked fatty acid plus eighteen carbons of the sphingosine backbone and Y the total number of double bonds in the entire lipid structure. Parentheses () distinguish sphingolipid from glycerophospholipid nomenclature in the table. In the nomenclature for hydroxylation on cerebrosides (*i.e.*, CB (x:y)h) h denotes presence of hydroxyl group, normally on the number two carbon (from carbonyl) of the amide linked fatty acid.

Table B.1 Negative Mode Dataset p-value Stability Analysis

Statistical analysis was repeated 18 times, each time removing one out of 18 samples (9 control and 9 mutant). This process yielded 18 p-values, one for each sample omission. Table B.1 lists the 18 calculated p-values for each lipid signal change with raw p-value <0.10. The reported standard deviation of the raw p-value is based on the 18 recalculated p-values.

m/z[a]	raw p value	stdev of raw p value	pval1	pval2	pval3	pval4	pval5	pval6	pval7	pval8	pval9	pval10	pval11	pval12	pval13	pval14	pval15	pval16	pval17	pval18
687.6	4.E-09	1.E-08	2.E-08	1.E-08	2.E-08	2.E-09	5.E-09	2.E-08	1.E-08	2.E-08	2.E-08	4.E-08	2.E-08	3.E-09	3.E-08	3.E-08	2.E-08	2.E-08	1.E-08	4.E-09
938.7	7.E-09	3.E-08	2.E-08	2.E-08	3.E-08	5.E-08	2.E-09	4.E-08	3.E-08	6.E-08	8.E-08	1.E-07	3.E-08	3.E-08	5.E-08	5.E-08	1.E-08	4.E-09	2.E-08	7.E-09
936ISO	2.E-08	5.E-08	1.E-08	6.E-08	8.E-08	5.E-08	3.E-09	6.E-08	1.E-07	1.E-07	1.E-07	2.E-07	5.E-08	7.E-08	1.E-07	1.E-07	7.E-08	7.E-08	6.E-08	2.E-08
687ISO	4.E-08	7.E-08	2.E-07	2.E-07	1.E-08	4.E-08	3.E-08	3.E-08	1.E-07	1.E-07	1.E-07	9.E-08	3.E-08	4.E-09	2.E-07	2.E-07	2.E-07	2.E-08	2.E-07	4.E-08
936.7	6.E-08	1.E-07	9.E-08	2.E-07	2.E-07	3.E-07	2.E-10	2.E-07	3.E-07	4.E-07	4.E-07	4.E-07	2.E-07	2.E-07	3.E-07	3.E-07	2.E-07	2.E-07	2.E-07	6.E-08
937.7	2.E-07	4.E-07	5.E-08	6.E-07	6.E-07	5.E-08	5.E-07	2.E-07	7.E-07	8.E-07	1.E-06	2.E-06	3.E-07	5.E-07	7.E-07	7.E-07	5.E-07	4.E-07	4.E-07	2.E-07
689.6	5.E-07	1.E-06	4.E-06	1.E-06	1.E-06	3.E-07	3.E-06	1.E-06	4.E-06	2.E-06	2.E-06	1.E-06	1.E-06	9.E-07	6.E-06	3.E-06	4.E-06	1.E-06	1.E-06	5.E-07
717.6	6.E-06	9.E-06	4.E-06	5.E-06	2.E-05	3.E-06	1.E-05	8.E-06	9.E-06	1.E-05	7.E-06	4.E-05	1.E-05	1.E-06	2.E-05	4.E-06	7.E-06	1.E-05	6.E-06	6.E-06
689ISO	9.E-06	1.E-05	2.E-05	3.E-05	2.E-05	3.E-06	3.E-05	3.E-05	2.E-05	3.E-05	4.E-05	3.E-05	1.E-05	3.E-05	1.E-06	4.E-05	2.E-05	5.E-05	3.E-05	9.E-06
688.6	2.E-05	2.E-05	4.E-05	4.E-05	3.E-05	3.E-05	2.E-05	4.E-05	5.E-05	5.E-05	8.E-05	4.E-05	5.E-05	3.E-05	5.E-05	5.E-05	1.E-05	4.E-05	1.E-05	2.E-05
716ISO	2.E-05	4.E-05	3.E-05	6.E-05	6.E-05	2.E-05	6.E-05	2.E-05	8.E-05	1.E-04	3.E-05	2.E-04	6.E-05	2.E-05	8.E-05	4.E-05	8.E-05	8.E-06	8.E-05	2.E-05
742ISO	3.E-05	3.E-05	6.E-05	7.E-05	5.E-05	8.E-05	6.E-05	8.E-05	8.E-05	4.E-06	2.E-06	6.E-05	8.E-05	7.E-05	1.E-04	1.E-04	5.E-05	5.E-05	7.E-05	3.E-05
910.7	3.E-05	5.E-05	3.E-05	9.E-05	7.E-05	6.E-05	5.E-05	9.E-05	9.E-05	1.E-04	1.E-04	2.E-04	1.E-04	3.E-05	5.E-05	2.E-05	7.E-05	3.E-06	7.E-05	3.E-05
716.6	3.E-05	5.E-05	1.E-05	9.E-05	8.E-05	3.E-05	8.E-05	2.E-05	1.E-04	1.E-04	7.E-05	2.E-04	8.E-05	3.E-05	1.E-04	6.E-05	1.E-04	8.E-06	1.E-04	3.E-05
742.6	3.E-05	4.E-05	8.E-05	9.E-05	6.E-05	9.E-05	8.E-05	1.E-04	9.E-05	2.E-05	5.E-07	1.E-04	1.E-04	8.E-05	1.E-04	2.E-04	7.E-05	6.E-05	8.E-05	3.E-05
739.6	3.E-05	3.E-05	9.E-05	5.E-05	6.E-05	5.E-05	7.E-05	5.E-05	1.E-04	1.E-04	1.E-04	2.E-05	9.E-05	7.E-05	8.E-05	7.E-05	4.E-05	8.E-05	7.E-05	3.E-05
738ISO	4.E-05	3.E-05	1.E-04	7.E-05	7.E-05	5.E-05	7.E-05	1.E-04	1.E-04	1.E-04	1.E-04	4.E-05	1.E-04	7.E-05	8.E-05	1.E-04	5.E-05	1.E-04	6.E-05	4.E-05
661.6	5.E-05	6.E-05	5.E-05	1.E-04	1.E-04	6.E-05	7.E-05	2.E-04	1.E-04	6.E-05	1.E-04	3.E-05	5.E-05	9.E-05	2.E-04	3.E-04	1.E-04	9.E-05	1.E-04	5.E-05
738.6	6.E-05	5.E-05	1.E-04	9.E-05	9.E-05	6.E-05	8.E-05	1.E-04	1.E-04	2.E-04	2.E-04	6.E-05	1.E-04	9.E-05	1.E-04	3.E-04	8.E-05	2.E-04	7.E-05	6.E-05
743.6	8.E-05	1.E-04	1.E-04	1.E-04	2.E-04	3.E-04	2.E-04	2.E-04	2.E-04	9.E-06	3.E-05	4.E-05	2.E-04	2.E-04	3.E-04	4.E-04	9.E-05	1.E-04	2.E-04	8.E-05
917.6	6.E-04	0.001	9.E-04	1.E-03	0.001	9.E-04	3.E-04	9.E-04	4.E-04	0.002	7.E-04	0.004	0.001	0.001	0.002	1.E-04	0.001	9.E-04	0.001	6.E-04
916ISO	7.E-04	0.001	1.E-03	0.001	0.001	6.E-04	3.E-04	8.E-04	8.E-04	0.003	9.E-04	0.005	0.001	1.E-03	0.003	3.E-04	0.001	7.E-04	0.001	7.E-04
916.6	1.E-03	0.001	0.001	0.001	0.001	6.E-04	6.E-04	0.001	0.002	0.004	0.001	0.006	0.002	0.001	0.004	5.E-04	0.002	8.E-04	0.002	1.E-03
835.6	0.002	0.002	0.003	0.002	0.002	0.005	0.004	2.E-04	0.003	0.006	0.010	0.007	0.003	0.003	0.006	0.007	0.003	0.004	0.002	0.002
918.6	0.002	0.003	0.003	0.002	0.003	0.001	0.003	0.002	0.002	0.007	0.003	0.012	0.005	0.003	0.008	0.003	0.003	0.003	0.004	0.002
908.7	0.002	0.002	0.003	0.005	0.004	0.002	0.004	0.005	0.005	0.005	0.008	0.009	0.005	0.001	0.005	0.002	0.006	0.000	0.006	0.002
861.6	0.003	0.002	0.005	0.005	0.005	0.001	0.005	0.006	0.005	0.005	0.001	0.008	0.004	0.004	0.004	0.002	0.004	0.005	0.003	0.003
417.3	0.003	0.002	0.006	0.001	0.004	0.001	0.005	0.003	0.001	0.006	0.007	0.008	0.004	0.004	0.005	0.007	0.002	0.007	0.004	0.003
846.6	0.005	0.003	0.003	0.004	0.005	0.008	0.007	0.008	0.008	0.010	0.011	0.011	0.007	0.004	0.009	0.007	0.004	0.001	0.010	0.005
861ISO	0.005	0.003	0.009	0.010	0.009	0.002	0.010	0.010	0.008	0.007	0.001	0.013	0.006	0.007	0.006	0.005	0.007	0.009	0.007	0.005

Note: (a) for m/z values with the ISO suffix ex. 716ISO p-value analysis was done on combined intensities of the monoisotopic peak 716.6 and isotopic peak 717.6.

Table B.1 (continued). Negative Mode Dataset p-value Stability Analysis

m/z[a]	raw p value	stdev of raw p value	pval1	pval2	pval3	pval4	pval5	pval6	pval7	pval8	pval9	pval10	pval11	pval12	pval13	pval14	pval15	pval16	pval17	pval18
915.6	0.005	0.004	0.005	0.008	0.008	0.008	0.002	0.003	0.007	0.012	0.004	0.018	0.009	0.008	0.014	0.001	0.008	0.006	0.008	0.005
859.6	0.006	0.003	0.010	0.011	0.010	0.000	0.009	0.009	0.010	0.015	0.006	0.008	0.012	0.009	0.008	0.010	0.007	0.010	0.009	0.006
935.7	0.006	0.006	0.008	0.012	0.011	0.007	0.000	0.013	0.012	0.006	0.018	0.020	0.005	0.003	0.015	0.023	0.010	0.007	0.009	0.006
698ISO	0.008	0.007	0.003	0.016	0.012	0.015	0.014	0.011	0.009	0.010	0.019	0.032	0.017	0.012	0.015	0.008	0.011	0.001	0.013	0.008
859ISO	0.009	0.005	0.014	0.016	0.015	0.000	0.014	0.013	0.014	0.022	0.007	0.010	0.018	0.015	0.012	0.016	0.009	0.015	0.013	0.009
698.6	0.009	0.005	0.002	0.018	0.017	0.019	0.016	0.016	0.014	0.011	0.010	0.025	0.018	0.015	0.008	0.011	0.011	0.007	0.016	0.009
686.6	0.010	0.008	0.015	0.011	0.007	0.037	0.003	0.016	0.005	0.019	0.023	0.018	0.020	0.010	0.027	0.012	0.016	0.014	0.015	0.010
317.1	0.014	0.016	0.045	0.011	0.018	0.016	0.015	0.016	0.019	0.015	0.014	0.010	0.018	0.019	0.013	0.021	0.006	0.078	0.026	0.014
730.6	0.015	0.009	0.024	0.023	0.021	0.030	0.025	0.025	0.020	0.001	0.026	0.042	0.024	0.014	0.028	0.007	0.024	0.016	0.019	0.015
730ISO	0.021	0.011	0.034	0.031	0.026	0.041	0.034	0.033	0.027	0.003	0.032	0.053	0.031	0.019	0.036	0.009	0.034	0.020	0.028	0.021
860.6	0.021	0.011	0.033	0.037	0.036	0.000	0.041	0.027	0.034	0.047	0.018	0.020	0.035	0.032	0.022	0.037	0.023	0.044	0.039	0.021
768.6	0.024	0.015	0.036	0.040	0.031	0.001	0.040	0.048	0.015	0.030	0.050	0.061	0.043	0.016	0.029	0.050	0.036	0.022	0.039	0.024
862.6	0.027	0.013	0.042	0.047	0.044	0.024	0.044	0.053	0.042	0.023	0.006	0.059	0.026	0.036	0.016	0.027	0.037	0.043	0.039	0.027
768ISO	0.030	0.018	0.047	0.049	0.036	0.002	0.049	0.057	0.020	0.036	0.052	0.079	0.055	0.017	0.030	0.051	0.045	0.027	0.046	0.030
480.2	0.032	0.017	0.048	0.025	0.025	0.050	0.027	0.063	0.047	0.054	0.046	0.068	0.038	0.050	0.024	0.081	0.018	0.024	0.042	0.032
365.1	0.045	0.059	0.161	0.025	0.066	0.035	0.053	0.040	0.049	0.058	0.057	0.071	0.053	0.026	0.046	0.063	0.024	0.268	0.056	0.045
902.6	0.045	0.039	0.043	0.048	0.049	0.019	0.065	0.034	0.049	0.149	0.047	0.157	0.057	0.044	0.113	0.028	0.051	0.035	0.061	0.045
329.1	0.046	0.038	0.054	0.046	0.048	0.004	0.094	0.038	0.034	0.141	0.110	0.139	0.053	0.020	0.086	0.094	0.053	0.061	0.049	0.046
934ISO	0.051	0.034	0.059	0.089	0.080	0.058	0.004	0.083	0.085	0.023	0.132	0.094	0.048	0.036	0.069	0.143	0.070	0.050	0.069	0.051
326.3	0.051	0.051	0.045	0.052	0.048	0.072	0.068	0.061	0.077	0.089	0.099	0.124	0.050	0.061	0.009	0.250	0.057	0.034	0.053	0.051
701.6	0.057	0.033	0.056	0.062	0.102	0.039	0.089	0.030	0.051	0.080	0.137	0.046	0.055	0.073	0.064	0.156	0.067	0.049	0.082	0.057
755.6	0.065	0.038	0.090	0.105	0.144	0.009	0.090	0.114	0.060	0.069	0.098	0.158	0.073	0.019	0.091	0.121	0.092	0.048	0.094	0.065
769.6	0.074	0.041	0.119	0.112	0.076	0.026	0.110	0.162	0.054	0.085	0.073	0.188	0.133	0.040	0.057	0.072	0.109	0.070	0.102	0.074
659.6	0.084	0.049	0.089	0.086	0.092	0.182	0.067	0.013	0.115	0.110	0.219	0.079	0.052	0.103	0.174	0.138	0.114	0.072	0.124	0.084
367.1	0.086	0.098	0.270	0.050	0.130	0.057	0.098	0.078	0.093	0.107	0.100	0.125	0.098	0.039	0.094	0.114	0.041	0.456	0.098	0.086
914ISO	0.092	0.041	0.093	0.111	0.116	0.120	0.126	0.066	0.110	0.138	0.057	0.210	0.118	0.106	0.163	0.017	0.115	0.092	0.128	0.092
828.6	0.093	0.062	0.105	0.046	0.053	0.169	0.132	0.074	0.136	0.157	0.214	0.293	0.091	0.096	0.143	0.079	0.100	0.061	0.089	0.093
481.1	0.094	0.050	0.161	0.066	0.100	0.049	0.127	0.114	0.101	0.149	0.148	0.158	0.120	0.109	0.119	0.245	0.019	0.139	0.070	0.094
713.6	0.095	0.050	0.069	0.135	0.128	0.204	0.115	0.086	0.077	0.066	0.181	0.221	0.083	0.146	0.137	0.026	0.104	0.136	0.091	0.095
479.2	0.096	0.041	0.148	0.111	0.134	0.091	0.081	0.063	0.109	0.148	0.145	0.129	0.117	0.119	0.090	0.208	0.022	0.157	0.095	0.096
741.6	0.096	0.038	0.113	0.148	0.101	0.154	0.114	0.139	0.157	0.055	0.067	0.160	0.147	0.130	0.086	0.039	0.127	0.062	0.145	0.096
833ISO	0.097	0.070	0.095	0.067	0.072	0.205	0.095	0.025	0.100	0.149	0.346	0.148	0.109	0.117	0.150	0.154	0.105	0.151	0.053	0.097
740ISO	0.099	0.039	0.112	0.151	0.112	0.158	0.120	0.143	0.168	0.067	0.043	0.140	0.143	0.139	0.099	0.037	0.134	0.075	0.149	0.099

Note: (a) for m/z values with the ISO suffix ex. 716ISO p-value analysis was done on combined intensities of the monoisotopic peak 716.6 and isotopic peak 717.6. M. Kliman, N. Vijayakrishnan, L. Wang, J.T. Tapp, K. Broadie, J.A. McLean, *Molecular BioSystems* **2010**, 6, 958-966. - Reproduced by permission of The Royal Society of Chemistry (RSC).

Table B.2 PtdEtn Lipid Fragment Assignments in Negative Ionization Mode.

Identity[a]	avg. *m/z*[b] (stdev)	*m/z* of PE signature fragment peaks[c]	*m/z* (sn-2 fatty acid)	*m/z* (sn-1 fatty acid)	*m/z* of neutral loss of sn-2 fatty acid	*m/z* of neutral loss of sn-2 fatty acid as ketene [M-H-RCH=C=O]
PE 36:2	742.60 (0.008)	140.0, 196.0	279.2 (18:2)	283.3 (18:0)	462.3	480.3
PE 34:1	716.58 (0.006)	140.0, 196.1	281.3 (18:1)	255.3 (16:0)	434.3	452.3
PE 36:4	738.56 (0.009)	140.1, 196.1	279.3 (18:2) 277.3 (18:3)	279.3 (18:2) 281.3 (18:1)	458.4	476.3
PE 35:1	730.63 (0.007)	140.1, 196.1	281.3 (18:1) 283.3 (18:0)	269.2 (17:0) 267.2 (17:1)	448.4	466.4
PE 38:3	768.60 (0.011)	140.0, 196.0	279.2 (18:2) 277.2 (18:3)	309.3 (20:1) 311.3 (20:0)	488.3	506.4
PE 36:3	740.58 (0.008)	140.1, 196.1	277.3 (18:3)	283.3 (18:0)	462.4	480.4

Notes: (a) Lipid identities determined by fragmentation and closest mass matches. Contribution from lipids with plasmalogen (p) and ether fatty acid linkages (o) cannot be determined at the mass resolution of the instrument; PE=PtdEtn, ex. PE X:Y, where X is the total number of carbons and Y is the total number of double bonds in the fatty acyl chains.

(b) Average and standard deviation of detected *m/z* from 18 measurements (9 control, 9 mutant).

(c) Negative mode PtdEtn signature fragment peaks as described in F. F. Hsu and J. Turk, Charge-Remote and Charge-Driven Fragmentation Processes in Diacyl Glycerophosphoethanolamine upon Low-Energy Collisional Activation: A Mechanistic Proposal, Journal of the American Society for Mass Spectrometry, **2000**, *11*, 892-899. M. Kliman, N. Vijayakrishnan, L. Wang, J.T. Tapp, K. Broadie, J.A. McLean, *Molecular BioSystems* **2010**, 6, 958-966. - Reproduced by permission of The Royal Society of Chemistry (RSC).

Table B.3 PtdIns Lipid Fragment Assignments in Negative Ionization Mode.

Identity[a]	avg. *m/z*[b] (stdev)	*m/z* of PI signature fragment peaks[c]	*m/z* (sn-2 fatty acid)	*m/z* (sn-1 fatty acid)	*m/z* of loss of inositol (180) from neutral loss of sn-2/sn-1 fatty acid	*m/z* of loss of inositol –H₂O (162) from neutral loss of sn-2/sn-1 fatty acid	*m/z* of neutral loss of sn-2/ sn-1 fatty acid	*m/z* of neutral loss of sn-2 fatty acid as ketene [M-H-RCH=C=O]
PI 34:1	835.59 (0.010)	223.0, 241.0	281.3 (18:1)	255.3 (16:0)	373.2/ --	--/417.3	553.3/579.3	--
PI 36:2	861.62 (0.010)	223.0, 241.0	279.3 (18:2)	283.3 (18:0)	-- / --	419.3/ --	581.3/ --	599.4
PI 36:3	859.59 (0.007)	223.0, 241.0	277.23 (18:3)	283.3 (18:0)	-- / --	419.3/ --	581.3/ --	599.3
PI 34:2	833.58 (0.008)	223.0, 241.0	279.2 (18:2)	255.2 (16:0)	-- / --	391.2/415.2	553.3/577.3	--

Notes: (a) Lipid identities determined by fragmentation and closest mass matches. Contribution from lipids with plasmalogen (p) and ether fatty acid linkages (o) cannot be determined at the mass resolution of the instrument; PI=PtdIns, ex. PI X:Y, where X is the total number of carbons and Y is the total number of double bonds in the fatty acyl chains.

(b) Average and standard deviation of detected *m/z* from 18 measurements (9 control, 9 mutant).

(c) Negative mode PtdEtn signature fragment peaks as described in F. F. Hsu and J. Turk, Characterization of Phosphatidylinositol, Phosphatidylinositol-4-phosphate, and Phosphatidylinositol-4,5-bisphosphate by Electrospray Ionization Tandem Mass Spectrometry: A Mechanistic Study, *Journal of the American Society for Mass Spectrometry*, **2000**, *11*, 986-999. M. Kliman, N. Vijayakrishnan, L. Wang, J.T. Tapp, K. Broadie, J.A. McLean, *Molecular BioSystems* **2010**, 6, 958-966. - Reproduced by permission of The Royal Society of Chemistry (RSC).

Table B.4 PtdEtn, PtdCho Lipid Fragment Assignments in Positive Ionization Mode.

Identity[a]	avg. m/z[b] (stdev)	M.W. (exact) (detected as [M+H]+ ion)[c]	M.W. (exact) (detected as [M+Na]+ ion)[c]	M.W. (exact) (detected as [M+K]+ ion)[c]	m/z of [PE + Na]+ signature fragment peaks[d]	m/z of [PC+H]+ signature fragment peak[e]	m/z of [PC+Na]+ signature fragment peak[e]	m/z of [PC+K]+ signature fragment peak[e]
				Fragment assignments of significantly changing positive mode signals with highest PtdEtn (PE) contribution				
PE 36:3			741.53		121.0, 146.0, 164.0			
PC 35:6	764.54	763.51				184.1		
PC 32:4	(0.005)			725.50 (<20%)				163.0
PC 33:3		741.53 (<10%)					147.0	
PE 36:2			743.55		121.0, 146.0, 164.0			
PC 35:5	766.56	765.53				184.1		
PC 32:3	(0.006)			727.51 (<20%)				163.0
PC 33:2		743.55 (<10%)					147.0	
PE 35:3	750.56		727.52		121.0, 146.0, 164.0			
PC 32:3	(0.006)		727.52				147.0	
PE 35:2	752.57		729.53		121.0, 146.0, 164.0			
PC 32:2	(0.007)		729.53				147.0	
PE 34:3	736.52		713.50		121.0, 146.0, 164.0			
PC 30:4	(0.009)			697.47 (<20%)				163.0
PE 36:1			745.56		121.0, 146.0, 164.0			
PC 33:1	768.57		745.56				147.0	
PC 35:4	(0.008)	767.55				184.1		
PC 32:2				729.57 (<10%)				163.0

Notes: (a) Lipid identities determined by fragmentation and closest mass matches. Contribution from lipids with plasmalogen (p) and ether fatty acid linkages (o) cannot be determined at the mass resolution of the instrument; PC=PtdCho, PE=PtdEtn, ex. PE X:Y, where X is the total number of carbons and Y is the total number of double bonds in the fatty acyl chains.
(b) Average and standard deviation of detected m/z from 18 measurements (9 control, 9 mutant).
(c) Exact monoisotopic molecular weight of the identified lipid detected as [M+H]+ or metal (Na, K) coordinated ion.
(d) Positive mode PtdEtn signature fragment peaks as described in C. Simoes, V. Simoes, A. Reis, P. Domingues and M. R. Domingues, Determination of the fatty acyl profiles of phosphatidylethanolamines by tandem mass spectrometry of sodium adducts, *Rapid Communications in Mass Spectrometry*, **2008**, *22*, 3238-3244 and G. Stubiger, E. Pittenauer and G. Allmaier, MALDI Seamless Postsource Decay Fragment Ion Analysis of Sodiated and Lithiated Phospholipids, *Analytical Chemistry*, **2008**, *80*, 1664-1678.
(e) Positive mode PtdCho signature fragment peaks as described in R. C. Murphy, J. A. Hankin and R. M. Barkley, *Journal of Lipid Research*, **2009**, *50*, S317-S322. M. Kliman, N. Vijayakrishnan, L. Wang, J.T. Tapp, K. Broadie, J.A. McLean, *Molecular BioSystems* **2010**, 6, 958-966. - Reproduced by permission of The Royal Society of Chemistry (RSC).

Table B.5 PtdCho, PtdEtn Lipid Fragment Assignments in Positive Ionization Mode.

Identity[a]	avg. m/z[b] (stdev)	Raw p value	M.W. (exact)[c] (detected as [M-H+2Na]+ion)	M.W. (exact)[c] (detected as [M+H]+ ion)	M.W. (exact)[c] (detected as [M+Na]+ ion)	M.W. (exact)[c] (detected as [M+K]+ ion)	m/z of [PC+H]+ signature fragment peak[d]	m/z of [PC+Na]+ signature fragment peak[d]	m/z of [PC+K]+ signature fragment peak[d]	m/z of [PE+Na]+ signature fragment peak[e]	m/z of [PE-H+2Na]+ signature fragment peak[f]
					Fragment assignments of significantly changing positive mode signals with highest PtdCho (PC) contribution						
PC 35:2	794.60	8.E-14			771.58				147.0		
PC 34:3	(0.022)					755.55				163.0	
PC 32:1					731.55					163.0	
PC 35:3	770.59	1.E-08		769.56				184.1			
PC 33:0	(0.024)				747.58				147.0		
PE 35:4			725.50								168.0, 186.0
PC 35:3	792.59	1.E-08			769.56				147.0		
PC 34:4	(0.024)					753.54				163.0	
PC 35:2	772.60	8.E-06		771.58				184.1			
PC 32:0	(0.041)					733.57				163.0	
PE 35:3			727.52								168.0, 186.0
PC 32:0	734.59 (0.006)	8.E-05		733.57				184.1			
PC 36:5	802.55	2.E-05			779.55				147.0		
PC 37:1	(0.008)			801.62				184.1			
PC 30:0	728.57	3.E-05			705.53				147.0		
PC 32:3	(0.006)			727.51				184.1			
PC 31:0					719.55				147.0		
PC 33:3	742.56	2.E-04		741.53				184.1			
PE 34:0	(0.005)				719.55(<20%)					121.0, 164.0	
PC 30:1						703.51(<20%)				163.0	
PC 32:4	748.59	2.E-04			725.50				147.0		
PC 33:0	(0.046)			747.58				184.1			
PE 35:4					725.50 (<10%)					121.0, 164.0	
PC 33:2	744.58	3.E-04		743.55					147.0		
PC 32:6	(0.006)				721.47			184.1			
PC 36:2	786.61 (0.009)	1.E-03		785.59				184.1			
PC 32:1	732.58	1.E-03		731.55				184.1			
PE 32:2	(0.005)		687.48								168.0, 186.0
PC 34:3	756.57	3.E-03		755.55				184.1			
PC 32:0	(0.003)				733.56				147.0		
PC 36:0	790.56	3.E-03		789.62				184.1			
PE 36:1	(0.009)		745.56								168.0, 186.0
PC 36:1	788.60 (0.032)	3.E-03		787.61				184.1			
PC 34:1	760.59 (0.007)	4.E-03		759.58				184.1			
PC 36:2	808.60	6.E-03			785.59				147.0		
PC 38:5	(0.005)			807.58				184.1			

Lipid	m/z (SD)	value					
PC 34:2	758.58 (0.004)	6.E-03	757.56		184.1		
PC 32:1	754.56 (0.006)	7.E-03		731.55		147.0	
PC 34:3			753.53		184.1		
PE 35:1				731.55 (<20%)			121.0, 164.0
PC 31:3	714.53 (0.008)	1.E-02	713.50		184.1		
PE 32:0				691.52			121.1, 164.0
PC 34:2	796.57 (0.018)	1.E-02		757.56		163.0	
PC 37:4			795.58		184.1		
PC 35:1				773.59 (<20%)		147.0	
PC 36:4	804.57 (0.006)	2.E-02		781.56		147.0	
PC 30:5	718.56 (0.005)	2.E-02		695.45		147.0	
PC 31:1			717.53 (<20%)		184.1		
PC 32:2	730.58 (0.006)	0.028	729.53		184.1		

Notes: (a) Lipid identities determined by fragmentation and closest mass matches. Contribution from lipids with plasmalogen (p) and ether fatty acid linkages (o) cannot be determined at the mass resolution of the instrument; PC=PtdCho, PE=PtdEtn, ex. PE X:Y, where X is the total number of carbons and Y is the total number of double bonds in the fatty acyl chains.

(b) Average and standard deviation of detected *m/z* from 18 measurements (9 control, 9 mutant).

(c) Exact monoisotopic molecular weight of the identified lipid detected as [M+H]+ or metal (Na, K) coordinated ion.

(d) Positive mode PtdCho signature fragment peaks as described in R. C. Murphy, J. A. Hankin and R. M. Barkley, *Journal of Lipid Research*, **2009**, *50*,S317-S322.

(e) Positive mode PtdEtn signature fragment peaks as described in C. Simoes, V. Simoes, A. Reis, P. Domingues and M. R. Domingues,
Determination of the fatty acyl profiles of phosphatidylethanolamines by tandem mass spectrometry of sodium adducts, *Rapid Communications
In Mass Spectrometry*, **2008**, *22*, 3238-3244.

(f) Positive mode PtdEtn signature fragment peaks as described in G. Stubiger, E. Pittenauer and G. Allmaier, MALDI Seamless Postsource Decay Fragment Ion Analysis of Sodiated and Lithiated Phospholipids, *Analytical Chemistry*, **2008**, *80*, 1664-1678. M. Kliman, N. Vijayakrishnan, L. Wang, J.T. Tapp, K. Broadie, J.A. McLean, *Molecular BioSystems* **2010**, 6, 958-966. - Reproduced by permission of The Royal Society of Chemistry (RSC).

**REFERENCES OF ADAPTATION
FOR CHAPTERS**

Chapter I: Sections adapted from:

(a) Michal Kliman, Jody C. May, and John A. McLean, "Lipid Analysis and Lipidomics by Structurally Selective Ion Mobility-Mass Spectrometry", submitted to *Biochimica et Biophysica Acta – Molecular and Cell Biology of Lipids*.

(b) Michal Kliman, Jody C. May, Jarrod Smith, Amina S. Woods, J. Albert Schultz, Terry P. Lybrand, John A. McLean, "Structural Selectivity of Anhydrous Sphingolipids and Glycerophospholipids in Ion Mobility-Mass Spectrometry Analysis", submitted to coauthors, formatted for *Journal of American Chemical Society*.

(c) Jeffrey R. Enders, Michal Kliman, Sevugarajan Sundarapandian, John A. McLean, "Peptide and Protein Analysis using Ion Mobility-Mass Spectrometry", submitted to **Protein and Peptide Mass Spectrometry in Drug Discovery,** Wiley-Blackwell John Wiley & Sons, Inc., Michael L. Gross, ed.

(d) Figure 1.1 adapted from Figure 2 in John A. McLean, Whitney B. Ridenour and Richard Caprioli "Profiling and imaging of tissues by imaging ion mobility-mass spectrometry", *Journal of Mass Spectrometry* **2007**, **,** *42* (8), 1099-1105.

Chapter II: Adapted with kind permission from Springer Science+Business Media: Larissa S. Fenn, Michal Kliman, Ablatt Mahsut, Sophie R. Zhao, and John A. McLean, "Characterizing Ion Mobility-Mass Spectrometry Conformation Space for the Analysis of Complex Biological Samples", *Analytical and Bioanalytical Chemistry* **2009**, *394* (1), 235-244.

Chapter III: Adapted from Michal Kliman, Jody C. May, Jarrod Smith, Amina S. Woods, J. Albert Schultz, Terry P. Lybrand, John A. McLean, "Structural Selectivity of Anhydrous Sphingolipids and Glycerophospholipids in Ion Mobility-Mass Spectrometry Analysis", submitted to coauthors, formatted for *Journal of the American Chemical Society*

Chapter IV: Adapted from Michal Kliman, Niranjana Vijayakrishnan, Lily Wang, John T. Tapp, Kendal Broadie, and John A. McLean, "Structural Mass Spectrometry Analysis of Lipid Changes in a Drosophila Epilepsy Model Brain",

Chapter V: Adapted from Michal Kliman, Jay G. Forsythe, John A. McLean, "Dynamic Light Patterning for High Spatial Resolution Imaging of Lipids, in preparation for the Journal of the American Society for Mass Spectrometry.

Curriculum Vitae

Michal Kliman   H:(615) 292-2012   W:(615) 343-4563
2011 25th Ave South, Nashville, TN   michal.kliman@vanderbilt.edu

RESEARCH   LIPID, BIOANALYTICAL IM-MS (MALDI, ESI), COMPUTATIONAL MODELING (GAUSSIAN, AMBER), LASER OPTICS.

2006 – Present   Vanderbilt University, Nashville TN, Structural Mass Spectrometry Laboratory of Dr. John McLean, Graduation July 2011

Advanced Structural and Spatial Analysis of Lipids Using Ion Mobility-Mass Spectrometry

Ion mobility-mass spectrometry (IM-MS) provides rapid (µs-ms) two dimensional separations on the basis of molecular structure and mass-to-charge (m/z), respectively. Based on differences in intramolecular packing of various biomolecules, the added separation dimension allows resolution of isobaric (*i.e.*, same m/z) or nearly isobaric lipids from peptides, carbohydrates, and oligonucleotides. Experimentally determined IM collision cross sections (*i.e.*, apparent surface areas in Å^2) of major membrane lipid classes are interpreted by performing molecular dynamics simulations. Glycerophospholipid and sphingolipid signals are resolved by IM based on structural differences of the glycerol and sphingosine backbones. In addition to resolving lipids from other biomolecules and classes of lipids, IM-MS is shown to be a useful method for mobility separation of exogenous chemical noise in support of relative quantitation of lipid changes in *Drosophila eas* mutant. These advantages of IM-MS may soon become useful in spatially resolved imaging of lipid species in tissues and cells. Digital light patterning for laser focusing and patterning in high spatial resolution studies of lipids in tissues and cells, compatible with the IM-MS platform is described.

EDUCATION   BIOANALYTICAL CHEMISTRY

2006 – Present   Vanderbilt University, Nashville, TN
PhD program, Department of Chemistry, Graduation July 2011, **GPA: 3.9**
Honors: Vanderbilt Dissertation 2009 Enhancement Grant Recipient
ACS Student Members Excellence in Teaching Award 2009/10
VICB Student Award 2010 Finalist
FACSS Student Poster Award 2010

1997 – 1999   Union University, Jackson, TN, **GPA: 4.0**
BSc. in Chemistry; Finance minor
Honors: Recipient of the Union University Academic Medal

1993 – 1997   University of Economics and Slovak Technical University, Bratislava, Slovak Republic, **GPA: 3.6**
Double Major: Applied Statistics and Chemistry

TEACHING

8/2010 – 12/2010   Undergraduate Research Mentor, McLean Laboratory

1/2010 – 5/2010   Teaching Assistant, Analytical Chemistry Laboratory

8/2006 – 12/2006   Teaching Assistant, General Chemistry Laboratory

July 15, 2011

WORK EXPERIENCE   LIQUID, GAS CHROMATOGRAPHY (LC, GC), IM-MS

2006 – Present   Vanderbilt University, Nashville, TN; Graduate Research Assistant, Structural Mass Spectrometry Laboratory of Dr. John McLean (**MALDI/ESI**-**IM-MS**)

2005 – 2006   TEC Environmental Laboratories, Jackson, TN; Analytical Mass Spectrometrist (**GC/MS**)
                        Set up non-volatiles analysis gas chromatography MS out of box, also performed volatiles analysis of soil and water samples.

2001 – 2005   Siegel-Robert Automotive, Inc., Ripley, TN; Chief Chemist **(LC)**
                        Supervised four full time employees in a 24 hour analytical lab. Voluntary leave to pursue graduate and medical school applications.

1999 – 2001   Siegel-Robert Automotive, Inc., Ripley, TN; Analytical Chemist (**LC**)
                        Performed wet chemistry, spectrometry, liquid chromatography, and scanning electron microscopy analyses.

PUBLICATIONS

Kliman, M., May, J.C., McLean, J.A., 2011. Lipid Analysis and Lipidomics by Structurally Selective Ion Mobility-Mass Spectrometry, Invited contribution for inclusion in *Biochimica et Biophysica Acta – Molecular and Cell Biology of Lipids* Special Issue: Lipidomics and Imaging Mass Spectrometry, Robert C. Murphy & Alfred H. Merrill, Jr., guest eds., in press.

Enders, J.R., **Kliman, M.**, Sundarapandian, S., McLean, J.A., 2010. Peptide and Protein Analysis using Ion Mobility-Mass Spectrometry, Wiley Books: Mass Spectrometry of Proteins and Peptides in Drug Discovery, Gross, M.L., Pramanik, B., Chen, G., eds., in press.

Kliman, M., Vijayakrishnan, N., Wang, L., Tapp, J.T., Broadie, K., McLean, J.A., 2010. Structural Mass Spectrometry Analysis of Lipid Changes in a Drosophila Epilepsy Model Brain, *Molecular BioSystems*, 6(6), pp. 958-966.

Ridenour, W.B., **Kliman, M.**, McLean, J.A., Caprioli, R.M., 2010. Structural Characterization of Phospholipids and Peptides Directly from Tissue Sections by MALDI Traveling-Wave Ion Mobility-Mass Spectrometry, *Analytical Chemistry* 82(5), pp. 1881-1889.

Fenn, L.S., **Kliman, M.**, Mahsut, A., Zhao, S.R., McLean, J.A., 2009. Characterizing Ion Mobility-Mass Spectrometry Conformation Space for the Analysis of Complex Biological Samples, *Analytical and Bioanalytical Chemistry*, 394(1), pp. 235-244.

Gies, A.P., **Kliman, M.**, McLean, J.A., Hercules, D.M., 2008. Characterization of Branching in Aramid Polymers Studied by MALDI-Ion Mobility/Mass Spectrometry. *Macromolecules*, 41(22), pp. 8299-8301.

PUBLICATIONS IN PREPARATION

Kliman, M., Woods, A.S., Schultz, J.A., Lybrand, T.P., Smith, J., McLean, J.A., 2011. Structural Selectivity of Anhydrous Sphingolipids and Glycerophospholipids.

Forsythe, J.G., **Kliman, M.**, Lawrie, J.L., Broussard, J.A., Jiao, Y., Webb, D.J., Weiss, S.M., McLean, J.A., 2011. Semi-transparent Porous Silicon Films for Confocal and Mass Spectrometry Imaging of Cell Monolayers.

July 15, 2011

PUBLICATIONS IN PREPARATION (CONTINUED)

Kliman, M., Korade, Z., Xu, L., McLean, J.A., Porter, N.A., 2011. Relative Quantitation and High Resolution Mass Spectrometry Imaging of Cholesterol and 7-Dehydrocholesterol Oxysterols in Smith-Lemli-Opitz Syndrome Mouse Model.

Kliman, M., Forsythe, J.G., McLean, J.A., 2011. Dynamic Light Patterning for High Spatial Resolution Imaging of Lipids.

SELECTED RESEARCH PRESENTATIONS AND POSTERS

Kliman, M., Korade, M., Xu, L., McLean, J.A., Porter, N.A., 2010. Relative Quantitation and High Resolution Mass Spectrometry Imaging of Cholesterol and 7-Dehydrocholesterol Oxysterols in Smith-Lemli-Opitz Syndrome Mouse Model. In: *Vanderbilt Kenedy Center Science Day*, February 25, 2011, Nashville, TN, USA.

Kliman, M., Forsythe, J.G., McLean, J.A., 2010. Ion Mobility Mass Spectrometry Structural Characterization and High Resolution Imaging and Profiling of Lipids. In: *Research Center Julich, Laboratory of Dr. Sabine Becker*, November 15-19, 2010, Julich, Germany.

Kliman, M., Forsythe, J.G, McLean, J.A., 2010. Advances in Structural Characterization and High Resolution Profiling and Imaging of Lipid Species with Ion Mobility Mass Spectrometry. In: *The Federation of Analytical Chemistry and Spectroscopy Societies (FACSS) Conference*, October 24-29, 2010, Raleigh, NC, USA.

Kliman, M., Enders, J.R., Goodwin, C.R., McLean, J.A., 2009. Dynamic Laser Patterning for Biomolecular Imaging MALDI – Mass Spectrometry. In: *The Federation of Analytical Chemistry and Spectroscopy Societies (FACSS) Conference*, October 18-22, 2009, Louisville, KY, USA.

Kliman, M., Korade, M., Xu, L., McLean, J.A., Porter, N.A., 2009. Dynamic Laser Patterning for Biomolecular Imaging MALDI – Mass Spectrometry. In: *Vanderbilt Institute of Chemical Biology Summer Retreat*, August 8, 2009, Nashville, TN, USA.

Kliman, M., Woods, A.S., Schultz, J.A., McLean, J.A., 2009. Fine Structure in Lipid Conformation Space: Study of Ion Mobility Mass Spectrometry Resolution of Sphingolipids and Glycerolipids. In: *American Society for Mass Spectrometry (ASMS) 21st Sanibel Conference on Mass Spectrometry*, January 23-26, 2009, St. Pete Beach, FL, USA.

Ridenour, W.B., **Kliman, M.**, McLean, J.A., Caprioli, R.M., 2009. Measurements of Lipid Collision Cross Sections Directly from Tissue Using Imaging MALDI Ion Mobility-MS. In: *American Society for Mass Spectrometry (ASMS) 21st Sanibel Conference on Mass Spectrometry*, January 23-26, 2009, St. Pete Beach, FL, USA.

Kliman, M., Woods, A.S., Schultz, J.A., McLean, J.A., 2008. Structural Resolution of Sphingolipids and Glycerophospholipids by Ion Mobility Mass Spectrometry. In: *The Southeastern Regional Meeting of the American Chemical Society*, November 12-15, 2008, Nashville, TN, USA.

Fenn, L.S., **Kliman, M.**, Mahsut, A., Zhao, S.R., Kerr, T.J., Gant, R.L., McLean, J.A., 2008. Integrated 'Omics' Using Structural Mass Spectrometry Strategies. In: *The Southeastern Regional Meeting of the American Chemical Society*, November 12-15, 2008, Nashville, TN, USA.

Ugarov, M.V, Egan, T.F., Schultz, J.A., Fenn, L.S., **Kliman, M.**, McLean, J.A., Jackson, S.N., Wang, H.J., Woods, A.S., 2007. Study of Lipids in Tissues by Ion Mobility Time-Of-Flight Mass Spectrometry. In: *American Society for Mass Spectrometry (ASMS) Conference*, June 3-7, 2007, Indianapolis, IN, USA.